UNIVERSIDADE D COIMBRA

FACULDADE DE CIÊNCIAS E TECNOLOGIA

Ductile fracture prediction using a coupled damage model

Submitted in Partial Fulfilment of the Requirements for the Degree of Master in Mechanical Engineering in the speciality of Production and Project

Previsão da fratura dúctil com recurso a um modelo de dano acoplado

Author

João Paulo Martins Brito

Advisor

Prof. **Marta Cristina Cardoso Oliveira**

Jury

President	**Professor Doutor Pedro André Dias Prates** Professor Auxiliar Convidado da Universidade de Coimbra
Vowel	**Professor Doutor José Luís de Carvalho Martins Alves** Professor Associado da Universidade do Minho
Advisor	**Professor Doutor Marta Cristina Cardoso Oliveira** Professora Auxiliar da Universidade de Coimbra

Coimbra, July, 2018

To my family.

"*They succeed, because they think they can.*"

Virgil, in *Aeneid* (29–19 BC), Book V.

Acknowledgements

Above all, I would like to express my deepest gratitude to my scientific advisor who provided crucial guidance and support throughout this study. I thank Professor Marta Oliveira for her continuous guidance, encouragement and endless patience. Her comments, discussions and suggestions were essential to the accomplishment of this thesis.

I would also like to acknowledge Professor Diogo Neto, for his insightful comments and fruitful conversations. His drive for scientific rigor and excellence has been a great source of inspiration for me.

Special recognition is extended to Professor José Luís Alves, who afforded numerous constructive comments and academic insights on the ductile damage modelling framework, as well as for his computational expertise, which were invaluable to the completion of this research.

I also wish to thank all members of the research centre in which this thesis was conducted – CEMMPRE (Centre for Mechanical Engineering, Materials and Processes), for the pleasant and inspiring atmosphere, good-mood and friendship.

Finally, I would like to thank my family and Beatriz, for their unconditional support and encouragement throughout both this work and earlier academic accomplishments, during the course of my M.Sc. degree at the Department of Mechanical Engineering of the University of Coimbra.

This work was carried out under the project “Watch4ming: Monitoring the stamping of advanced high strength steels” with reference P2020-PTDC/EMS-TEC/6400/2014 (POCI-01-0145-FEDER-016876), co-funded by the Foundation for Science and Technology and the EU/FEDER, through the program COMPETE 2020.

Abstract

The growing complexity of the sheet metal formed products and the shortening of the development cycles has placed new challenges to this forming industry. In this context, it is well-known that the numerical simulation of the forming processes assumed a vital role to face up these challenges. In particular, the introduction of new materials with higher strength-to-weight ratio, and consequently reduced ductility, have sparked a growing interest on the development of reliable computational tools, able to accurately predict the onset of failure of ductile materials.

The main objective of this work is to evaluate the ability of a coupled micromechanical damage model – the so-called CPB06 porous model, to describe the damage accumulation and, ultimately, the onset of failure of ductile materials exhibiting tension-compression asymmetry (SD effects). The main features of the CPB06 porous model are investigated and the importance of the yield loci shape, through the role played by all stress invariants, on the damage evolution are highlighted.

Within this framework, a detail sensitivity analysis of the damage model is firstly performed based on the yield loci change of shape and size, when varying material and/or damage parameters. Both two-dimensional and three-dimensional representations of the yield surfaces are analysed. The influence of the stress state through the stress triaxiality, hydrostatic stress and the sign of the third invariant of the deviatoric stress tensor, particularly for axisymmetric loadings, is also studied. Next, a numerical analysis is carried out, based on single-element computations under axisymmetric and hydrostatic stress states, obeying the isotropic form of the CPB06 porous model. The applicability and reliability of the damage model is assessed by comparing the obtained results with the ones predicted by documented and well-accepted micromechanical finite element computations on three-dimensional unit cells. Additionally, the numerical tests are complemented with a brief sensitivity analysis regarding the matrix isotropic hardening law parameters. All numerical simulations are performed with the in-house finite element solver DD3IMP.

It is shown that, under tensile axisymmetric loadings, the damage model predicts two very distinct behaviours for the ductile damage evolution, whit regard to the sign of the third

deviatoric stress invariant. For positive values of this invariant, the model is sensitive to the SD effects, in agreement with the behaviour predicted by the unit cell studies. Nonetheless, for negative values of this invariant the damage model is shown to be insensitive to the SD effects, which contrasts with the behaviour predicted by the same studies. It is concluded that the insensitivity to the SD effects for this particular stress state is due the homogeneous characteristics of the yield function, implying that the direction of the plastic strain increment, and eventually the damage accumulation, are independent of the tension-compression asymmetry displayed by the materials.

Keywords: Ductile Damage, Porous Materials, Micromechanical Damage Model, CPB06, SD Effects, Stress Invariants.

Resumo

A crescente complexidade dos componentes obtidos pelo processo de estampagem de chapas metálicas e a redução dos ciclos de desenvolvimento de novos produtos colocaram novos desafios a esta tecnologia de conformação. Neste contexto, a simulação numérica do processo de estampagem de chapas metálicas assumiu um papel notório para enfrentar estes desafios. Em particular, a introdução de materiais com maior relação resistência-peso e, consequentemente, menor ductilidade, despertou um interesse acrescido no desenvolvimento de ferramentas computacionais fiáveis e robustas, com capacidade para prever com precisão a ocorrência da rotura de materiais dúcteis.

O principal objetivo deste trabalho é avaliar a capacidade de um modelo de dano micromecânico acoplado – o modelo poroso CPB06, para descrever a acumulação de dano e, eventualmente, o instante em que ocorre a falha mecânica de materiais dúcteis que exibem assimetria tração-compressão (efeitos SD). As principais características do modelo poroso CPB06 são investigadas e é destacada a importância da forma da superfície de elasticidade, através do papel desempenhado por todos os invariantes do tensor das tensões, na evolução do dano dúctil.

Neste contexto, inicialmente é realizada uma análise de sensibilidade ao modelo, com base na alteração da forma e dimensão da superfície limite de elasticidade com a variação dos parâmetros materiais e/ou de dano. São analisadas representações tridimensionais e bidimensionais destas superfícies. A influência do estado de tensão caracterizado através da triaxialidade, da pressão hidrostática e do sinal do terceiro invariante do tensor desviador das tensões, particularmente para carregamentos axissimétricos, é igualmente estudada. De seguida, é realizada uma análise com base em simulações numéricas com um único elemento finito submetido a estados de tensão axissimétricos e hidrostáticos, obedecendo à forma isotrópica do modelo poroso CPB06. A aplicabilidade e fiabilidade do modelo de dano são avaliadas comparando os resultados obtidos com os previstos por estudos numéricos em células unitárias tridimensionais documentados na literatura. Os testes numéricos são complementados por uma análise de sensibilidade em relação aos parâmetros da lei de

encruamento isotrópico da matriz. Todas as simulações numéricas são realizadas com o código de elementos finitos académico DD3IMP.

A análise numérica mostra que, em carregamentos axissimétricos de tração, o modelo de dano prevê dois comportamentos bastante distintos para a evolução do dano dúctil, em função do sinal do terceiro invariante do tensor desviador das tensões. Para valores positivos deste invariante, o modelo é sensível aos efeitos SD, o que está de acordo com o comportamento previsto pelos estudos numéricos realizados com células unitárias. No entanto, para valores negativos deste invariante, o modelo de dano mostra-se insensível aos efeitos SD, o que contrasta com o comportamento previsto pelos mesmos estudos. Conclui-se que a insensibilidade aos efeitos SD para este estado de tensão é devida à homogeneidade da função que define a superfície limite de elasticidade do critério. Esta característica matemática da função implica que a direção do incremento de deformação plástica e, em última análise, a acumulação de dano, sejam independentes da assimetria tração-compressão exibida pela matriz dos materiais porosos.

Palavras-chave: Dano Dúctil, Material Poroso, Modelo de Dano Micromecânico, CPB06, Efeitos SD, Invariantes do tensor das tensões.

Contents

List of Figures

List of Tables

List of Symbols and Acronyms

Symbols

α	Homogeneity degree of a homogeneous function
ε_0	Swift's law material parameter
ε_N	Mean value of the strain-controlled Gaussian distribution
$\boldsymbol{\varepsilon}^p$	Local plastic strain tensor
$\bar{\varepsilon}_f^P$	Critical equivalent plastic strain at fracture
$\dot{\bar{\varepsilon}}_M^p$	Local matrix effective plastic strain rate
θ	Angle relating Barlat et al. (2005) characteristic equation constants
θ_Σ	Lode angle
$\overline{\theta}_\Sigma$	Lode angle parameter
$\dot{\lambda}$	Rate of the plastic multiplier
ν	Poisson's coefficient
ξ_Σ	Normalized third invariant of the deviatoric stress tensor
ρ	Ratio of the macroscopic axial and lateral axisymmetric stresses
$\boldsymbol{\sigma}$	Local Cauchy stress tensor
σ_C	Isotropic matrix uniaxial yield stress in compression
σ_M	Flow stress of the matrix
σ_p	Mean value of the stress-controlled Gaussian distribution
σ_T	Isotropic matrix uniaxial yield stress in tension (and current matrix flow stress)
σ_Y	Gurson's yield stress of the undamaged material
σ_0^T	Initial yield strength in tension
σ_1^T	Uniaxial yield strength of the matrix along the 1-direction
$\boldsymbol{\Sigma}$	Macroscopic principal stress tensor

$\boldsymbol{\Sigma}'$	Macroscopic deviatoric stress tensor
$\hat{\boldsymbol{\Sigma}}$	Macroscopic CPB06 linear-transformed stress tensor
Σ_{11}, Σ_{22}	Axisymmetric macroscopic true lateral stress
Σ_{33}	Axisymmetric macroscopic true axial stress
Σ_{e}	Macroscopic von Mises equivalent stress
Σ_{m}	Macroscopic mean stress
$\Sigma_{\gamma\gamma}$	Sum of the macroscopic in-plane stresses
$\tilde{\Sigma}_{e}$	CPB06 macroscopic equivalent stress
$\dot{\Sigma}_{m}$	Macroscopic mean stress rate
$\overline{\Sigma}$	Barlat et al. (2005) modified variable for the linear-transformed stress, $\hat{\Sigma}$
$\overline{\Sigma}_{e}$	Normalized macroscopic von Mises equivalent stress
$\overline{\Sigma}_{m}$	Normalized macroscopic mean stress
φ	Function defining a yield criterion
φ_{G}^{S}, φ_{G}^{C}	Gurson's original yield criterion for spherical and cylindrical voids, respectively
ϕ_1, ϕ_2, ϕ_3	CPB06 anisotropic constants
$\omega, \overline{\omega}$	Complex constant and its conjugate, respectively
a	CPB06 yield criterion constant – degree of homogeneity
A_{N}, B_{N}	Normal distribution proportionally constants
$\mathbf{B}$	Forth-order inverse of the anisotropic linear-transformed tensor $\mathbf{L}$
C_0	Cubic finite element initial side length
C_{eqv}	Gurson's cylindrical void criterion constant
C_i	Current FE side dimensions
$\mathbf{C}$	CPB06 fourth-order tensor describing the anisotropy of the matrix
D	Internal damage variable
D_{c}	Critical internal damage
$\mathbf{D}^{p}$	Macroscopic plastic strain rate tensor

E	Young's modulus
E_1, E_2, E_3	Macroscopic principal logarithmic strains
E_e	Macroscopic von Mises equivalent strain
$\mathbf{e}_1, \mathbf{e}_2, \mathbf{e}_3$	Reference frame associated with axis of orthotropy
f	Void volume fraction
$\dot{f}$	Void volume fraction rate of change
f_0	Initial void volume fraction
f_c	Critical void volume fraction, onset of coalescence
f_F	Void volume fraction at final failure
f_N	Void volume fraction nucleation potential of the strain-controlled Gaussian distribution
f_P	Void volume fraction nucleation potential of the stress-controlled Gaussian distribution
$\dot{f}_{growth}$	Void growth rate
$\dot{f}_{nucleation}$	Void nucleation rate
f^*	Effective void volume fraction
f_U^*	Ultimate value of the effective void volume fraction
$f(\boldsymbol{\sigma}, \boldsymbol{\varepsilon}_p)$	Weighting function of damage
g	Axisymmetric isotropic equivalent stress constant
$\hat{g}$	Axisymmetric anisotropic equivalent stress constant
h	CPB06 porous model anisotropic hydrostatic factor
H_1, H_2, H_3	First, second and third invariants of tensor $\hat{\boldsymbol{\Sigma}}$
H_p, H_q	Constants of Barlat et al. (2005) modified characteristic equation
I_1^{Σ}	First stress invariant
$\mathbf{I}$	Identity second order tensor
$J_2^{\Sigma}, J_3^{\Sigma}$	Second and third macroscopic deviatoric stress invariants
J_2^E	Second invariant of the macroscopic principal strain tensor
k	Material parameter capturing strength-differential effects

K	Swift's law hardening coefficient
$\mathbf{L}$	CPB06 linear-transformed anisotropic tensor
m	Isotropic CPB06 effective stress constant
$\hat{m}$	Anisotropic CPB06 effective stress constant
n	Swift's law hardening exponent
$\hat{n}$	CPB06 anisotropic constant accounting for SD effects
O	Point denoting the coordinate system origin
$\hat{p}_{\mathrm{Y}}^{+}$	Tensile hydrostatic mean stress limit
$\hat{p}_{\mathrm{Y}}^{-}$	Compressive hydrostatic mean stress limit
P	Arbitrary point contained in the axisymmetric yield locus
q_1, q_2, q_3	Tvergaard's fitting parameters
q_δ	Void coalescence accelerating factor
r, θ	Gurson's limit-analysis radial and polar coordinates
$r(\sigma_{\mathrm{T}}, \sigma_{\mathrm{C}})$	Function describing isotropic SD effects
$\mathbf{R}$	π-plane representation orthogonal rotation matrix
s_{N}	Standard deviation of the strain-controlled Gaussian distribution
s_{p}	Standard deviation of the stress-controlled Gaussian distribution
$s(x)$	Generic real valued homogeneous function
t	Homothetic transformation scale factor
t_1, t_2	CPB06 porous model anisotropic scalars
T_Σ	Macroscopic stress triaxiality
$\mathbf{t}$	Prescribed axisymmetric Cauchy stress vector
$\mathbf{T}$	Fourth-order deviatoric unit tensor
$u_i^*(t)$	Time histories of the FE displacements in each direction
$\mathbf{u}$	Displacement between the current and the reference configuration
$z, \overline{z}$	Complex number and its conjugate, respectively
z_{s}	CPB06 porous model isotropic hydrostatic factor

Acronyms

2D	Two-Dimensional
3D	Three-Dimensional
AHSS	Advanced High Strength Steels
BCC	Body Centred Cubic
CDM	Continuum Damage Mechanics
CPB06	Cazacu, Plunkett and Barlat 2006 yield criterion
DCI	Digital Image Correlation
DD3IMP	Deep Drawing 3D IMPlicit finite element solver
DD3MAT	Deep Drawing 3-D MATerial
DP	Dual-Phase
EBT	Equi-Biaxial Tension
FCC	Face Centred Cubic
FE	Finite Element
FEA	Finite Element Analysis
FFT	Fast Fourier Transform
FLD	Forming Limit Diagram
GTN	Gurson–Tvergaard–Needleman model
HCP	Hexagonal Closed Packed
HSS	High Strength Steels
MS	Martensitic Steels
RVE	Representative Volume Element
SD	Strength-Differential
SRI	Selective Reduced Integration
TRIP	Transformation Induced Plasticity steels

1. Introduction

This chapter presents the motivation and a brief background on the framework of ductile fracture prediction using the finite element method, highlighting the growing industrial interest on damage modelling and its current challenges. The key objectives of the thesis and the outline of the text are also presented.

1.1. Motivation

Sheet metal forming is a process in which an initially planar geometry of a sheet metal, the blank, is deformed to a desired shape applying external forces that cause plastic deformation of the material. Being a near net-shape technology, this process is distinguished from other industrial manufacturing processes due to its high production rate, cost effectiveness, flexibility and enhanced mechanical properties of the final product. This technology is widely used in industries such as automotive, aeronautics, naval as well as in domestic and decorative applications.

Driven by the increasing complexity of the sheet metal forming processes and products as well as the global competition and the need for flexibility, due to the demands imposed by the market, the industry has demonstrated for the past decades a special interest in the potential of computational mechanics to solve its challenges (Yang, Ahn, Lee, Park, & Kim, 2002). One of the most popular numerical tools currently used is the Finite Element Analysis (FEA), which requires solving a set of algebraic equations that govern the mechanical behaviour of a material for a discrete number of domains (Pack, 2017).

Indeed, currently, the numerical simulation of sheet metal forming processes using the FEA assumes a vital role in the design stages of new products and tools. The ability to virtually predict, at a preliminary project stage, possible forming defects in a product (e.g. surface and dimensional, unsatisfactory final mechanical properties, rupture/fracture) allows the minimization of the experimental based, and consequent costly and time-consuming, trial-and-error steps. Therefore, in addition to the main role of validation and optimization of the forming process, the FEA leads to more flexible manufacturing processes, combining reduced time-to market for new products and lower costs involved in its development – an

essential characteristic in competitive industries such as the automotive, aeronautical, military, among others (Badreddine, Labergère, & Saanouni, 2016).

The study of ductile fracture in the sheet forming process has gain increased importance in recent years. This trend, especially noticeable in the automotive industry, is closely related to the increasing usage of new materials with higher strength-to-weight ratio such as advanced high strength steels (AHSS). This family of steels, which includes dual phase steels (DP), transformation induced plasticity steels (TRIP) and martensitic steels (MS) (Keeler et al., 2014) have enhanced mechanical properties, namely yield stress and tensile strength, when compared to deep-drawing quality mild steels and conventional high-strength steels (HSS). This newly introduced materials allow to produce lighter structures and components from thinner sections and/or thicknesses, while maintaining satisfactory strength and stiffness, which ultimately results in a reduction of the overall structure mass, a crucial step to meet the ever-stringent standards on passenger safety and gas emissions (Badreddine et al., 2016; Pack, 2017). However, as is well-known, the increased mechanical strength of steels is usually accompanied by a *reduction of their ductility*. This phenomenon, complemented by the higher work hardening of AHSS, reduces the formability and crashworthiness of the components, since necking and fracture occurs for plastic strains smaller than the ones required by conventional steels. In fact, it has been experimentally verified that fracture can occur in AHSS without any evident sign of necking, which makes the common usage of the well-known Forming Limit Diagrams (FLDs) unfeasible (Badreddine et al., 2016). Thus, it is of the utmost interest the development of reliable numerical tools that accurately describe internal damaging and failure of ductile materials, either by necking onset or premature ductile fracture. As an example, Figure 1.1 shows the application of a damage model within a FEA of an engineering component.

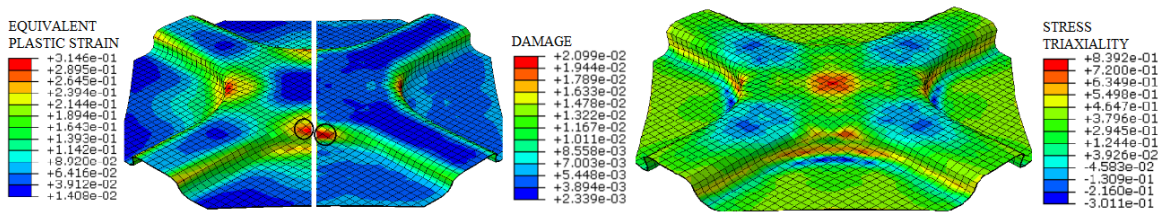

(a) (b)

Figure 1.1. FEA of a cross-shape component with damage prediction (a) Equivalent plastic strain and internal damage contours; (b) Stress triaxiality distribution before failure (Amaral et al., 2016).

To achieve this, the damage models must be able to capture the characteristic load-path dependent failure behaviour of ductile materials and provide reliable prediction of the stress and strain histories – crucial for predicting the onset of fracture (Roll, 2008). Simultaneously, such models should not present an overly complex formulation, which would lead to increased difficulties in their numerical implementation stage and in the calibration of the model parameters through experimental tests. In short, such tools must obtain accurate results in a reasonable computational time and be practical enough to be applicable to a fast-moving industry environment (Pack, 2017).

Finally, it should be mentioned that damage models can play a very important role in other technological areas. The widely used sheet metal blanking process, a manufacturing technology in which material separation is due to ductile fracture, can greatly benefit from improved damage criteria. Studies shown that sheet metal blanking simulations using damage models result in an improved prediction of the punch force and quality of the final product (Yoon, Stewart, & Cazacu, 2011). Moreover, the damage modelling and fracture prediction allows the design of lighter and safer structures through accurate crash simulations, which can also take into account the parts manufacturing process, and ultimately contribute to improve the crashworthiness of vehicles and aircrafts (Dunand, 2013).

1.2. A brief background on damage modelling for ductile fracture prediction

Before briefly discuss the existing alternatives for damage modelling, it is of all interest to clarify the meaning of the commonly mentioned terms *damage* and *ductile fracture*. The term *ductile fracture* is used to describe the rupture of a material that experiences large plastic deformation, exhibiting high ductility in the region where structural failure occurs. Ductile fracture is a physical process that results from the accumulation of plastic *damage* and leads to the formation and propagation of cracks in metals (Marcadet, 2015; Xue, 2007). In its turn, *damage* can be understood as the physical process of progressive deterioration of the material. At the microscopic level, damage is related to the mechanism of nucleation, growth and coalescence of micro-cracks and micro-cavities, evidenced by experimental observations. Macroscopically, damage translates into a decrease of the material stiffness, strength and a reduction of the remaining ductility. Damage is an

internal variable that usually cannot be measured directly or easily quantified, unlike the material's ductility or its fracture strain. Therefore, damage models are proposed to link field variables (e.g. strain tensor, stress tensor, stress triaxiality) to the progressive deterioration towards fracture, i.e. the damage evolution (Xue, 2007). This connection can be numerically simulated using either the so-called *uncoupled* or *coupled* damage models.

The *uncoupled models* assume the damage process as being independent of the material plastic behaviour, i.e. the plastic properties of the material do not change with the damage accumulation. This approach consists in carrying out a conventional FEA simulation and evaluate damage exclusively as a post-processing step of the finite element solution (Badreddine et al., 2016; Kiran & Khandelwal, 2014). Within this framework, damage accumulation is formulated empirically or semi-empirically through a separate scalar variable D, with the general criterion:

$$D = \int_0^{\bar{\varepsilon}_f^p} f(\boldsymbol{\sigma}, \boldsymbol{\varepsilon}^p)\, d\bar{\varepsilon}^p \geq D_c, \tag{1.1}$$

where $\bar{\varepsilon}^p$ is the equivalent plastic strain, $\bar{\varepsilon}_f^p$ is the critical value of equivalent plastic strain at fracture for a given loading path, $\boldsymbol{\sigma}$ is the Cauchy stress tensor and $\boldsymbol{\varepsilon}^p$ is the plastic strain tensor. The integrand $f(\boldsymbol{\sigma}, \boldsymbol{\varepsilon}_p)$, is the so-called weighting function of damage and represents a general function of the field variables, e.g. stress and strain tensors, stress triaxiality, etc. The weighting function is either chosen empirically or inspired by micromechanical results and can also account for thermal and strain rate effects. According to these models, fracture is considered to occur when the damage variable D, exceeds the critical damage value, D_c (Li, Fu, Lu, & Yang, 2011; Xue, 2007). Several uncoupled criteria, i.e. weighting functions have been develop. The reader is referred to the work of Ayada (1987); Cockcroft & Latham (1968); McClintock (1968); Rice & Tracey (1969); Wierzbicki, Bao, Lee, & Bai, (2005), among many others.

Uncoupled models often fail to predict the ductile fracture due to the over simplification of the mechanical behaviour of the material. Nevertheless, this approach can be used as a fast procedure for early development stages due to its simpler formulation, numeric implementation and parameters calibration (Teixeira, 2010; Xue, Pontin, Zok, & Hutchinson, 2010).

The *coupled models* approach incorporate damage accumulation in the constitutive equations. In other words, the plastic properties of the material are in fact considered as a function of the accumulated damage. Generally, coupled models can be classified in two main categories: micromechanical-based (or physical-based) and damage-based (or phenomenological) models (Kiran & Khandelwal, 2014).

The *micro-mechanical damage models* treat the materials as a cluster of inhomogeneous cells. It is well-known that microstructure of metals is characterized by the presence of multiphase materials, such as precipitates, second phase particles, impurities and voids. The void distribution is a function of pre-existing voids (e.g. manufacturing defects) and of the nucleation by decohesion of second-phase particles and/or by particle fracture. The void grow results from the plastic deformation of the surrounding matrix material. Micromechanical-based damage models take advantage of the intimate relationship between material porosity and ductile failure: the ability to accurately describe the evolution of the void distribution in a ductile metal allows to accurately predict the failure of the material (Stewart, 2009). Due to computational constraints, the approach of modelling each of the micro-voids in the material is not practical at this time. Thus, instead of explicitly tracking the microscopic evolution of each void, the mechanical behaviour of the micro-voids is incorporated into macroscopic, or average, properties (such as macroscopic stress, strain, yielding, etc.) (Stewart, 2009). In this analysis, a void is modelled surrounded by undamaged material (the matrix material, which obeys conventional continuum mechanics) in a representative volume element (RVE) also known as unit cell (Xue, 2007). The macroscopic behaviour of the macroscopic material is then obtained through a homogenization procedure, where an analytic expression is derived for the plastic potential (and, thus, for the yield criterion, when assuming associated plasticity) (Stewart, 2009). Due to the enormous combination of the possible size, shape, orientation and spacing of the voids and of the RVE geometry, simplifications and assumptions have to be made to make the mathematical problem of void evolution tractable (Xue, 2007). The most widely used plastic potential for porous solids is related with the original work developed by Gurson (1977). In Gurson-like micromechanics-based criteria, the behaviour of a void-containing solid is described by the pressure-sensitive plastic flow, and the internal damage variable is employed in the constitutive equations, interacting with the other state variables. In these criteria, the internal damage variable is the void volume fraction, defined as the ratio between the accumulated

volume of individual voids and the total volume of the RVE (Li & Karr, 2009). The fracture is considered to occur then the void volume fraction reaches a critical value. The Gurson model and its extensions will be further explored and discussed in more detail in following chapters.

The *damage-based models* framework, or phenomenological approach, is based on the classical Continuum Damage Mechanics (CDM) theory proposed by Lemaitre (1984). In this framework, the material degradation resulting from the mechanism of nucleation, growth and coalescence of micro-voids is described using a purely phenomenological model derived from the first and second principles of thermodynamics for continuous media (Badreddine et al., 2016; Dunand, 2013). CDM-based criteria introduce a macroscopic damage indicator in the constitutive relationships as an internal variable to describe the damage evolution and progressive degradation of the material (Li et al., 2011). The internal damage state variable affects both the elastic behaviour and the plastic flow, through the so-called *effective stress*, based either on the strain equivalence principle or the energy equivalence principle (Chaboche, Boudifa, & Saanouni, 2006). In opposition to micro-mechanical models, the constitutive and damage models of the material is based on the externally observed behaviour of the material, as the growth of individual void and their interactions are depicted in a phenomenologically aggregative way (Xue, 2007). Compared to Gurson-like micromechanical models, CDM models are relatively simpler to apply since, due to its phenomenological nature, the identification of the material parameters is more intuitive and typically fewer measurements are involved (Li et al., 2011).

When compared to uncoupled damage models, coupled models represent a sounder physical background of the micromechanical fracture and, therefore, typically allow to obtain more reliable results in the ductile fracture prediction. However, the coupled models are more difficult to implement in an FEA code and usually require a greater computational effort.

The selection of the damage model to apply in a numerical simulation is a non-trivial issue. The applicability and reliability of a model must be confronted with its computational cost and calibration difficulty (Wierzbicki et al., 2005). The inappropriate application of damage models may result in misleading ductile fracture predictions, which has been a problematic issue in industrial applications of both the coupled and uncoupled alternatives (Li et al., 2011).

1.3. Objectives of the work

The aim of this study is to evaluate the ability of a coupled micromechanical damage model – the so-called CPB06 porous model, to describe the damage accumulation and, ultimately, final failure of ductile materials exhibiting tension-compression asymmetry. The predictive ability of the isotropic form of the abovementioned constitutive damage model is assessed through elementary numerical simulations, under axisymmetric and hydrostatic stress states. A qualitative comparison between the numerical predictions obtained by the damage model and by micromechanical finite element computations on three-dimensional unit cells, documented in the literature, is performed. In order to support and substantiate the numerical results, a sensitivity analysis of the damage model yield criterion parameters is firstly carried out based on the yield loci change of shape and size, when varying material and/or damage parameters. Both two-dimensional and three-dimensional representations of the yield surfaces are analysed. These are used to analyse the influence of the stress state through the stress triaxiality, hydrostatic stress and the sign of third invariant of the deviatoric stress tensor, particularly for axisymmetric loadings. The damage model response through elementary numerical tests is complemented with a brief sensitivity analysis regarding the matrix isotropic hardening law parameters. All numerical simulations were performed with the in-house finite element solver DD3IMP, specifically developed for simulating sheet metal forming processes (Menezes & Teodosiu, 2000).

In summary, the present work intends to provide a contribution to the evaluation of the applicability and reliability of the CPB06 coupled damage model on the ductile fracture prediction, investigating its main features and highlighting the importance of the yield loci shape, through the role played by all stress invariants, on the damage evolution and ultimately, on the onset of failure.

1.4. Layout of the thesis

This section presents a summary of the contents covered in this work. The thesis comprises of two main parts, organized into six chapters. The former corresponds to the literature review and contains Chapter 2 and Chapter 3; the latter covers the investigations conducted within the framework of this study, corresponding to Chapter 4, Chapter 5 and Chapter 6. Following the general introduction and motivation presented in this first chapter, the layout of the thesis is as follows.

Chapter 2 sets out the basic concepts describing the physical mechanisms of the ductile crack formation. Some well-known coupled micromechanical damage models and relevant extensions are briefly presented, discussion their advantages and possible drawbacks. The description of the stress state in the fracture mechanics framework is also presented.

Chapter 3 presents the anisotropic and isotropic version of the Cazacu, Plunkett & Barlat (2006) yield criterion, used to describe the tension-compression asymmetry displayed by the matrix material. Next, the Stewart & Cazacu's (2011) plastic potential for random distributed spherical voids is introduced. Both anisotropic and isotropic versions of this coupled damage model are analysed. The expressions of the damage model resulting for the particular case of axisymmetric stress states are briefly discussed.

Chapter 4 is devoted to the sensitivity analysis of the Cazacu & Stewart's (2009) isotropic damage model parameters, based on three-dimensional representations of the yield surfaces and corresponding two-dimensional projections on the deviatoric plane and on the axisymmetric plane.

Chapter 5 describes the numerical analyses conducted in order to assess the ability of the damage model to describe the plastic flow of the matrix and the accumulated damage in porous solids exhibiting tension–compression asymmetry. The numerical model and the methodology adopted in the analysis are briefly discussed. A detailed analysis of the results is performed and the main findings of this study are presented. Lastly, a sensitivity analysis is performed regarding the matrix isotropic hardening law parameters.

Chapter 6 presents a short summary of the issues addressed in the study and the main conclusions withdrawn from it, along with suggestions for future research.

For the sake of improving the main topics presentation, while allowing the reader to access all the important details, the work also includes the following supplements:

Annex A provides the method proposed by Barlat et al. (2005) for the determination of the ordered principal values of the CPB06 transformed stress tensor.

Annex B describes the method proposed by Revil-Baudard et al. (2016) to compute the components of the forth-order anisotropic inverse of the CPB06 linear-transformed tensor, required to determine the hydrostatic factor of the CPB06 porous model.

Appendix A contains several expressions and relationships for the damage model parameters, derived for the particular case of axisymmetric stress states.

2. Coupled Micromechanical-Based Damage Models

This chapter provides an overview of the general concepts governing the physical mechanism of the ductile crack formation, emphasizing the complexity and the consequent difficulties associated with the description of the ductile fracture process. Following this literature review, the description of the stress state in the fracture mechanics framework is presented. Finally, the original Gurson (1977) micromechanical damage model and some of its extensions are presented, discussing the main features and drawbacks of this approach.

2.1. Physical mechanisms of the ductile crack formation

As outlined in the introductory chapter, ductile fracture can be described as a three stage process: nucleation, growth and coalescence of micro-voids (see e.g. McClintock (1968) and Rousselier (1987)). In this section each stage of this physical mechanism will be reviewed in detail.

The void distribution in a material originates from pre-existing voids or from *nucleation* at second-phase particles, either by matrix-particle decohesion or by particle cracking (e.g. inclusions, impurities). It is generally observed that voids nucleate preferably in larger second-phase particles due to higher local stress fields generated by the presence of larger rigid inclusions, when the matrix undergoes plastic deformation, and due to the increased number and size of geometrical defects at this larger particles, leading to easier micro-crack formation in the particles. Void nucleation could also occur in shear bands (Bao, 2003). Following nucleation, voids will grow and eventually link.

It is well-known that the stress triaxiality – defined by the ratio between the mean stress and the equivalent stress – is the most important parameter governing ductile crack formation (Bao, 2003). The mean stress (or hydrostatic stress), which has little or no influence on the overall plastic deformation in the absence of damage, i.e. in fully dense materials, exhibits a dramatic effect on the ductile fracture mechanism of porous materials, particularly on the void growth and coalescence stages (Nahshon & Hutchinson, 2008). According to McClintock (1968) the size, shape and spacing of the voids depends on the

entire stress and strain history. Indeed, the physical mechanism of *void growth* and final linkage is governed by the microstructure of the material and loading conditions. Under shear dominated loads, i.e. low stress triaxiality, the voids undergo a rotation and a change of shape, which makes them lose their initially spherical shape. Since rotation of voids does not change the void volume fraction, the macroscopic dilation of the voids is minimal. In this case, there is a relatively small dilatational growth (or change of volume) and the ductile fracture is mainly due to large "deviatoric" or shape changing void growth (Bao, 2003). On the other hand, under high stress triaxiality, the change of volume dominates the contribution to void growth over the shape changing effect and, therefore, voids retain their initial shape (Besson, 2010; Rice & Tracey, 1969).

In addition to the different processes of void nucleation and void growth previously mentioned, different processes of void linkage, also known as *void coalescence*, have been experimentally observed. When the voids grow so large that they begin to interact with each other, the deformation becomes highly localized (Xue, 2007). Void linkage can occur through three phenomena: *internal necking* of the matrix between voids, simple touching of two voids (*void impingement*) and due to the so-called *void sheet* mechanism (Bao, 2003). These ductile failure micro-mechanisms lead to the formation of macroscopic cracks and, ultimately, the macroscopic failure of the material. Figure 2.1 highlights the internal necking and the void sheet mechanisms – the more commonly observed coalescence modes. Failure by internal necking of the matrix occurs mainly at high stress triaxiality and is due to inter-void ligament necks of large primary voids.

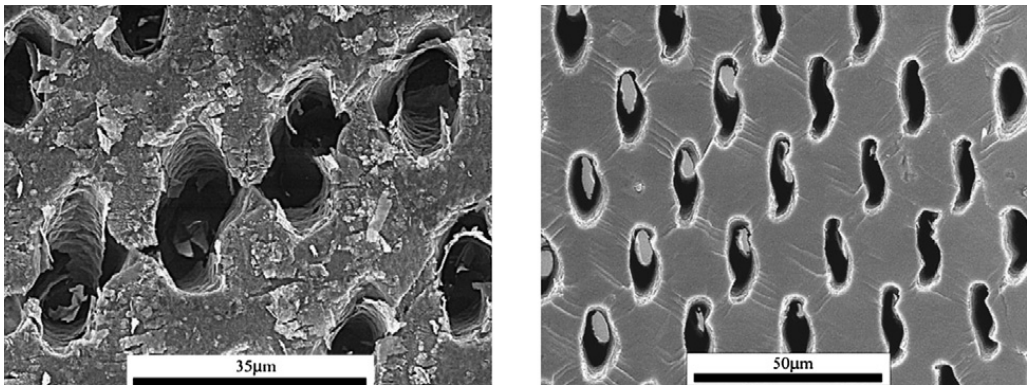

(a) (b)

Figure 2.1. Two ductile failure micro-mechanisms (after Weck et al., 2006): (a) inter-void ligament necking; (b) void sheeting mechanism.

When a material contains several populations of inclusions corresponding to different length scales, failure by void sheeting can also occur. In this void coalescence mode, also known as shear coalescence, shear banding occurs at the scale of the voids. In this mechanism, active at low stress triaxiality, the linkage between primary voids and micro-crack propagation is accelerated due to the nucleation of secondary voids at highly concentrated shear bands induced by the stress concentration effect at the ends of the micro-crack and by shear dominated loadings (Besson, 2010). This plastic shear localization weakens the total aggregate of material and promotes inter-void ligaments of smaller, elongated and rotated voids. It should be noted that "shear coalescence" is just the name for this type of mechanism and it does not mean that this type of micro-mechanical failure is exclusively due to shear loadings.

At intermediate stress triaxialities there is a combined effect of volumetric and shape changes of the voids as both internal necking and void sheet mechanisms are active. In other words, the intermediate stress triaxiality range is a transition range (Bao, 2003).

Experimental observations on steels and aluminium alloys shown that the void sheet mechanism can cause inter-void ligament failure before void touching takes place, (which would require a distribution of larger voids) (Hammi & Horstemeyer, 2007). Void coalescence modelling has received less attention in the literature than void nucleation and void growth mainly because of the lack of definition and difficulty in quantifying this behaviour. In fact, although there are well-established micromechanical-based damage models that consider void coalescence due to the internal necking of the matrix (e.g. McClintock (1968) and Rice & Tracey (1969)) and due to simple void contact (e.g. Gurson (1977)), no good void sheet mechanism modelling has been developed (Bao, 2003). So far, void shearing damage criteria have been mostly modelled through heuristic approaches, based on the know-how rather than deep scientific analysis (Li et al., 2011).

Despite the great relevance of the stress triaxiality on ductile fracture mechanics, FEA on unit cells (e.g. Cazacu & Stewart (2009) and Alves, Revil-Baudard & Cazacu (2014)) as well as Fast Fourier Transform (FFT)-based approaches (e.g. Lebensohn & Cazacu (2012)) have shown that the stress triaxiality by itself can be insufficient to characterize the yielding of porous materials. In these studies was shown that, for the same triaxiality, the yielding and the rate of void growth depend not only on the first and second invariants of the stress and deviatoric stress tensors, respectively, but also on the sign of the third invariant of the

stress deviator – a relationship often referred in the literature as "*Lode angle dependence*" (Xue, 2007). In the past decade, experimental data has supported this evidence, recognizing and highlighting the role played by all stress invariants in the yielding of porous materials and, consequently, in the ductile fracture prediction (Alves et al., 2014; Malcher, 2012).

The ductile fracture phenomena briefly reviewed in this section show that appropriate modelling of these physical mechanisms is by no means trivial, especially when volumetric and shear effects are combined through complex strain paths (Malcher, 2012). Observations of the physical process of ductile fracture have allowed the development of damage models and procedures for fitting the models parameters, in order to perform numerical simulations. Nowadays, recent developments of X-ray tomography allows to gather real-time 3D data of the evolution of damage (e.g. void shape, rotation, growth, linkage, etc.). Using this method, error on damage quantification induced by conventional surface preparation techniques can be avoided (Babout, Maire, Buffière, & Fougeres, 2001), leading to a better understanding of the process and enhanced damage criteria developments (Besson, 2010).

2.2. Description of the stress state

A stress state is fully defined by the six independent components of the Cauchy stress tensor. Regarding the study of ductile fracture mechanics, the stress state is usually described by two dimensionless parameters: the stress triaxiality, T_Σ and the normalized Lode angle, $\bar{\theta}_\Sigma$. Letting $\boldsymbol{\Sigma}$ be the macroscopic principal stress tensor with the diagonal components Σ_1, Σ_2 and Σ_3 ordered such that $\Sigma_1 \geq \Sigma_2 \geq \Sigma_3$, the mean stress, Σ_m can be defined as:

$$\Sigma_m = \frac{1}{3} I_1^\Sigma = \frac{1}{3}\mathrm{tr}(\boldsymbol{\Sigma}) = \frac{1}{3}(\Sigma_1 + \Sigma_2 + \Sigma_3), \tag{2.1}$$

where tr($\cdot$) denotes the trace of a tensor and I_1^Σ is the first invariant of the stress tensor. The macroscopic deviatoric stress tensor, $\boldsymbol{\Sigma}'$ is given by:

$$\boldsymbol{\Sigma}' = \boldsymbol{\Sigma} - \Sigma_m \mathbf{I} = \begin{bmatrix} \Sigma_1 - \Sigma_m & 0 & 0 \\ 0 & \Sigma_2 - \Sigma_m & 0 \\ 0 & 0 & \Sigma_3 - \Sigma_m \end{bmatrix}, \tag{2.2}$$

with $\mathbf{I}$ being the second-order identity tensor. Therefore, the second and third deviatoric stress invariants, respectively J_2^Σ and J_3^Σ can be written as:

$$J_2^\Sigma = \frac{1}{2}(\Sigma_1'^2 + \Sigma_2'^2 + \Sigma_3'^2), \tag{2.3}$$

$$J_3^{\Sigma} = \Sigma_1^{'}\Sigma_2^{'}\Sigma_3^{'}. \tag{2.4}$$

The von Mises equivalent stress, Σ_e can be represented as a function of the second deviatoric stress invariant, J_2^{Σ} as:

$$\Sigma_e = \sqrt{3J_2^{\Sigma}}, \tag{2.5}$$

Thus, the stress triaxiality, T_{Σ} is defined as the ratio of the mean stress and equivalent von Mises stress, i.e.:

$$T_{\Sigma} = \frac{\Sigma_m}{\Sigma_e}, \tag{2.6}$$

with $-\infty \le T_{\Sigma} \le \infty$. Note that for purely deviatoric loadings $(I_1^{\Sigma} = 0)$, results while for purely hydrostatic loadings at tension or compression $(J_2^{\Sigma} = 0)$, results that $T_{\Sigma} \to \infty$ or $T_{\Sigma} \to -\infty$, respectively.

The so-called normalized third invariant of the deviatoric stress tensor, ξ_{Σ} lies in the range $-1 \le \xi_{\Sigma} \le 1$ and characterizes the position of the second principal macroscopic stress, Σ_2 with respect to the maximum and minimum principal stresses, Σ_1 and Σ_3 (Dunand, 2013), such that:

$$\xi_{\Sigma} = \frac{3\sqrt{3}}{2}\frac{J_3^{\Sigma}}{\left(J_2^{\Sigma}\right)^{3/2}}. \tag{2.7}$$

Another way to establish this relationship is through a parameter known as Lode angle, θ_{Σ} that can be defined as:

$$\theta_{\Sigma} = \arctan\left\{-\frac{1}{\sqrt{3}}\left[2\left(\frac{\Sigma_2^{'} - \Sigma_3^{'}}{\Sigma_1^{'} - \Sigma_3^{'}}\right) - 1\right]\right\}, \tag{2.8}$$

which, by its turn, can also be written as a function of the normalized third invariant of the deviatoric stress tensor, ξ_{Σ} as:

$$\theta_{\Sigma} = \left(\frac{\pi}{6} - \frac{1}{3}\arccos\left(\xi_{\Sigma}\right)\right) = \frac{1}{3}\arcsin\left(\xi_{\Sigma}\right). \tag{2.9}$$

when defined in this way, the Lode angle ranges between $-\pi/6 \le \theta_{\Sigma} \le \pi/6$, such that $\theta_{\Sigma} = \pi/6$ $(\xi_{\Sigma} = 1)$ corresponds to a uniaxial tension loading and $\theta_{\Sigma} = -\pi/6$ $(\xi_{\Sigma} = -1)$ to a uniaxial compression loading. In the same spirit as J_3^{Σ}, this parameter can be normalized, resulting in the so-called normalized Lode angle or *Lode angle parameter*, $\overline{\theta}_{\Sigma}$ given in this case by:

$$\bar{\theta}_{\Sigma} = \frac{6\theta_{\Sigma}}{\pi}, \tag{2.10}$$

or, alternatively, as a function of the normalized third invariant of the stress deviator, ξ_{Σ} as:

$$\bar{\theta}_{\Sigma} = \left(1 - \frac{2}{\pi}\arccos\left(\xi_{\Sigma}\right)\right) = \frac{2}{\pi}\arcsin\left(\xi_{\Sigma}\right). \tag{2.11}$$

Similarly to the parameter ξ_{Σ}, the Lode angle parameter also varies in the range $-1 \le \bar{\theta}_{\Sigma} \le 1$.

A stress state represented in a three-dimensional Cartesian system $(\Sigma_1, \Sigma_2, \Sigma_3)$ can be translated in to an equivalent cylindrical coordinate system, with coordinates $(\Sigma_e, \theta_{\Sigma}, \Sigma_m)$. This transformation is exemplified in Figure 2.2 (a), underlining the hydrostatic axis direction and the definition of the π-plane[1]. This cylindrical coordinate system is also referred as the Haigh–Westergaard coordinates. In the π-plane, the Lode angle is defined as the smallest angle formed between the pure shear line segment and the projection of the actual stress tensor on the deviatoric plane, as shown in Figure 2.2 (b) (Malcher, 2012). Therefore, the Lode angle can be understood as a quantification of the proximity (or remoteness) of the current stress state relative to the pure-shear stress state, i.e. the position of the second principal macroscopic stress in the interval defined by the maximum and minimum principal stresses: $\Sigma_1 \ge \Sigma_2 \ge \Sigma_3$.

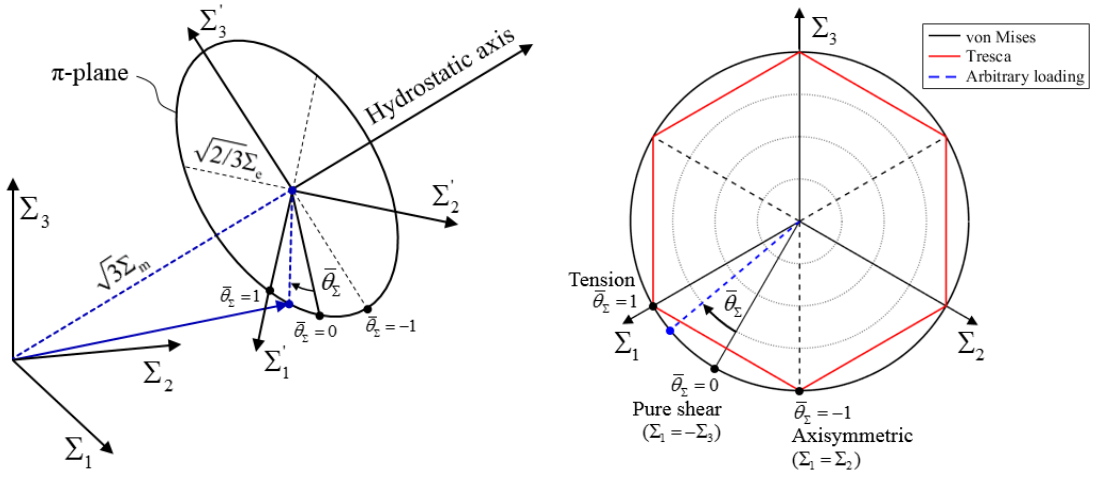

Figure 2.2. Geometrical definition of the Lode angle parameter: (a) Three-dimensional Cartesian system and the corresponding cylindrical coordinate system; (b) π-plane representation.

[1] As known as *deviatoric plane* or *octahedral plane*; plane normal to the hydrostatic axis, defined by the normal $\mathbf{n} = (1/\sqrt{3})\mathbf{e}_1 + (1/\sqrt{3})\mathbf{e}_2 + (1/\sqrt{3})\mathbf{e}_3$, where $(\mathbf{e}_1, \mathbf{e}_2, \mathbf{e}_3)$ is the Cartesian coordinate system associated with the principal directions of the stress tensor.

One can conclude that a stress state can be partially defined by a combination of the above parameters: $(T_\Sigma, \bar{\theta}_\Sigma)$. Indeed, the direction of the vector defined by the principal stress tensor can be unequivocally expressed by these pair of parameters. Hence, throughout the thesis, the term "stress state" will refer to these widely used adimensional parameters in the fracture mechanics framework. Some of the stress states with great importance for the sheet metal forming process are mentioned bellow:

- Pure-shear ($T_\Sigma = 0,\ \bar{\theta}_\Sigma = 0$);
- Uniaxial tension ($T_\Sigma = 1/3,\ \bar{\theta}_\Sigma = 1$);
- Uniaxial compression ($T_\Sigma = -1/3,\ \bar{\theta}_\Sigma = -1$);
- Plane strain tension ($T_\Sigma = 1/\sqrt{3},\ \bar{\theta}_\Sigma = 0$);
- Equibiaxial tension ($T_\Sigma = 2/3,\ \bar{\theta}_\Sigma = -1$);
- Equibiaxial compression ($T_\Sigma = -2/3,\ \bar{\theta}_\Sigma = 1$).

2.3. Gurson-like micromechanical damage models

The first micromechanical ductile damage models where developed by McClintock (1968) and Rice & Tracey (1969) to describe the growth of isolated cylindrical or spherical voids in a rigid perfectly plastic matrix. These pioneer uncoupled criteria outlined the combined role of the stress triaxiality and the plastic strain on the void growth. Being uncoupled models, these prior studies did not consider the effects of the void growth on the material behaviour, i.e. neglected the softening effects (Besson, 2010). This problem was firstly addressed by Gurson (1977), which developed a coupled micromechanical-based model by introducing a new yield function which strongly links the plastic behaviour with the damage accumulation (Chaboche et al., 2006). Gurson developed analytic yield criteria for ductile materials containing either spherical or cylindrical voids. To obtain the plastic potentials, and thus, the yield criteria, Gurson performed an upper bound limit load analysis on the RVEs (spherical void within a spherical shell RVE or a cylindrical void within a cylindrical tube RVE), assuming a rigid perfectly plastic matrix material (undamaged/void free material) obeying the classic pressure-insensitive von Mises criterion (Besson, 2010). Gurson's criteria are an upper bound of the exact plastic potential, since the minimization of the plastic energy was done for a specific velocity field compatible with uniform strain rate boundary conditions, rather than for the complete set of kinematically admissible velocity

fields (Stewart, 2009). The mathematical details of the analysis are rather complex (Chaboche et al., 2006). When assuming an associated flow rule, the result is a plastic pressure-sensitive yield surface which takes into account the damage accumulation, given for spherical voids as:

$$\varphi_{\mathrm{G}}^{\mathrm{S}} = \left(\frac{\Sigma_{\mathrm{e}}}{\sigma_{\mathrm{Y}}}\right)^2 + 2f\cosh\left(\frac{3\Sigma_{\mathrm{m}}}{2\sigma_{\mathrm{Y}}}\right) - 1 - f^2 = 0, \tag{2.12}$$

and for cylindrical voids as:

$$\varphi_{\mathrm{G}}^{\mathrm{C}} = C_{\mathrm{eqv}}\left(\frac{\Sigma_{\mathrm{e}}}{\sigma_{\mathrm{Y}}}\right)^2 + 2f\cosh\left(\frac{\sqrt{3}\Sigma_{\gamma\gamma}}{2\sigma_{\mathrm{Y}}}\right) - 1 - f^2 = 0, \tag{2.13}$$

where

$$C_{\mathrm{eqv}} = \begin{cases} \left(1 + 3f + 24f^6\right)^2 & \text{for plane strain,} \\ 1 & \text{for axisymmetry.} \end{cases} \tag{2.14}$$

In the previous expressions, Σ_{e} is the macroscopic von Mises equivalent stress, Σ_{m} is the macroscopic mean stress or hydrostatic stress, σ_{Y} is the yield stress of the undamaged material, $\Sigma_{\gamma\gamma}$ is the sum of the in-plane stresses (e.g. $\Sigma_{\gamma\gamma} = \Sigma_{11} + \Sigma_{22}$ if the 3-direction is the out-of-plane direction) and f is the void volume fraction (or porosity), which quantifies the current damage and is defined by the ratio of the void volume to the total volume of the RVE. Note that, unlike von Mises yield criterion, Gurson's criteria depend not only on the second invariant of the stress deviator, but also on the pressure (or the mean stress), i.e. on the first invariant of the stress tensor. However, in the absence of voids ($f = 0$), these criteria reduce to that of the matrix, i.e. the von Mises yield surface. Gurson's spherical void criterion is considered more often in the literature than the cylindrical void criterion. Even so, the latter can be applied to certain problems, for example plane stress analysis of sheet metal (Stewart, 2009).

The matrix material is described by a convex yield function in the stress space. The macroscopic plastic strain rate tensor, $\mathbf{D}^{\mathrm{p}}$ is determined through the normality rule, assuming an associated flow rule, as:

$$\mathbf{D}^{\mathrm{p}} = \dot{\lambda}\frac{\partial\varphi}{\partial\boldsymbol{\Sigma}}, \tag{2.15}$$

where $\boldsymbol{\Sigma}$ is the macroscopic Cauchy stress tensor and $\dot{\lambda} \geq 0$ the rate of the plastic multiplier. Assuming the equivalence of microscopic and macroscopic inelastic work (i.e. equivalence

of the rate of plastic work), the rate of the microscopic/local effective plastic strain, $\dot{\bar{\varepsilon}}_{\mathrm{M}}^{\mathrm{p}}$ is obtained as:

$$\boldsymbol{\Sigma} : \mathbf{D}^{\mathrm{p}} = (1-f)\sigma_{\mathrm{M}}\dot{\bar{\varepsilon}}_{\mathrm{M}}^{\mathrm{p}}, \tag{2.16}$$

where σ_{M} is the flow stress of the matrix, following a given hardening law. Combining the above expressions results:

$$\dot{\bar{\varepsilon}}_{\mathrm{M}}^{\mathrm{p}} = \dot{\lambda}\frac{\boldsymbol{\Sigma} : \dfrac{\partial \varphi}{\partial \boldsymbol{\Sigma}}}{(1-f)\sigma_{\mathrm{M}}}. \tag{2.17}$$

The void volume fraction rate, $\dot{f}$ evolves both from the nucleation and the growth of existing voids such that:

$$\dot{f} = \dot{f}_{\text{growth}} + \dot{f}_{\text{nucleation}}, \tag{2.18}$$

where the rate of change due to the growth of existing voids, $\dot{f}_{\text{growth}}$ is obtained from the plastic incompressibility of the matrix material, i.e. *mass conservation principle* as:

$$\dot{f}_{\text{growth}} = (1-f)\mathbf{D}^{\mathrm{p}} : \mathbf{I} = (1-f)D_{kk}^{\mathrm{p}}, \text{ with } f(t_0) = f_0, \tag{2.19}$$

where ":" denotes the tensor double contraction. Thus, D_{kk}^{p} is the trace of the macroscopic plastic strain rate tensor, $\mathbf{D}^{\mathrm{p}}$ which represents the macroscopic plastic strain rate. In the previous expression, f_0 corresponds to the initial void volume fraction at the time instant t_0. Note that the evolution law for the damage variable *f*, is entirely determined by the definition of the yield surface (Besson, 2010). Indeed, in Gurson-like criteria, the physical mechanisms of ductile fracture (void nucleation, growth and coalescence) is modelled by explicitly monitoring the void volume fraction, which accounts for the reduction of the load-bearing area and subsequent softening effect.

The void volume fraction rate of change due to nucleation, $\dot{f}_{\text{nucleation}}$ was one of the first extensions proposed to the original Gurson model. Void nucleation can be modelled as stress-controlled, as discussed in Argon, Im & Safoglu (1975) or strain-controlled as suggested by Gurson (1975) and is generally written as:

$$\dot{f}_{\text{nucleation}} = A_{\mathrm{N}}\dot{\bar{\varepsilon}}_{\mathrm{M}}^{\mathrm{p}} + B_{\mathrm{N}}\dot{\Sigma}_{\mathrm{m}} \tag{2.20}$$

Both plastic strain controlled nucleation and mean stress controlled nucleation are frequently considered in a statistical way, following a normal distribution as suggested by Chu & Needleman (1980). The proportionally constants A_{N} and B_{N} are given by:

$$A_{\mathrm{N}} = \begin{cases} \dfrac{f_{\mathrm{N}}}{s_{\mathrm{N}}\sqrt{2\pi}} \exp\left[-\dfrac{1}{2}\left(\dfrac{\bar{\varepsilon}_{\mathrm{M}}^{\mathrm{p}} - \varepsilon_{\mathrm{N}}}{s_{\mathrm{N}}} \right)^2 \right] & \text{if } \Sigma_{\mathrm{m}} \geq 0, \\ 0 & \text{if } \Sigma_{\mathrm{m}} < 0; \end{cases} \tag{2.21}$$

$$B_{\mathrm{N}} = \begin{cases} \dfrac{f_{\mathrm{p}}}{s_{\mathrm{p}}\sqrt{2\pi}} \exp\left[-\dfrac{1}{2}\left(\dfrac{\Sigma_{\mathrm{m}} - \sigma_{\mathrm{p}}}{s_{\mathrm{p}}} \right)^2 \right] & \text{if } \dot{\Sigma}_{\mathrm{m}} \geq 0, \\ 0 & \text{if } \dot{\Sigma}_{\mathrm{m}} < 0; \end{cases} \tag{2.22}$$

where ε_{N} and σ_{p} are the mean values of the Gaussian distribution, s_{N} and s_{P} are the standard deviations and f_{N} and f_{p} represent the total void volume fraction that can be nucleated by the plastic strain rate and by the mean stress rate, respectively.

Based on finite element unit cell computations, a widely used modification of the Gurson's spherical yield criterion was suggested by Tvergaard (1981) and Tvergaard (1982):

$$\varphi = \left(\frac{\Sigma_{\mathrm{e}}}{\sigma_{\mathrm{M}}} \right)^2 + 2q_1 f \cosh\left(q_2 \frac{3\Sigma_{\mathrm{m}}}{2\sigma_{\mathrm{M}}} \right) - 1 - q_3 f^2 = 0. \tag{2.23}$$

The adjustments to the original Gurson's model proposed by Tvergaard were established through the introduction of new parameters – the fitting parameters q_i (all equal to one in Gurson's original expression). These parameters can be thought of as an adjustment of the yield surface to account for the influence of neighbouring voids, hence designated as void interaction parameters (Kiran & Khandelwal, 2014; Stewart, 2009). Based on finite element unit cell simulations, Tvergaard recommended values of $q_1 = 1.5$, $q_2 = 1$ and $q_3 = q_1^2$. Perrin & Leblond (1990) have determined a correlation between the fitting parameters q_i and the porosity f and showed that when the porosity tends to zero, q_1 value tends to $4/e \cong 1.47$, with $q_2 = 1$ and $q_3 = q_1^2$, i.e. the results are very similar to the ones originally suggested by Tvergaard (Benseddiq & Imad, 2008; Stewart, 2009). Faleskog, Gao & Shih (1998) have shown that the fitting parameters also depend on the matrix flow properties, namely the plastic hardening exponent, n and the ratio of the yield stress over the Young's modulus, σ_{Y}/E. These authors showed that, regardless of the flow properties of the matrix, the product $q = q_1 q_2$ for the optimal values of the fitting parameters is approximately constant and equal to 1.5, which again agrees with the values proposed by Tvergaard (Benseddiq & Imad, 2008).

According to the modified Gurson yield criterion presented above (see Equation (2.23)), the complete loss of load carrying capacity occurs at $f = 1/q_1$ which is unrealistically larger than experimental observations (Xue, 2007). In order to model the complete loss of load carrying capacity at a realistic level of the void volume fraction, Tvergaard & Needleman (1984) further modified Gurson's spherical yield criterion to account for the onset of void coalescence leading to final material fracture. This model is often referred to as the Gurson–Tvergaard–Needleman (GTN) model. The GTN criterion is given by:

$$\varphi = \left(\frac{\Sigma_e}{\sigma_M}\right)^2 + 2q_1 f^* \cosh\left(q_2 \frac{3\Sigma_m}{2\sigma_M}\right) - 1 - q_3 \left(f^*\right)^2 = 0, \tag{2.24}$$

where f^* is the so-called *effective* void volume fraction. The newly introduced internal damage variable is a function of the *actual* void volume fraction, f and is given as:

$$f^*(f) = \begin{cases} f & \text{if} \quad f < f_c, \\ f_c + q_\delta (f - f_c) & \text{if} \quad f \geq f_c. \end{cases} \tag{2.25}$$

In the expression above, f_c is the critical void volume fraction of a material at which the material stress carrying capacity starts to decay rapidly, i.e. the trigger for the void coalescence, and q_δ is the accelerating factor, introduced in order to describe the final stage of ductile failure, defined by:

$$q_\delta = \frac{f_U^* - f_c}{f_F - f_c}, \tag{2.26}$$

where f_F is the void volume fraction at final failure and f_U^* is the ultimate value of the effective void volume fraction, i.e. the effective void volume fraction at which occurs the complete loss of macroscopic stress carrying capacity, such that $f_U^* = 1/q_1$ if $q_3 = q_1^2$, as suggested by Tvergaard. The damage evolution predicted by the GTN model (see Equation (2.25)) is illustrated graphically in Figure 2.3, where it is clearly shown that as the actual void volume fraction tends to the value at final failure, $(f \to f_F)$, the effective void volume fraction tends to its ultimate value, $(f^* \to f_U^*)$.

In summary, the GTN model has a total of nine parameters: (i) the *void interaction parameters*: q_1, q_2 and q_3; (ii) the *material parameters* which can be classified in: (a) the initial void volume fraction, f_0 and the void nucleation parameters (f_N, ε_N, s_N) for strain-controlled nucleation or (f_p, ε_p, s_p) for stress-controlled nucleation; and (b) *ductile fracture parameters*: the critical and final failure parameters, f_c and f_F, respectively.

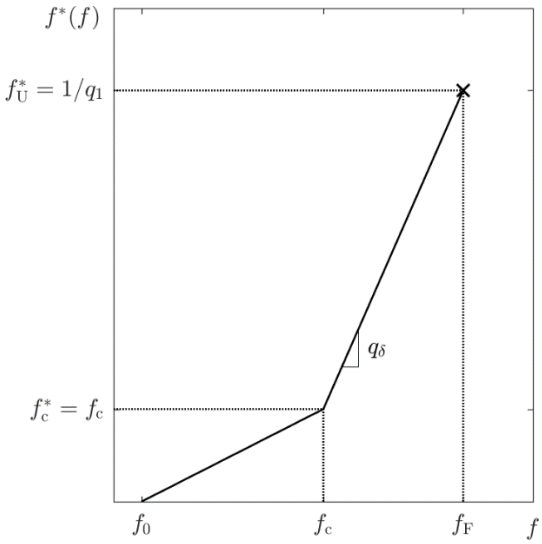

Figure 2.3. Effective void volume fraction concept introduced by Tvergaard and Needleman (1984); GTN model damage evolution.

As discussed in the previous section, the coalescence phenomenon is a highly complex physical mechanism, that even today lacks theoretical definition and is challenging to quantify. The effective void volume fraction concept introduced by Tvergaard & Needleman (1984) to formulate the GTN model accounts for coalescence in a rather basic but efficient way (Besson, 2010). When properly calibrated for a specific material, Gurson-like models have shown considerable potential for characterizing damage evolution and fracture prediction (Xue et al., 2010). Despite the success of Gurson-type criteria on many applications, there are some drawbacks associated with these models:

i. No void shearing mechanism is considered: the presented Gurson models are unable to predict fracture under shear-dominated loading conditions (low stress triaxiality), where the void growth mechanism is inactive and void sheeting dominates. Indeed, under pure shear loadings, the GTN model will fail to predict any void growth and thus, predict the ductile failure, if $f_N < f_F$ (the nucleation potential does not exceed the void volume fraction at failure). Gurson-like models were conceived to be applied at high stress triaxiality loadings, where pressure sensitivity (the mean stress) dominates the fracture phenomenon. The application of these models at low stress triaxialities should be used with caution;

ii. The damage accumulation in ductile materials is a more complex phenomenon than solely track the evolution of the void volume fraction, e.g. the presence of a volume-less micro crack inherently creates damage to the material by introducing loss of

load carrying area (Xue, 2007). Furthermore, the actual distribution of void nucleation, void size, shape, orientation and spacing have to be treated in a stochastic way since the distribution of such parameters are often unknown;

iii. Due to the large number of material parameters, the calibration of the GTN model is a challenging procedure that still remains open (Bao, 2003). Moreover, those parameters are strongly coupled and it was proven that a non-unique solution can exist if no physical significance is added to these parameters (e.g. ductile fracture initiation can either be simulated as early nucleation of a small volume of voids or delayed nucleation of a large volume of voids (Kiran & Khandelwal, 2014));

iv. The matrix material obeys the classical isotropic von Mises yield criterion and the voids retain their spherical shape. However, in some applications such as in cold rolled metal sheets, the micro-voids that form within a loaded material are ellipsoidal rather than spherical, due to the influence of the asymmetrical loadings and/or an anisotropic microstructure (Stewart, 2009). In coupled damage criteria, *poor plasticity modelling leads to poor damage modelling*. By neglecting the anisotropic behaviour of the material matrix, original Gurson-like criteria are unable to reliably predict the fracture on strongly anisotropic ductile materials;

v. In Gurson's (1977) limit-analysis for the hollow sphere the matrix plastic dissipation was approximated with a function that depended only on the radial coordinate, r, i.e. the polar coordinate, θ was neglected. This approximation amounts to discarding any combined effects of shear and mean stress on the yielding of the porous solid. As a consequence, the original Gurson-type criteria are insensitive to the third-stress invariant, J_3^{Σ} and depend only on the stress triaxiality, T_{Σ} which, as discussed previously, can be insufficient to correctly characterize yielding, even for high triaxiality loadings, see e.g. Alves, Revil-Baudard & Cazacu (2014).

2.3.1. Calibration of the model parameters

The material parameters identification can be performed through: (i) microscopic measurements; (ii) macroscopic measurements; and (iii) a hybrid experimental-numerical approach. The microscopic approach allows the direct evaluation of the initial void volume fraction, f_0 and of the volume fraction of void nucleating particles, f_{N} through image analysis of the undamaged material with 3D X-ray micro-tomography or *in-situ* neutron

diffraction. Additionally, it can be used to quantify the ductile fracture parameters, f_c and f_F. This approach also allows the qualitative measurement of other variables such as, void spacing, size and distribution as well as fracture propagation and final crack aspect. The macroscopic approach uses experimental tests (e.g. tensile tests on various notched specimens to obtain different stress triaxialities, punch tests, butterfly tests, etc.) and Digital Image Correlation (DIC) measurements to determine the load-displacement curves, displacement or strain at the onset of coalescence and at fracture, and the crack appearance on the specimen thought image analysis. The hybrid experimental-numerical approach combines finite element simulations with experimental data to determine the value of the material parameters that lead to the best fittings between the numerical and experimental load-displacement curves. In most investigations, the calibration procedure starts by fixing the void interaction parameters to $q_1 = 1.5$, $q_2 = 1$ and $q_3 = q_1^2$, as recommended by Tvergaard (1982), as well as fixing the standard deviation of the void nucleation strain to $s_N = 0.1$ – a common value in several studies, regardless of the material considered (see Benseddiq & Imad (2008)). The remaining parameters, void nucleation parameters, (f_N, ε_N), for strain-controlled nucleation and the ductile fracture parameters, (f_c, f_F) are calibrated following a mono-parametric analysis, in order to determine the numerical values that yields an overall good agreement with experimental results. Due to the strong coupling between the material parameters, different experiments should be performed to calibrate each set of parameters. It should be noted that each calibration step is not independent from all subsequent steps and therefore a calibration procedure must be repeated iteratively until satisfactory results are achieved (Dunand, 2013).

Besides the GTN model specific parameters, the hardening law of the matrix material has also to be defined for the complete description of the coupled damage model. The hardening law parameters are chosen to fit the stress-strain curve of the actual porous material obtained from quasi-static uniaxial tensile tests of un-notched specimens up to necking. When the initial porosity, f_0 is very small when compared with the nucleated void volume fraction, f_N the tensile behaviour of the porous material remains almost unaffected by the growth of pre-existing voids for strains lower than the nucleation strain, ε_N thus the matrix degradation can be neglected.

One can conclude that the GTN's parameter identification is a challenging issue that has strongly limited the model application in the industry environment. Although there have been a large amount of work aimed at the development of calibration procedures, to the author knowledge there is still no well-stablished method or standard calibration procedure. For more information concerning the GTN model parameters calibration, the reader is referred to the work of Benseddiq & Imad (2008), Xue et al. (2010), Dunand & Mohr (2011), Li et al. (2011) and Kiran & Khandelwal (2014).

2.3.2. Modifications and extensions of Gurson's analysis

In addition to the extensions to the original Gurson (1977) model proposed by Chu & Needleman (1980) to account for void nucleation, and by Tvergaard & Needleman (1984) to account for the loss of load-carrying capacity associated with void coalescence, many other works have modified and extended Gurson's analysis to more complex materials, as well as to more complex void shapes and distributions. The reader is referred to the work of: Gologanu, Leblond & Devaux (1993) to account for ellipsoidal voids (prolate and oblate) rather than spherical voids; the works of Liao, Pan & Tang (1997) and Benzerga & Besson (2001) which address anisotropy using Hill's 1948 yield criterion for transversely isotropic metal sheets under plane stress conditions and for orthotropic porous metals, respectively; and the extended GTN model proposed by Besson & Guillemer-Neel (2003) to include mixed isotropic and kinematic hardening within a thermodynamic framework. Other very relevant extensions were proposed by Xue (2008) and Nahshon & Hutchinson (2008) to introduce a dependency of the damage evolution on the third-stress invariant (i.e. Lode angle dependence), and thus deal with the material deterioration under shear-dominated loads due to void distortion and void sheet coalescence in an heuristic way. Moreover, Cazacu et al. (2013) developed an analytic criterion to include the effect of the third invariant of the deviatoric stress tensor on the yielding of the porous material governed by a von Mises yield criterion. This thesis will particularly study the modifications proposed by Stewart (2009) to account for materials that have different yield strengths in tension *versus* compression, the so-called tension-compression asymmetry.

3. Analytic Yield Criteria for Porous Solids Exhibiting Tension–Compression Asymmetry

It is well established that metallic sheets usually exhibit plastic anisotropy as a result of the forming processes. The importance of the plastic anisotropy has been recognized and there has been a global effort to model its effects on the mechanical behaviour of the materials, through the development of macroscopic plasticity models. However, until recent years the strength differential (SD) effects have been neglected (Barros, Alves, Oliveira, & Menezes, 2016). The SD effects, or tension-compression asymmetry is a shear related phenomenon that results from single crystal plastic deformation, either due to the activation of mechanical twinning or due to slip that does not obey the well-known Schmid law, i.e. non-Schmid type slip (Hosford & Allen, 1973). Unlike the conventional (Schmid type) slip deformation which is a reversible shear mechanism, twinning is an irreversible and directional shear mechanism, i.e. shear can promote twinning in one direction but not in the opposite direction. The twinning effect becomes more prominent when increasing the strain rate (Barros et al., 2016; Stewart, 2009).

The SD effects are more pronounced in metals with hexagonal closed packed (HCP) structure (e.g. α-titanium, magnesium, zirconium, etc.). However, materials with cubic crystal structure such as high strength steels (HSS), molybdenum and aluminium alloys can also exhibit some tension–compression asymmetry in yielding, although in the absence of voids they are pressure-insensitive (Benzerga, Besson, & Pineau, 2004b; Stewart, 2009).

A fundamental issue that arises is how the SD effects of the matrix material impacts the damage accumulation, i.e. the void growth stage of the ductile failure mechanism; and, as a consequence, the overall ductility of the voided metallic polycrystals. To account for the SD effects in a incompressible matrix, Stewart & Cazacu (2011) recently developed a macroscopic anisotropic yield criterion for porous aggregates that is sensitive to all stress invariants. For this purpose, in their analysis, the matrix plastic behaviour was described by the Cazacu, Plunkett & Barlat (2006) orthotropic yield criterion – often referred as the CPB06 yield criterion, which will be preliminary presented in the next subsection. Following it, the Stewart & Cazacu's (2011) analytic plastic potential for random distribution of spherical voids is presented and its main features and properties are briefly discussed.

3.1. Cazacu, Plunkett and Barlat yield criterion

In order to account for both the anisotropy and the SD effects in pressure insensitive materials, Cazacu, Plunkett & Barlat (2006) proposed the following macroscopic elastoplastic yield criterion, φ:

$$\varphi\left(\hat{\boldsymbol{\Sigma}}, k, a, \sigma_1^{\mathrm{T}}\right) = \tilde{\Sigma}_{\mathrm{e}} - \sigma_1^{\mathrm{T}} = 0, \tag{3.1}$$

where $\tilde{\Sigma}_{\mathrm{e}}$ denotes the CPB06 macroscopic equivalent stress, such that:

$$\tilde{\Sigma}_{\mathrm{e}} = \hat{m}\left[\sum_{i=1}^{3}\left(\left|\hat{\Sigma}_i\right| - k\hat{\Sigma}_i\right)^a\right]^{\frac{1}{a}}, \tag{3.2}$$

and σ_1^{T} is the uniaxial tensile yield stress along an axis of orthotropy of the matrix material, say the rolling direction, which is denoted by the 1-direction. In the previous expression, k is a material parameter that captures the SD effects and the parameter a is the degree of homogeneity, a positive integer usually taken as $a = 2$. The orthotropy is introduced through a linear transformation on the deviatoric component of the Cauchy stress tensor, $\boldsymbol{\Sigma}'$ i.e.:

$$\hat{\boldsymbol{\Sigma}} = \mathbf{C} : \boldsymbol{\Sigma}', \tag{3.3}$$

where $\mathbf{C}$ is a fourth-order symmetric tensor describing the anisotropy of the matrix. Note that the hat accent is used to denote all quantities defined in the equivalent isotropic stress space. In the previous expression, $\hat{\Sigma}_i$ are the principal values of the transformed stress tensor, $\hat{\boldsymbol{\Sigma}}$ (see Annex A for details regarding the calculation of $\hat{\Sigma}_i$). Let $(\mathbf{e}_1, \mathbf{e}_2, \mathbf{e}_3)$ be the reference frame associated with the orthotropy axes, such that $\mathbf{e}_1$, $\mathbf{e}_2$ and $\mathbf{e}_3$ are the rolling, transverse and through-thickness directions, respectively. In that case, the fourth-order tensor $\mathbf{C}$ involves 9 independent anisotropy coefficients and can be represented at the orthotropy axes, using the Voigt notation, by:

$$\mathbf{C} = \begin{bmatrix} C_{11} & C_{12} & C_{13} & 0 & 0 & 0 \\ C_{12} & C_{22} & C_{23} & 0 & 0 & 0 \\ C_{13} & C_{23} & C_{33} & 0 & 0 & 0 \\ 0 & 0 & 0 & C_{44} & 0 & 0 \\ 0 & 0 & 0 & 0 & C_{55} & 0 \\ 0 & 0 & 0 & 0 & 0 & C_{66} \end{bmatrix}, \tag{3.4}$$

Finally, the effective stress constant, $\hat{m}$ is defined such that $\tilde{\Sigma}_{\mathrm{e}}$ reduces to the tensile yield stress along an axis of orthotropy by:

$$\hat{m} = \left[\frac{1}{\sum_{i=1}^{3} \left(|\phi_i| - k\phi_i \right)^a} \right]^{\frac{1}{a}}, \tag{3.5}$$

where

$$\begin{Bmatrix} \phi_1 \\ \phi_2 \\ \phi_3 \end{Bmatrix} = \begin{Bmatrix} (2/3)C_{11} - (1/3)C_{12} - (1/3)C_{13} \\ (2/3)C_{12} - (1/3)C_{22} - (1/3)C_{23} \\ (2/3)C_{13} - (1/3)C_{23} - (1/3)C_{33} \end{Bmatrix}. \tag{3.6}$$

The anisotropic material parameters identification can be performed based on results of tensile and compressive tests, (e.g. uniaxial tension tests on flat specimens and uniaxial compression tests on cylindrical specimens). For more information on the identification procedure the reader is referred to methods presented by Cazacu, Plunkett & Barlat (2006), Barros et al. (2016) and Revil-Baudard et al. (2016).

For an isotropic material, the tensor **C** reduces to the fourth-order identity tensor, **I** and the CPB06 yield criterion reduces to its isotropic form, such that:

$$\varphi\left(\boldsymbol{\Sigma}', k, a, \sigma_{\mathrm{T}}\right) = \tilde{\Sigma}_{\mathrm{e}} - \sigma_{\mathrm{T}} = 0, \tag{3.7}$$

with σ_{T} defined as the matrix uniaxial yield stress in tension (equal in all directions). The isotropic form of the macroscopic equivalent stress, $\tilde{\Sigma}_{\mathrm{e}}$ is given by:

$$\tilde{\Sigma}_{\mathrm{e}} = m\left[\sum_{i=1}^{3} \left(\left|\Sigma_i'\right| - k\Sigma_i' \right)^a \right]^{\frac{1}{a}}, \tag{3.8}$$

where Σ_i' are the principal values of the Cauchy stress deviatoric component and *m*, is the isotropic version of the effective stress constant given, for $a = 2,$ by:

$$m = \sqrt{\frac{9}{2\left(3k^2 - 2k + 3\right)}}. \tag{3.9}$$

In these conditions, it can be easily shown that, for the isotropic case, the material constant *k* alone allows for the description of the SD effect and can be expressed in terms of the ratio between the uniaxial yield in tension, σ_{T} and the uniaxial yield in compression, σ_{C} as:

$$k = \frac{1 - r\left(\sigma_{\mathrm{T}}, \sigma_{\mathrm{C}}\right)}{1 + r\left(\sigma_{\mathrm{T}}, \sigma_{\mathrm{C}}\right)}, \tag{3.10}$$

where the function *r* is given by:

$$r\left(\sigma_{\mathrm{T}}, \sigma_{\mathrm{C}}\right) = \sqrt{\left(2 - \left(\frac{\sigma_{\mathrm{T}}}{\sigma_{\mathrm{C}}}\right)^2\right) \Big/ \left(2\left(\frac{\sigma_{\mathrm{T}}}{\sigma_{\mathrm{C}}}\right)^2 - 1\right)}. \tag{3.11}$$

Notice that if there is no difference between the response in tension and compression, i.e. no tension-compression asymmetry ($\sigma_T = \sigma_C$), then $k = 0$, $m = \sqrt{3/2}$ and $\tilde{\Sigma}_e$ simply becomes the von Mises equivalent stress, $\Sigma_e = \sqrt{3J_2^{\Sigma}}$. For anisotropic materials exhibiting SD effects it is not possible to define a single σ_T/σ_C ratio and, as a consequence, the physical meaning of the parameter *k* is lost (Barros et al., 2016). Moreover, the convexity of the isotropic form of the yield criterion is guaranteed for any integer $a \geq 2$ and for $k \in [-1, 1]$ (Cazacu et al., 2006).

The main characteristics of the CPB06 yield criterion that justify its selection for representing the plastic behaviour of the matrix material of the porous aggregate are the following (Alves, Oliveira, Menezes, & Cazacu, 2017):

i. Although it is pressure-insensitive, i.e. neglects the effects of the first stress invariant, I_1^{Σ}, it accounts for the SD effects, a phenomenon that occurs in HSS (and AHSS), the same family of materials that sparked growing interest in developing reliable damage models;

ii. If a material displays SD effects $(k \neq 0)$, the plastic flow depends on the sign and ordering of all principal values of the macroscopic stress deviator, $\boldsymbol{\Sigma}'$ hence it depends on the third-invariant of the deviatoric stress tensor, J_3^{Σ}, which, as discussed, can have a great impact on damage accumulation and ductile fracture;

iii. In the isotropic case all the yield criterion parameters, $\varphi(\boldsymbol{\Sigma}', k, a, \sigma_T) = 0$ have a clear physical meaning, namely the uniaxial yield stress in tension, σ_T and the material parameter *k,* which is intimately related to specific single-crystal plastic deformation mechanisms;

iv. The ability of the CPB06 criterion to easily reduce to other yield criteria when no SD effects are considered $(k \neq 0)$, e.g. the Hill'48 criterion if $a = 2$ and **C** is constrained to be deviatoric; and the von Mises criterion if $a = 2$ and **C**=**I**.

To further emphasise the dependency on the third-invariant of deviatoric stress tensor, J_3^{Σ} of the CPB06 yield criterion (i.e. the Lode angle dependence), Figure 3.1 (a) illustrates the deviatoric π-plane representations of some isotropic yield surfaces, corresponding to materials displaying different tension–compression asymmetries:

- $k = 0 \;\; (\sigma_T/\sigma_C = 1)$, which corresponds to a von Mises material;
- $k = 0.3098 \;\; (\sigma_T/\sigma_C = 1.21)$, corresponding to a fully-dense isotropic BCC material;
- $k = -0.3098 \; (\sigma_T/\sigma_C = 0.83)$, corresponding to a fully-dense isotropic FCC material.

Both cubic structures are considered to deform at single-crystal level only by deformation twinning, in agreement with Hosford & Allen (1973). Figure 3.1 (a) displays the drastic departure of the yield locus from the von Mises circle to triangular shaped surfaces with rounded corners, when $k \neq 0$. The dependence of the yield loci on J_3^{Σ} is evidenced by this change of shape. In fact, in the π-plane representations the radial coordinate is related to the second invariant of the stress deviator, J_2^{Σ} while the angular coordinate is related to the third invariant, J_3^{Σ} (see Figure 2.2). In other words, a yield criterion is J_3^{Σ} dependent if there is a change of the radial coordinate with the angular coordinate, i.e. the yield locus is not a circle (e.g. the Tresca criterion). Figure 3.1 (b) presents the same surfaces but assuming plane stress conditions, highlighting the departure of the yield locus from the von Mises ellipse to triangular shaped surfaces with rounded corners.

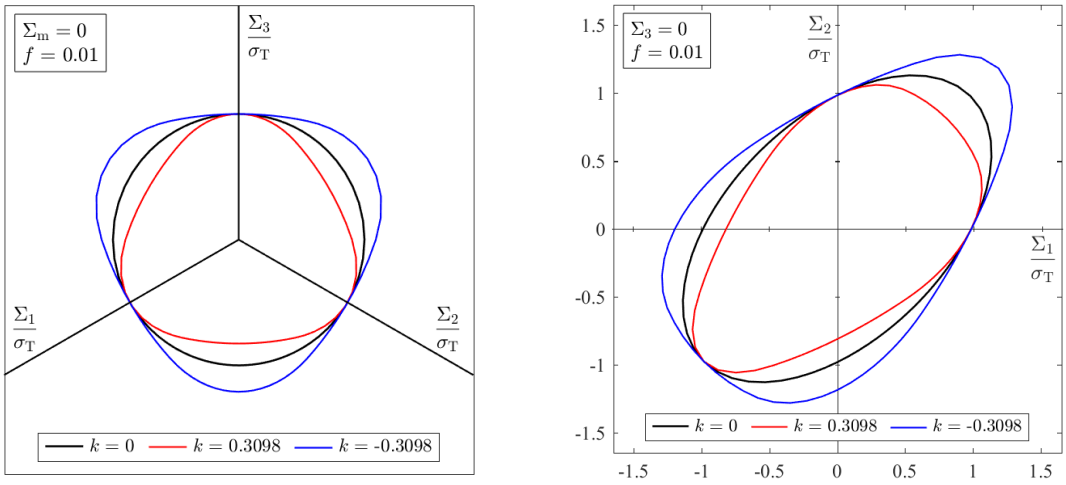

Figure 3.1. Dependency on the third-invariant of the stress deviator due to SD effects: (a) π-plane representation; (b) plane stress representation.

3.2. An yield criterion for anisotropic porous aggregates containing spherical voids and exhibiting SD effects

As mentioned in the previous chapters, much work has been done to extend the original Gurson (1977) damage model to include the anisotropy effects of the matrix. It is worth noting the contribution of: Liao, Pan & Tang (1997) that modified Gurson's (1977) cylindrical void criterion to account for transverse isotropy using the Hill'48 yield criterion; the contribution of Benzerga & Besson (2001), which extended Gurson's (1977) spherical criterion for orthotropic materials also using the Hill'48 criterion; and the work of Gologanu, Leblond & Devaux (1993) that developed an macroscopic yield criterion for prolate ellipsoidal voids to account for void shape effects, which later was further extended by Benzerga, Jacques Besson & Pineau (2004) to merge Gologanu et al. (1993) elliptical void shape model with the orthotropy modelling earlier proposed in Benzerga & Besson (2001). Although these studies account for the anisotropy effect, they all neglect (or fail to recognize) the tension-compression asymmetry behaviour in yielding that some materials can display.

In order to account for the SD effects on yielding of porous media, Stewart & Cazacu (2011) recently performed a rigorous mathematical upscaling analysis, based on the kinematic non-linear homogenization approach of Hill (1967) and Mandel (1972), to derive a closed-form macroscopic yield criterion for anisotropic porous aggregates containing randomly distributed spherical voids (Lebensohn & Cazacu, 2012; Revil-Baudard et al., 2016). The tension–compression asymmetry associated with directional shear mechanisms at the single crystal level are accounted by the CPB06 anisotropic yield criterion. The plastic potential derived by Stewart & Cazacu (2011), including Tvergaard (1981) additional fitting parameters, q_i (see Equation (2.23)), has the following expression:

$$\varphi\left(\hat{\boldsymbol{\Sigma}}, k, \sigma_1^{\mathrm{T}}, f\right) = \left(\frac{\tilde{\Sigma}_{\mathrm{e}}}{\sigma_1^{\mathrm{T}}}\right)^2 + 2q_1 f \cosh\left(\frac{3q_2\Sigma_{\mathrm{m}}}{h\sigma_1^{\mathrm{T}}}\right) - q_3 f^2 - 1 = 0, \tag{3.12}$$

where $\tilde{\Sigma}_{\mathrm{e}}$ is the macroscopic equivalent stress associated with the CPB06 anisotropic criterion with $a = 2$, k is the CPB06's material parameter describing the SD effects, σ_1^{T} is the uniaxial yield strength along an axis of orthotropy of the matrix material (e.g. rolling direction), and f is the void volume fraction (or *effective* void volume fraction, f^* if assuming Tvergaard & Needleman's (1984) extension (see Equation (2.25)). In the previous expression, h is the so-called anisotropy hydrostatic factor, which controls the damage

evolution and is applied to the hydrostatic part of the macroscopic yield criterion. This factor depends on the sign of the macroscopic mean stress, Σ_m and on the anisotropy coefficients of the fourth-order tensor **C** (see Equation (3.4)) and can be expressed, following Lebensohn & Cazacu (2012), as:

$$h = \sqrt{\frac{\hat{n}}{5}\left(4t_1 + 6t_2\right)}, \tag{3.13}$$

where the constant $\hat{n}$ accounts for the matrix SD effects and is expressed as:

$$\hat{n} = \begin{cases} \dfrac{1}{\hat{m}^2}\left(\dfrac{3}{3k^2 - 2k + 3}\right) & \text{if } \Sigma_m < 0, \\ \dfrac{1}{\hat{m}^2}\left(\dfrac{3}{3k^2 + 2k + 3}\right) & \text{if } \Sigma_m \geq 0, \end{cases} \tag{3.14}$$

for $a = 2,$ with $\hat{m}$ being the effective stress constant given by Equation (3.5). The scalars t_1 and t_2 of Equation (3.13) account for the matrix anisotropy and are defined as:

$$t_1 = 3\left(B_{13}B_{23} + B_{12}B_{23} + B_{12}B_{13} + 2{B_{12}}^2 + 2{B_{13}}^2 + 2{B_{23}}^2\right); \tag{3.15}$$

$$t_2 = {B_{44}}^2 + {B_{55}}^2 + {B_{66}}^2, \tag{3.16}$$

where B_{ij}, with $i, j = 1,...,6$, are the components of tensor **B**, defined as the inverse of **L**, such that $\mathbf{B} = \mathbf{L}^{-1} = \left(\mathbf{C} : \mathbf{T}\right)^{-1}$, where **T** denotes the fourth-order deviatoric unit tensor, i.e.:

$$\mathbf{T} = \begin{bmatrix} 2/3 & -1/3 & -1/3 & 0 & 0 & 0 \\ -1/3 & 2/3 & -1/3 & 0 & 0 & 0 \\ -1/3 & -1/3 & 2/3 & 0 & 0 & 0 \\ 0 & 0 & 0 & 1 & 0 & 0 \\ 0 & 0 & 0 & 0 & 1 & 0 \\ 0 & 0 & 0 & 0 & 0 & 1 \end{bmatrix}. \tag{3.17}$$

Note that the Voigt notation is adopted in all these definitions. The expressions of the components of **B** in terms of the linear transformed anisotropy coefficients L_{ij}, with $i, j = 1,...,6$, are resumed in Annex B.

Since the yield surface proposed by Stewart & Cazacu (2011) depends on all stress invariants, the criterion accounts for the influence of both the direction and the sense of loading on the dilatational plastic response of the material (Lebensohn & Cazacu, 2012). In addition to yielding of the porous aggregate, the combined effects of matrix anisotropy and tension–compression asymmetry are also accounted on the porosity evolution. In fact, as stated in Equation (2.19), the porosity evolution due to void growth, $\dot{f}_{\text{growth}}$ is obtained from the mass conservation principle. Taking into account the definition of the plastic strain rate

tensor (see Equation (2.15)) and the yield function (see Equation (3.12)), the void growth is defined as:

$$\dot{f}_{\text{growth}} = (1-f) D_{kk}^{\text{p}} = (1-f)\dot{\lambda}\frac{\partial \varphi}{\partial \Sigma_{kk}} = (1-f)\dot{\lambda}\left(\frac{6q_1q_2f}{h\sigma_1^{\text{T}}}\right)\sinh\left(\frac{3q_2\Sigma_{\text{m}}}{h\sigma_1^{\text{T}}}\right), \tag{3.18}$$

where D_{kk}^{p} is the trace of the macroscopic plastic strain rate tensor, $\mathbf{D}^{\text{p}}$, and $\dot{\lambda} \geq 0$ is the rate of the plastic multiplier. In the previous expression it is clearly seen that the porosity evolution depends on the parameter *h* which, by its turn, depends on the strength–differential parameter *k* and on the anisotropy coefficients.

Contrary to the original Gurson-type criteria, the yield function is no longer symmetric with respect to the transformations $(\Sigma_{\text{m}}, \boldsymbol{\Sigma}') \rightarrow (\Sigma_{\text{m}}, -\boldsymbol{\Sigma}')$ and $(\Sigma_{\text{m}}, \boldsymbol{\Sigma}') \rightarrow (-\Sigma_{\text{m}}, \boldsymbol{\Sigma}')$. Indeed, due to the dependence of the parameter *h* with the sign of the applied mean stress, Σ_{m}, the yield locus given by Equation (3.12) no longer display the centro-symmetry properties previously seen in the Gurson (1977) criteria and on the one presented by Benzerga & Besson (2001). In other words, if the matrix exhibits SD effects the yield surface is not symmetric with respect to the plane $\Sigma_{\text{m}} = 0$. According to Stewart & Cazacu's (2011) criterion, for tensile hydrostatic loading, yielding of the porous material occurs when $\Sigma_{\text{m}} = \hat{p}_{\text{Y}}^{+}$ with:

$$\hat{p}_{\text{Y}}^{+} = \frac{1}{3q_2}\sigma_1^{\text{T}} h^{+} \cosh^{-1}\left(\frac{q_3 f^2 + 1}{2q_1 f}\right), \tag{3.19}$$

whereas, for compressive hydrostatic loading, yielding occurs when $\Sigma_{\text{m}} = \hat{p}_{\text{Y}}^{-}$ with:

$$\hat{p}_{\text{Y}}^{-} = -\frac{1}{3q_2}\sigma_1^{\text{T}} h^{-} \cosh^{-1}\left(\frac{q_3 f^2 + 1}{2q_1 f}\right). \tag{3.20}$$

Note that, as shown in Equations (3.13) and (3.14), *h* can be defined by branches, such as:

$$h = \begin{cases} h^{-} & \text{if } \Sigma_{\text{m}} < 0, \\ h^{+} & \text{if } \Sigma_{\text{m}} \geq 0. \end{cases} \tag{3.21}$$

If $q_3 = q_1^{\,2}$, as Tvergaard (1981) recommended, the previous expressions resume to:

$$\hat{p}_{\text{Y}}^{+} = -\frac{1}{3q_2}\sigma_1^{\text{T}} h^{+} \ln\left(q_1 f\right), \tag{3.22}$$

$$\hat{p}_{\text{Y}}^{-} = +\frac{1}{3q_2}\sigma_1^{\text{T}} h^{-} \ln\left(q_1 f\right). \tag{3.23}$$

As discussed previously, if the matrix is isotropic but displays SD effects $(k \neq 0)$, the anisotropy tensor **C** reduces to the fourth-order identity tensor, **I** and the CPB06 yield criterion takes its isotropic form, i.e. the matrix uniaxial yield stress in tension, σ_T is equal in all directions and there is a single σ_T/σ_C ratio. Thus, Stewart & Cazacu's (2011) anisotropic yield criterion (Equation (3.12)) reduces to its *isotropic* form – the Cazacu & Stewart's (2009) criterion, given as:

$$\varphi\left(\boldsymbol{\Sigma}^{'},k,\sigma_T,f\right)=\left(\frac{\tilde{\Sigma}_e}{\sigma_T}\right)^2+2q_1 f\cosh\left(z_s\frac{3q_2\Sigma_m}{2\sigma_T}\right)-q_3 f^2-1=0, \tag{3.24}$$

where $\tilde{\Sigma}_e$ is the CPB06 isotropic form of the macroscopic equivalent stress. The parameter z_s controls the damage evolution, in the same spirit as the anisotropic parameter *h* in Equation (3.12), but it depends only on the strength-differential parameter *k*, such that:

$$z_s=\frac{2}{h\big|_{isot}}=\begin{cases}1 & \text{if } \Sigma_m<0;\\ \left(\dfrac{\sigma_T}{\sigma_C}\right)=\sqrt{\dfrac{3k^2+2k+3}{3k^2-2k+3}} & \text{if } \Sigma_m\geq 0,\end{cases} \tag{3.25}$$

where $h\big|_{isot}$ is the isotropic form of *h*. Again, because Cazacu & Stewart's (2009) yield criterion depends on all principal values of the deviatoric stress tensor and on the sign of the applied mean stress through the parameter z_s, it does not have the symmetry properties of the Gurson's (1977) criterion. In the isotropic case yielding occurs at purely hydrostatic tensile loading when $\Sigma_m=\hat{p}_Y^+$ for:

$$p_Y^+=-\frac{1}{3q_2}\sigma_T h^+\ln\left(q_1 f\right)=-\frac{2}{3q_2}\sigma_C\ln\left(q_1 f\right), \tag{3.26}$$

whereas, for compressive hydrostatic loading, the model predicts that yielding occurs when $\Sigma_m=\hat{p}_Y^-$ for:

$$p_Y^-=\frac{1}{3q_2}\sigma_T h^-\ln\left(q_1 f\right)=\frac{2}{3q_2}\sigma_T\ln\left(q_1 f\right). \tag{3.27}$$

Note that, according to the two previous expressions, yielding at tensile hydrostatic loading is exclusively a function of the yield strength in compression, σ_C and, in opposition, yielding at compressive hydrostatic loading is a function of the yield strength in tension, σ_T. This counter-intuitive result is related to the exact (analytical) solution for a hollow sphere loaded hydrostatically and obeying the CPB06 isotropic yield criterion (e.g. see Cazacu & Stewart (2009)) and it was further validated by unit cell calculations (Yoon, et al., 2011).

If the matrix material presents no tension–compression asymmetry, i.e. $(\sigma_T = \sigma_C)$, then $k = 0$, thus $z_s = 1$, $m = \sqrt{3/2}$ and the Cazacu & Stewart's (2009) criterion (Equation (3.24)) reduces to the GTN yield criterion. Furthermore, when the material is void-free $(f = 0)$ Stewart & Cazacu (2011) criterion $\varphi(\hat{\boldsymbol{\Sigma}}, k, \sigma_1^T, f)$ given by Equation (3.12), reduces to that of the matrix, i.e. the quadratic form of the CPB06 orthotropic criterion: $\tilde{\Sigma}_e = \sigma_1^T$ if there is tension-compression asymmetry in the matrix and to Hill'48 yield criterion when no strength differential is exhibited.

The validity of the presented anisotropic and isotropic criteria were assessed through comparisons with finite element unit cell calculations. It was concluded that the theoretical yield loci predictions provided by both the isotropic and anisotropic criteria for the void-matrix aggregate shown an overall good agreement with the numerical results. For more details on micromechanical finite-element analyses of unit cells and on the validation of the Stewart & Cazacu (2011) yield surfaces the reader is referred to the work of Stewart (2009) and Lebensohn & Cazacu (2012).

3.3. CPB06 porous model under macroscopic axisymmetric stress states

In order to further investigate the effects of the third-invariant, J_3^{Σ}, and of the stress triaxiality, T_{Σ} on yielding of the porous aggregate and, ultimately, on the damage accumulation, this thesis will focus particularly on the study of macroscopic axisymmetric loadings. Thus, in an introductory way, this section briefly presents the expressions that characterize this type of stress state. Letting $(\mathbf{e}_1, \mathbf{e}_2, \mathbf{e}_3)$ be the reference frame associated with the axes of orthotropy, an axisymmetric loading about the $\mathbf{e}_3$ axis is characterized such that $\Sigma_{11} = \Sigma_{22}$, i.e. only two principal macroscopic stresses are independent:

$$\boldsymbol{\Sigma} = \Sigma_{11}\left(\mathbf{e}_1 \otimes \mathbf{e}_1 + \mathbf{e}_2 \otimes \mathbf{e}_2\right) + \Sigma_{33}\left(\mathbf{e}_3 \otimes \mathbf{e}_3\right), \tag{3.28}$$

with $\boldsymbol{\Sigma}$ denoting the macroscopic stress tensor, Σ_{11} the imposed macroscopic lateral stress and Σ_{33} the macroscopic axial stress. For such loadings the mean stress, Σ_m becomes:

$$\Sigma_m = \frac{2\Sigma_{11} + \Sigma_{33}}{3}, \tag{3.29}$$

the von Mises equivalent stress, Σ_e is given by:

$$\Sigma_e = \sqrt{3J_2^\Sigma} = \left|\Sigma_{11} - \Sigma_{33}\right|, \tag{3.30}$$

and the third deviatoric stress invariant, J_3^Σ is written as:

$$J_3^\Sigma = \Sigma_1^{'}\Sigma_2^{'}\Sigma_3^{'} = -\frac{2}{27}\left(\Sigma_{11} - \Sigma_{33}\right)^3. \tag{3.31}$$

In this conditions, the macroscopic stress triaxiality, T_Σ is defined by:

$$T_\Sigma = \frac{\Sigma_m}{\Sigma_e} = \frac{2\Sigma_{11} + \Sigma_{33}}{3\left|\Sigma_{11} - \Sigma_{33}\right|}. \tag{3.32}$$

Due to the presence of an absolute value in the denominator, one can conclude that for the same stress triaxiality, T_Σ there are two possible orderings of the lateral and axial stress components, i.e. there are two possible axisymmetric stress states that yield the same stress triaxiality. These stress states can be distinguish by the sign of J_3^Σ (see Equation (3.31)), or analogously, by the two possible values of the Lode angle parameter, $\overline{\theta}_\Sigma = \pm 1$. Defining ρ as a prescribed constant to ensure a specified value for the stress triaxiality ratio, such that:

$$\rho = \frac{\Sigma_{33}}{\Sigma_{11}}, \tag{3.33}$$

the two possible axisymmetric stress states can be distinguished as:

i. $\Sigma_{33} > \Sigma_{11} \Leftrightarrow \rho > 1,$ which corresponds to $J_3^\Sigma > 0$ and $\overline{\theta}_\Sigma = 1$;

ii. $\Sigma_{33} < \Sigma_{11} \Leftrightarrow \rho < 1,$ which corresponds to $J_3^\Sigma < 0$ and $\overline{\theta}_\Sigma = 1.$

It can be shown that for loadings characterized by $\Sigma_{33} > \Sigma_{11},$ two principal values of the deviator stress tensor $\boldsymbol{\Sigma}'$ are *compressive* (negative) but the maximum principal value is *tensile* (positive). In opposition, if $\Sigma_{33} < \Sigma_{11}$ then two principal values of the deviator stress tensor $\boldsymbol{\Sigma}'$ are *tensile* (positive) but the minor principal value is *compressive* (negative) and has the largest absolute value (Alves et al., 2014). The two ρ values that originate the same specified stress triaxiality, T_Σ are given by:

$$\rho = \begin{cases} \dfrac{3T_\Sigma + 2}{3T_\Sigma - 1} & \text{if } J_3^\Sigma > 0, \\ \dfrac{3T_\Sigma - 2}{3T_\Sigma + 1} & \text{if } J_3^\Sigma < 0. \end{cases} \tag{3.34}$$

The proof of this result, as well as other details regarding the study of axisymmetric stress states (e.g. determination of the Lode angle parameters) can be found in Appendix A.

It is possible to prove that, under axisymmetric loadings, the equivalent stress according to the CPB06 anisotropic criterion, $\tilde{\Sigma}_e$ given in Equation (3.2), can be related to the von Mises equivalent stress given previously in Equation (3.30) by the relation:

$$\tilde{\Sigma}_e = \frac{1}{\hat{g}}\Sigma_e = \frac{1}{\hat{g}}\left|\Sigma_{11} - \Sigma_{33}\right|, \tag{3.35}$$

with $\hat{g}$ being a constant that depends on the sign of J_3^{Σ} given by:

$$\hat{g} = \begin{cases} \dfrac{1}{\hat{m}\left|\phi_3\right|\sqrt{2\left(3k^2 - 2k + 3\right)}} & \text{if } J_3^{\Sigma} > 0; \\ \dfrac{1}{\hat{m}\left|\phi_3\right|\sqrt{2\left(3k^2 + 2k + 3\right)}} & \text{if } J_3^{\Sigma} < 0, \end{cases} \tag{3.36}$$

where $\hat{m}$ is the anisotropic form of the effective stress constant, given in Equation (3.5), and $\left|\phi_3\right|$ is the absolute value of the third component of the anisotropic constants vector, given in Equation (3.6). Knowing the relationship between the von Mises and the CPB06 equivalent stresses, it is possible to quantify the effect of the sign of J_3^{Σ} for purely deviatoric loadings $(\Sigma_m = 0)$. Indeed, substituting Equation (3.35) in the Stewart & Cazacu (2011) criterion (Equation (3.12)), the porous anisotropic material is predicted to yield at purely deviatoric loading when:

$$\frac{\Sigma_e}{\sigma_1^T} = \begin{cases} \dfrac{\left(1 - q_1 f\right)}{\hat{m}\left|\phi_3\right|\sqrt{2\left(3k^2 - 2k + 3\right)}} & \text{if } J_3^{\Sigma} > 0; \\ \dfrac{\left(1 - q_1 f\right)}{\hat{m}\left|\phi_3\right|\sqrt{2\left(3k^2 + 2k + 3\right)}} & \text{if } J_3^{\Sigma} < 0, \end{cases} \tag{3.37}$$

if $q_3 = {q_1}^2$, as recommended in Tvergaard (1981). In order to better understand this result, the same expressions are now expressed under isotropic conditions. In the isotropic case, the effective stress constant $\hat{m}$ takes its isotropic form, m (Equation (3.9)) and the anisotropy tensor **C** reduces to the fourth-order identity tensor, **I**. Therefore, $\left|\phi_3\right|_{isot} = 1/3$ and the constant $\hat{g}$ resumes to its isotropic version, g such that:

$$g = \begin{cases} 1 & \text{if } J_3^{\Sigma} > 0; \\ \left(\dfrac{\sigma_C}{\sigma_T}\right) = \sqrt{\dfrac{3k^2 - 2k + 3}{3k^2 + 2k + 3}} & \text{if } J_3^{\Sigma} < 0, \end{cases} \tag{3.38}$$

where σ_T is the uniaxial yield in tension and σ_C the uniaxial yield in compression. Hence, Equation (3.35) can be rewritten as:

$$\tilde{\Sigma}_e = \begin{cases} \Sigma_e & \text{if } J_3^\Sigma > 0; \\ \left(\dfrac{\sigma_T}{\sigma_C}\right)\Sigma_e & \text{if } J_3^\Sigma < 0. \end{cases} \tag{3.39}$$

Substituting the previous expression in the Cazacu and Stewart's (2009) criterion (Equation (3.24)), the porous material yield at purely deviatoric loading $(\Sigma_m = 0)$ when:

$$\frac{\Sigma_e}{\sigma_T} = \begin{cases} (1 - q_1 f) & \text{if } J_3^\Sigma > 0; \\ \left(\dfrac{\sigma_C}{\sigma_T}\right)(1 - q_1 f) & \text{if } J_3^\Sigma < 0, \end{cases} \tag{3.40}$$

where, again, it is assumed that $q_3 = q_1^2$. Note the clear effect of the tension-compression asymmetry on yielding of the porous material and its dependence on the sign of the third invariant of the deviatoric stress tensor, J_3^Σ (or the Lode parameter). In order to better understand the impact of the SD effect on both purely deviatoric loadings $(\Sigma_m = 0)$ and purely hydrostatic loadings $(\Sigma_e = 0)$, Figure 3.2 presents a projection of the Cazacu & Stewart's (2009) analytical yield locus in the plane (Σ_m, Σ_e), for an isotropic material with yield strength in tension less than in compression $(k = -0.3098)$ under axisymmetric loading conditions. It can be verified that the SD effects, (in the form of σ_C/σ_T), are manifested only for deviatoric loadings with $J_3^\Sigma < 0$ and for tensile hydrostatic loadings.

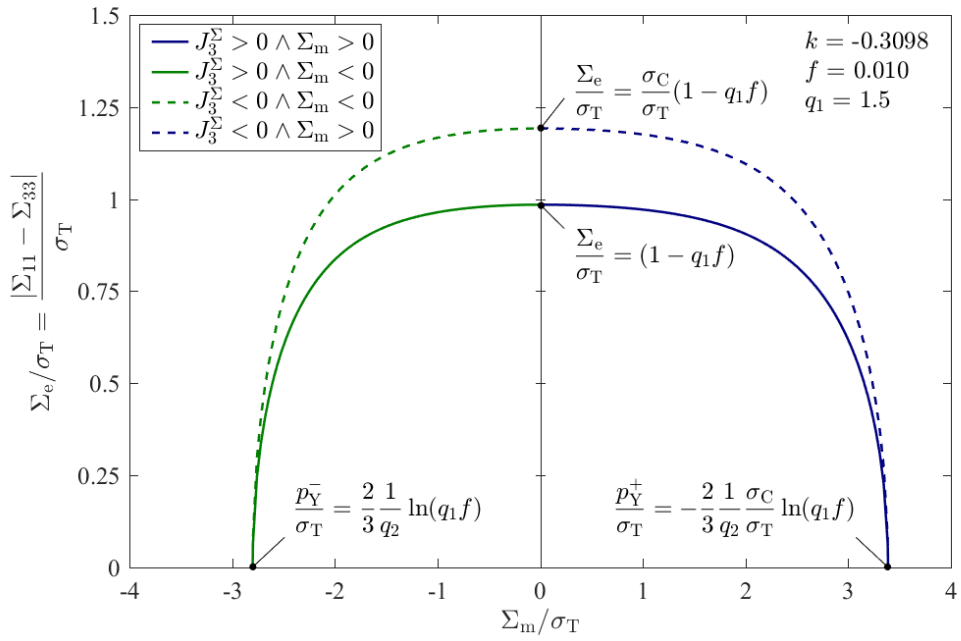

Figure 3.2. Projection of the Cazacu and Stewart's (2009) isotropic yield loci for a matrix material exhibiting SD effects ($k = -0.3098$) under an axisymmetric stress state.

According to the previous relationships, Cazacu & Stewart's (2009) single expression given in Equation (3.24) can be defined by branches, distinguished by the sign of J_3^{Σ} and the sign of Σ_m. Thus, under axisymmetric stress states, for $J_3^{\Sigma} < 0$ (i.e. $\Sigma_{33} < \Sigma_{11}$) results:

$$\varphi = \begin{cases} \left(\frac{\sigma_T}{\sigma_C}\right)^2 \left(\frac{\Sigma_e}{\sigma_T}\right)^2 + 2q_1 f \cosh\left(\left(\frac{\sigma_T}{\sigma_C}\right)\frac{3q_2\Sigma_m}{2\sigma_T}\right) - q_3 f^2 - 1 = 0 & \text{if } \Sigma_m > 0; \\ \left(\frac{\sigma_T}{\sigma_C}\right)^2 \left(\frac{\Sigma_e}{\sigma_T}\right)^2 + 2q_1 f \cosh\left(\frac{3q_2\Sigma_m}{2\sigma_T}\right) - q_3 f^2 - 1 = 0 & \text{if } \Sigma_m < 0, \end{cases} \tag{3.41}$$

whereas for $J_3^{\Sigma} > 0$ (i.e. $\Sigma_{33} > \Sigma_{11}$) results:

$$\varphi = \begin{cases} \left(\frac{\Sigma_e}{\sigma_T}\right)^2 + 2q_1 f \cosh\left(\left(\frac{\sigma_T}{\sigma_C}\right)\frac{3q_2\Sigma_m}{2\sigma_T}\right) - q_3 f^2 - 1 = 0 & \text{if } \Sigma_m > 0; \\ \left(\frac{\Sigma_e}{\sigma_T}\right)^2 + 2q_1 f \cosh\left(\frac{3q_2\Sigma_m}{2\sigma_T}\right) - q_3 f^2 - 1 = 0 & \text{if } \Sigma_m < 0. \end{cases} \tag{3.42}$$

The previous expressions define the yield loci of each of the four curves in the (Σ_m, Σ_e) stress space, illustrated in Figure 3.2. In the next chapter a sensibility analysis will be performed to the axisymmetric yield loci and a sounder discussion on the effect of the model parameters will be conducted.

4. Sensitivity Analysis of the CPB06 Porous Model Yield Surfaces

In this chapter a sensitivity analysis of the Cazacu & Stewart's (2009) isotropic model parameters, from now on referred as the CPB06 porous model, is performed. To this end, the yield loci change of shape and size with the variation of the material and damage parameters is assessed. The analysis is performed both on three-dimensional (3D) yield surfaces and the corresponding two-dimensional (2D) projections on the deviatoric plane and/or on the axisymmetric plane, i.e. the plane defined by the condition $\Sigma_1 = \Sigma_2$. Moreover, the influence of the stress state through the stress triaxiality, hydrostatic stress and the sign of J_3^{Σ}, particularly for axisymmetric loadings, is further analysed and discussed.

Regarding the strategy adopted for the determination of the yield loci, a Fortran 90 program was developed, based on several subroutines of DD3MAT in-house code – (developed to perform the identification of the yield criteria parameters). The developed program allows to numerically determine a set of data points in the three-dimensional space, i.e. a point cloud, which satisfy the Stewart & Cazacu (2011) orthotropic yield criterion (see Equation (3.12)). In order to convert the point cloud into 3D surfaces, a MATLAB® program was implemented. Within this code, the surfaces are constructed based on a triangulation method. The scatter points of the 2D projections are obtained from subset solutions of the original numerical point cloud. All the figures presented in this chapter were constructed using MATLAB® programs.

4.1. Influence of the void volume fraction

As stated in previous chapters, micromechanical damage models, such as the CPB06 porous model, are established through the intimate relationship between material porosity and the ductile failure mechanism, relying on the ability to describe the evolution of voids to accurately predict the failure of the material. Being the single internal damage variable, it is of the utmost interest to evaluate the influence of the void volume fraction, f on the yield surface locus, and thus quantify the softening effect of the material. In order to accomplish

this, several yield surfaces where generated for three virtual materials displaying different tension–compression asymmetries (as in Subsection 3.1), rewritten here for the reader's convenience:

- $k = 0 \ \ (\sigma_T/\sigma_C = 1),$ which corresponds to a von Mises material;
- $k = 0.3098 \ \ (\sigma_T/\sigma_C = 1.21),$ corresponding to a fully-dense isotropic BCC material;
- $k = -0.3098 \ (\sigma_T/\sigma_C = 0.83),$ corresponding to a fully-dense isotropic FCC material.

Thus, throughout the chapter, in addition to the main objective of the sensitivity analysis, a parallel study will be carried out regarding the influence of the SD effects on the yield loci. The influence of the void volume fraction, f on the yield surface is evaluated through several three-dimensional (3D) and two-dimensional (2D) yield surface representations – namely π-plane representations and axisymmetric plane projections of the 3D yield locus.

4.1.1. Three-dimensional yield surface representations

In order to facilitate the analysis of the yield surfaces, the usual three-dimensional Cartesian system $(\Sigma_1, \Sigma_2, \Sigma_3)$ is transformed into a cylindrical coordinate system normal to the π-plane, i.e. referred to the hydrostatic axis. As an example, the mentioned coordinate system transformation is illustrated in Figure 4.1. The closed-form surface of Figure 4.1 (a) corresponds to the solution of the yield criterion, $\varphi(\boldsymbol{\Sigma}', k, \sigma_T, f) = 0$ (Equation (3.24)) in the $(\Sigma_1, \Sigma_2, \Sigma_3)$ space). The surface represented in Figure 4.1 (b) is obtained by multiplying each point by the appropriate orthogonal rotation matrix, **R**, namely:

$$\mathbf{R} = \begin{bmatrix} 1/\sqrt{2} & -1/\sqrt{2} & 0 \\ -1/\sqrt{6} & -1/\sqrt{6} & 2/\sqrt{6} \\ 1/\sqrt{3} & 1/\sqrt{3} & 1/\sqrt{3} \end{bmatrix}. \tag{4.1}$$

Note that the cylindrical coordinate system adopted in Figure 4.1 (b) allows a more compact solution and an improved perception of the surface contours and dimension thorough the hydrostatic axis, (Σ_m/σ_T). Moreover, as a result of the coordinate system transformation, it is not possible to associate a clear physical meaning to the perpendicular axes defined on the bottom plane of Figure 4.1 (b), which contains some π-plane projections.

Figure 4.2 to Figure 4.4 show three-dimensional representations of the CPB06 porous model for different values of the void volume fraction, considering the three values of the material parameter *k*, which describes the SD effects. All representations were obtained

fixing the void interaction parameters of Equation (3.24) to $q_1 = 1.5$, $q_2 = 1$ and $q_3 = q_1^2$, as suggested by Tvergaard (1982).

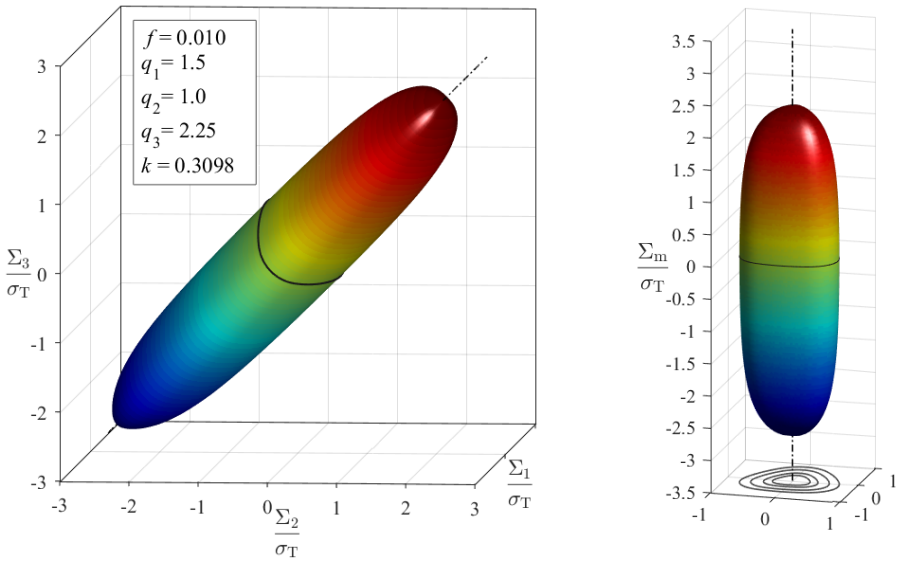

(a) (b)

Figure 4.1. Coordinate system transformation performed to represent the 3D yield surfaces: (a) three-dimensional Cartesian system $(\Sigma_1, \Sigma_2, \Sigma_3)$; (b) three-dimensional cylindrical coordinate system.

As discussed in Chapter 3, when the homogenized material is void-free, $f = 0$, the yield criterion $\varphi(\boldsymbol{\Sigma}', k, \sigma_T, f)$ given in Equation (3.24) reduces to that of the matrix material, i.e. the isotropic and quadratic form of the CPB06 yield criterion (see Equation (3.7)). This limit solution of the porous model is illustrated in Figure 4.2. It can be verified that, being pressure-insensitive, that is, by neglecting the effects of the first invariant of the stress tensor, I_1^{Σ}, the radial and angular coordinates of the yield surfaces are independent of the height coordinate – the mean stress, Σ_m. Indeed, the surfaces will not converge at any point, being infinite along the hydrostatic axis. This behaviour demonstrates the incompressible nature of the matrix material. Additionally, note that when the matrix material presents no tension–compression asymmetry (see Figure 4.2 (a)), the CPB06 porous model further reduces to the von Mises yield criterion, which is J_3^{Σ} - independent, i.e. the yield locus in the π-plane is a circle.

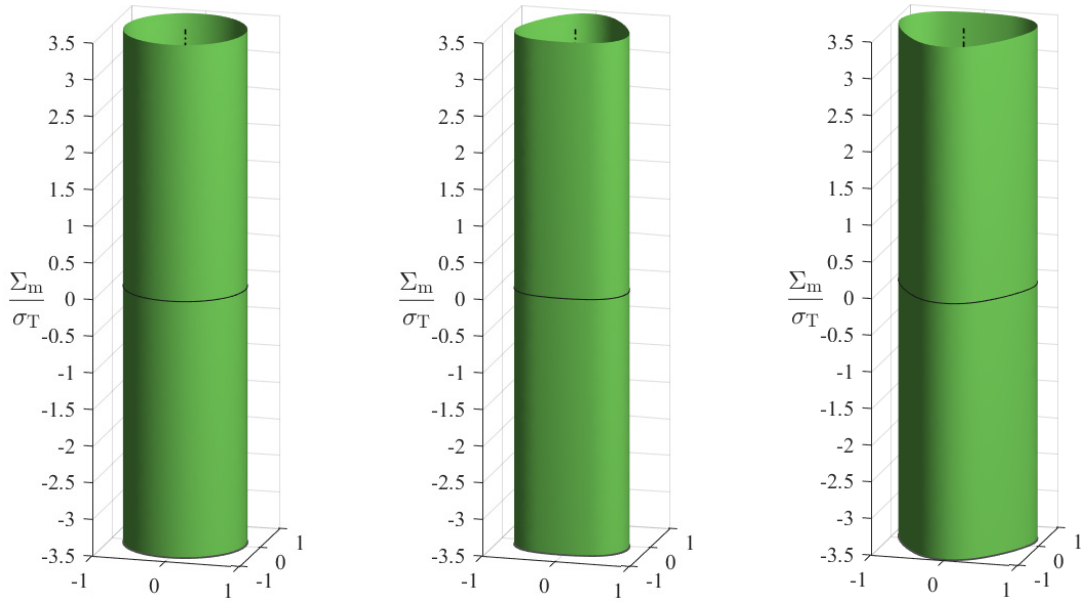

(a) (b) (c)

Figure 4.2. 3D representation of the CPB06 porous model for a void-free material ($f = 0$): (a) no tension-compression asymmetry ($k = 0$); (b) yield strength in tension greater than in compression ($k = 0.3098$); (c) yield strength in tension lower than in compression ($k = –0.3098$).

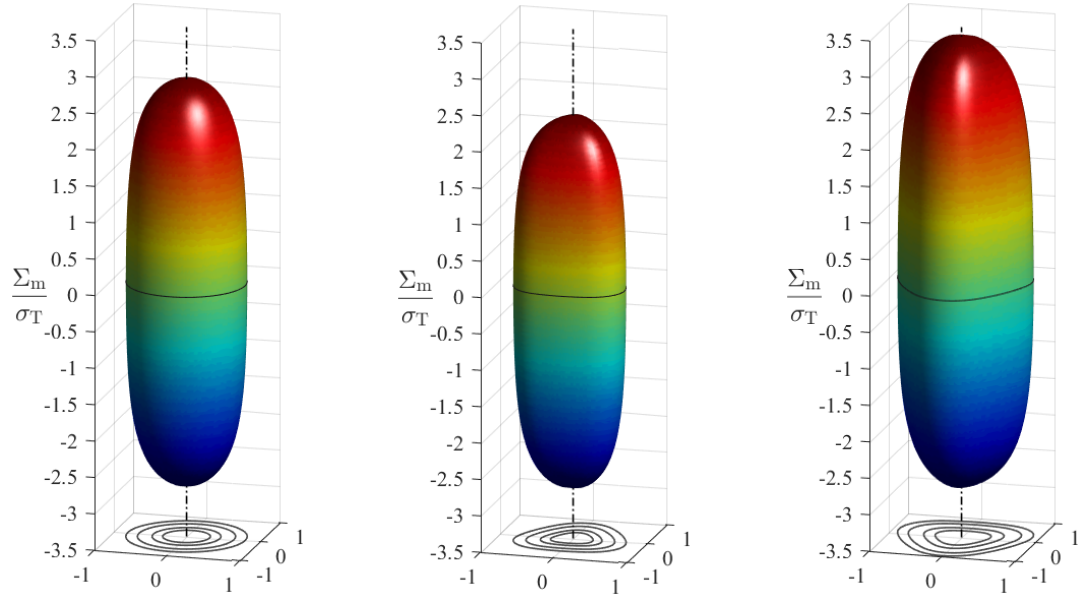

(a) (b) (c)

Figure 4.3. 3D representation of the CPB06 porous model for a material with $f = 0.010$: (a) no tension-compression asymmetry ($k = 0$); (b) yield strength in tension greater than in compression ($k = 0.3098$); (c) yield strength in tension lower than in compression ($k = –0.3098$).

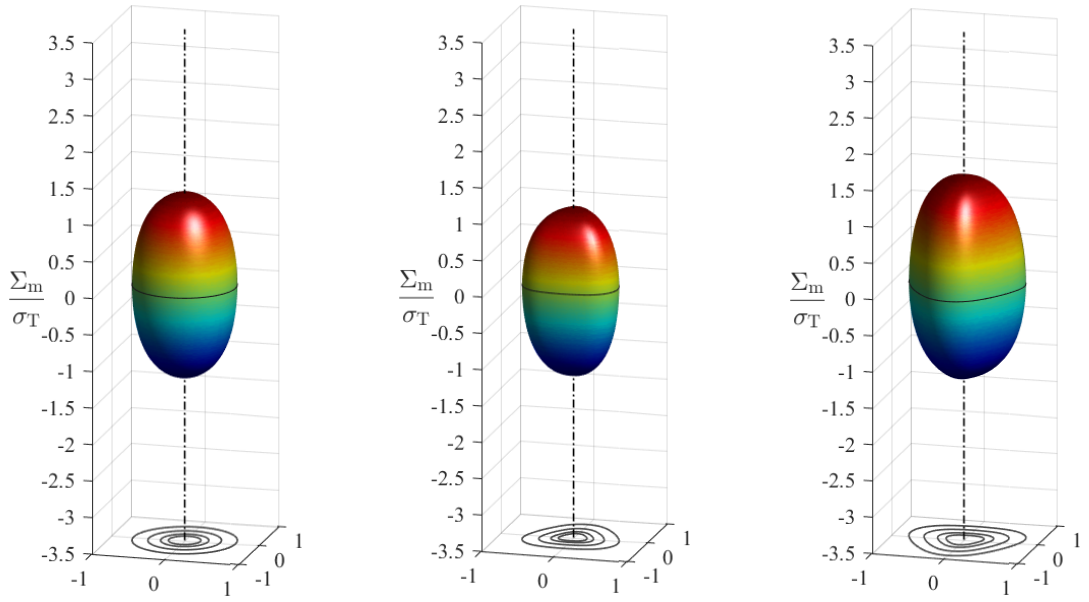

Figure 4.4. 3D representation of the CPB06 porous model for a material with $f = 0.100$: (a) no tension-compression asymmetry ($k = 0$); (b) yield strength in tension greater than in compression ($k = 0.3098$); (c) yield strength in tension lower than in compression ($k = -0.3098$).

Figure 4.3 shows the effect of the presence of voids in the homogenized material ($f = 0.01$). As soon as porosity arises, the yield surfaces become finite along the hydrostatic axis, i.e. the porous aggregate is considered to be compressible, recovering its sensitivity to I_1^{Σ}. Moreover, if SD effects are present, the yield loci is no longer symmetric with respect to the middle plane, defined by $\Sigma_m = 0$. Since the three materials are assumed to have the same yield strength in *tension*, σ_T, yielding at *compressive* hydrostatic loading occurs in all cases at the same distance from the $\Sigma_m = 0$ plane, as stated in Equation (3.27). This reinforces the idea that the SD effects are irrelevant in the definition of the lower vertex of the yield surfaces. However, since the materials have different yield strengths in *compression*, σ_C, yielding at *tensile* hydrostatic loading occurs for three different values of mean stress, $\hat{p}_Y^+$ (see Equation (3.26)). Note the curious result that higher values of the yield strength in compression lead to higher values for the yield hydrostatic stress in tension, i.e. the tensile hydrostatic limit occurs for an higher value of Σ_m / σ_T. Further analysing the plots, it can be concluded that the yield surfaces present their maximum dimension along the deviatoric plane at $\Sigma_m = 0$. By moving away from this plane, i.e. as the mean stress increases

towards either tensile or compressive hydrostatic limits (the surface vertices), the surfaces shrink in the deviatoric plane. Note that, despite changing its size, the shape of the yield locus in the deviatoric plane is governed by the tension-compression asymmetry of the matrix, through the sign and magnitude of the material parameter *k*. Furthermore, the variation of the size of the surface in the π-plane with the distance to the plane $\Sigma_m = 0$ does not appear to be linear. This subject will be recovered in a following subsection where a sensitivity analysis will be carried out by varying the mean stress, Σ_m. Lastly, it should be mentioned that, when no tension-compression asymmetry is displayed, the matrix obeys the classical von Mises yield criterion, hence the surface plotted in Figure 4.3 (a) matches to the well-known GTN model, given by Equation (2.24).

Figure 4.4 shows the yield surfaces of the same porous aggregates as in Figure 4.3, but with a ten times higher porosity, $f = 0.10$. The reduction of the size of the surfaces is evident, especially the distance between the vertices along the hydrostatic axis. It seems that the increase of the void volume fraction changes the proportions of the yield locus to account for the reduction of the load-bearing area and the subsequent softening effect.

4.1.2. Two-dimensional yield surface representations

The surfaces represented in the three-dimensional space allowed to study the global behaviour of the porous aggregates when varying the porosity. A complementary analysis is now carried out through two-dimensional projections to further understand the influence of the void volume fraction, f on the definition of the yield locus. In particular, some deviatoric π-plane projections are presented in order to evaluate the reduction of size of the yield locus on this plane. Additionally, axisymmetric projections are carry out to compare the reduction of the yield surface dimensions along the hydrostatic axis *versus* along the deviatoric plane, i.e. to evaluate the yield surface proportions during the damage accumulation.

Figure 4.5 illustrates π-plane representations for the CPB06 porous model ductile criterion $\varphi(\boldsymbol{\Sigma}', k, \sigma_T, f) = 0$ (see Equation (3.24)) for the three materials considered in this study, for a fixed hydrostatic stress, $\Sigma_m = 0$. Regardless of the shape of the yield loci, which is ruled by the SD effects, it is shown that the surfaces shrink in the deviatoric plane as the porosity increases. Note that, if the material exhibits tension-compression asymmetry, the reduction of the radial coordinate is not equal in all directions, i.e. the softening depends on

the angular coordinate – otherwise the surfaces would change their original shape. However, the successive decrements of the radial coordinate, resulting from the increase of porosity, have the same value along the principal axes for all three materials. Furthermore, along the principal axes, the reduction of the radial coordinate seems to vary linearly with the porosity. In order to confirm this observation, Equation (3.40), derived for axisymmetric loadings in the previous chapter, is recovered. Trivially, the derivative of Σ_e/σ_T in order to the void volume fraction is constant. On other hand, note that for purely deviatoric loadings $(\Sigma_m = 0)$ with $J_3^{\Sigma} > 0$ the principal axis Σ_3/σ_T of Figure 4.5 is collinear with Σ_e/σ_T, given in Equation (3.40). Moreover, due to the isotropy assumption, the distance relative to the hydrostatic axis (i.e. the radius) of the yield surface points contained in the deviatoric plane at $\Sigma_m = 0$ and intercepted by the principal axes Σ_i/σ_T with $i = 1,2,3$ is the same in the three directions. Therefore, in analogy with the analysis performed with Equation (3.40):

$$\frac{\partial}{\partial f}\left(\frac{\Sigma_i}{\sigma_T}\right) = \frac{\partial}{\partial f}\left(1 - q_1 f\right) = -q_1 \quad \text{with } i = 1,2,3. \tag{4.2}$$

This means that the yield locus sensitivity to porosity in the π-plane is *constant* and quantified by the fitting parameter q_1. The radial coordinate of the yield locus intercepted by the principal axes is a linear function of the void volume fraction, f and it is independent of the SD effects. Although not represented in Figure 4.5, as a limit case, the surfaces would converge into a single point when the void volume fraction reached its ultimate value, i.e. $f \to 1/q_1$ or $f^* \to f_U^* = 1/q_1$ if the effective void volume fraction concept proposed by Tvergaard & Needleman (1984) is considered.

The previous analysis was performed for a single mean stress value, $\Sigma_m = 0$. A fundamental question that arises is how the increasing porosity of the aggregate effects the entire range of the yield surface along the hydrostatic axis. For this purpose, the projection of the yield locus $\varphi(\boldsymbol{\Sigma}', k, \sigma_T, f) = 0$, given in Equation (3.24), on the axisymmetric plane $(\Sigma_{11} = \Sigma_{22})$ is also constructed. This projection is obtained through the intersection of the three-dimensional yield surface with the axisymmetric plane, as shown in Figure 4.6. The resulting bi-dimensional contour can be transformed into a coordinate system defined in the stress space $(\Sigma_m, \Sigma_{11} - \Sigma_{33})$ where the mean stress, Σ_m is given by Equation (3.29) and the other axis, $(\Sigma_{11} - \Sigma_{33})$ is defined according with the von Mises equivalent stress, Σ_e given in Equation (3.30).

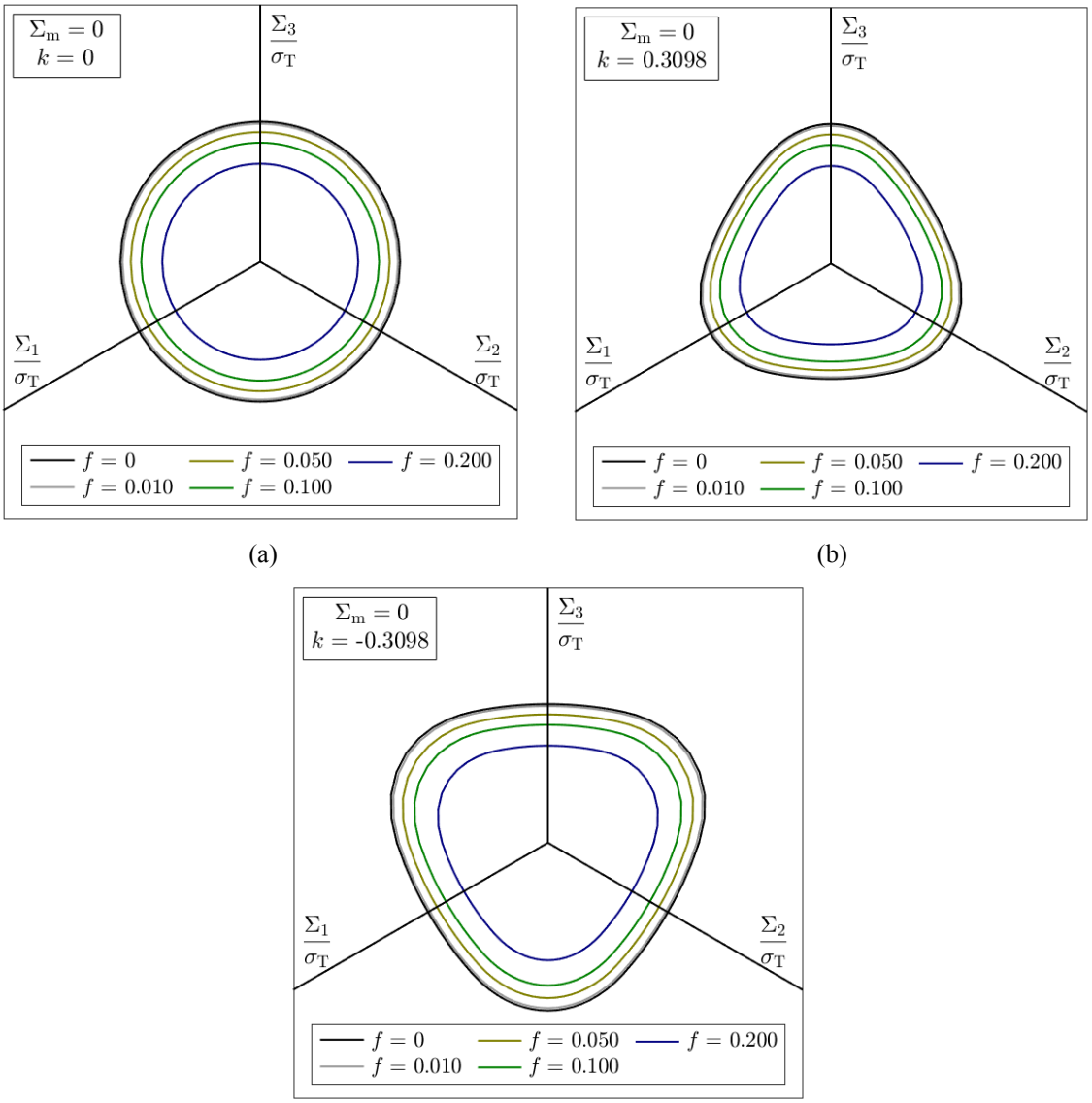

Figure 4.5. Deviatoric plane representation of the CPB06 porous model varying the void volume fraction: (a) no tension-compression asymmetry ($k = 0$); (b) yield strength in tension greater than in compression ($k = 0.3098$); (c) yield strength in tension lower than in compression ($k = –0.3098$).

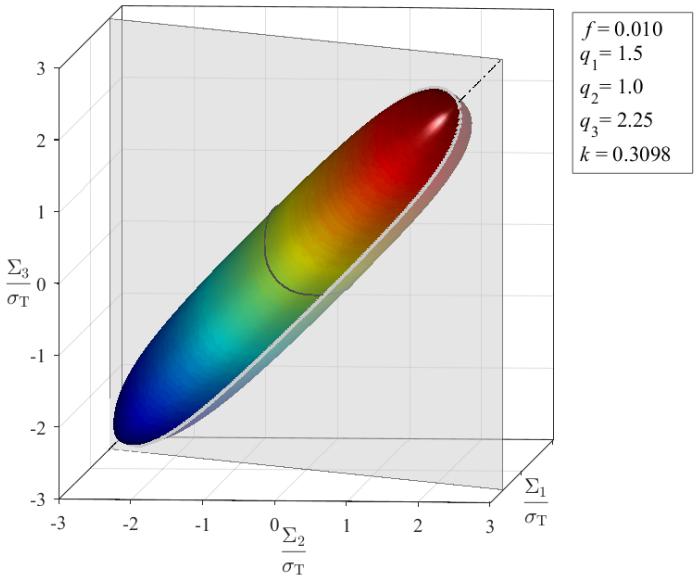

Figure 4.6. Intersection of an isotropic CPB06 porous yield surface with the axisymmetric plane ($\Sigma_{11} = \Sigma_{22}$).

Figure 4.7 shows the projections on the axisymmetric plane of each of the three materials, for the same values of porosity as in the previous analysis. As seen in the 3D representations, a clear reduction of the size of the yield loci along the hydrostatic axis is evidenced when increasing the void volume fraction. Furthermore, a change of the proportions of the yield locus is also observed. The change of shape shown in the axisymmetric plane is due to the distinct response of the yield surface along the hydrostatic axis and on the π-plane. For the porosity values tested, regardless of the SD effects, the yield locus sensitivity to porosity in the hydrostatic axis is much higher than in the π-plane, as small variations of the porosity value tend to greatly reduce the size of the yield projection on the former. However, unlike the π-plane case, the sensitivity of the yield locus to the porosity along the hydrostatic axis is not constant. This statement can be confirmed through the analysis of the derivative of the compressive hydrostatic limit, $\hat{p}_Y^-$ (given in Equation (3.27)) with respect to f, such that:

$$\frac{\partial}{\partial f}\left(\frac{p_Y^-}{\sigma_T}\right) = \frac{\partial}{\partial f}\left(\frac{2}{3q_2}\ln\left(q_1 f\right)\right) = \left(\frac{2}{3q_2}\right)\frac{1}{f}. \tag{4.3}$$

It is concluded that the sensitivity of the yield surface size along the hydrostatic axis is inversely proportional to the porosity value and to the fitting parameter q_2. Thus, although for relatively low values of porosity the sensitivity on the hydrostatic axis is dominant, one can expect that there is an instant (i.e. a void volume fraction value, f) at which the sensitivity to the porosity in the π-plane will prevail. This implies that the projections of the

yield loci, initially comparable to an oblate ellipse, will eventually become prolate. In other words, the capacity of the porous solid to withstand purely deviatoric loadings will become greater than purely hydrostatic ones. As in the projections on the deviatoric plane, the yield loci of Figure 4.7 will converge into a single point when the void volume fraction reaches its ultimate value, i.e. $f \to 1/q_1$.

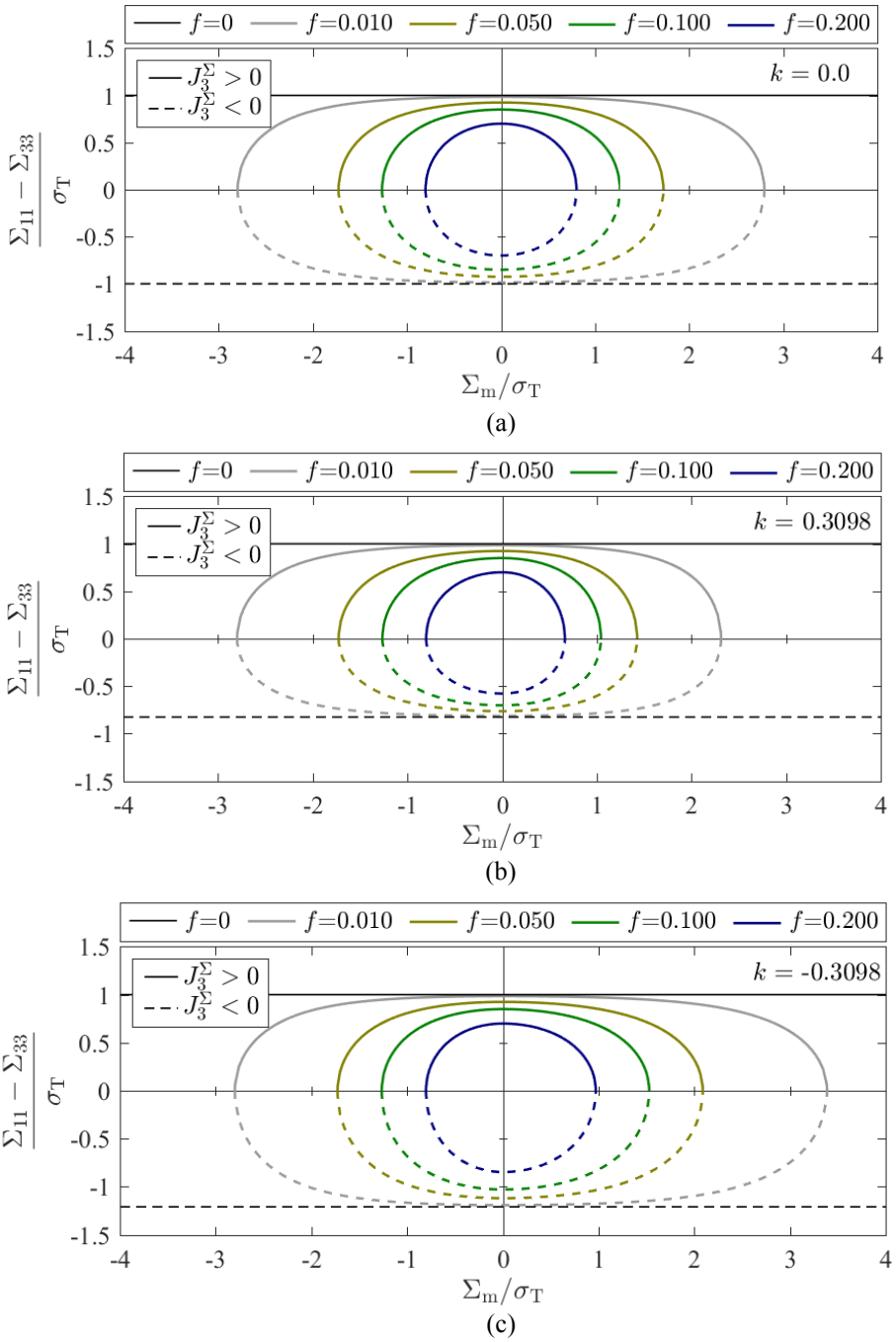

Figure 4.7. Axisymmetric plane projections of the CPB06 porous model varying the void volume fraction: (a) no tension-compression asymmetry ($k = 0$); (b) yield strength in tension greater than in compression ($k = 0.3098$); (c) yield strength in tension lower than in compression ($k = -0.3098$).

4.2. Influence of the stress state

As outlined in the previous chapters, the *stress state* plays a key role in the description of the ductile fracture. Recall that, concerning the study of ductile fracture mechanics, the stress state is often described by two dimensionless parameters: the stress triaxiality, T_Σ and the Lode angle parameter, $\overline{\theta}_\Sigma$ (quantifying J_3^Σ). In fact, as discussed previously, the stress state, particularly the stress triaxiality, is responsible for determining the active void growth micro-mechanism: shape changing *versus* volumetric changing void growth. Consequently, it is important to understand how a stress state affects the yield criterion and how can it be visualized both on a three-dimensional and on a two-dimensional space.

This section discusses the influence of the stress state on the CPB06 porous yield loci for three virtual materials displaying different tension–compression asymmetries (as in Subsection 4.1). Firstly, the sensitivity of the deviatoric plane projections to the mean stress, Σ_m is analysed. Following it, 3D representations are shown, illustrating the intersection of the yield loci with a surface of constant stress triaxiality. This analysis is complemented with a 2D projection on the axisymmetric plane, illustrating graphically the stress triaxiality and its influence on the yielding of the three materials displaying different SD effects.

4.2.1. Effect of the mean stress on the deviatoric plane projections

Figure 4.8 shows π-plane representations of the CPB06 porous yield criterion $\varphi(\boldsymbol{\Sigma}', k, \sigma_T, f) = 0,$ given in Equation (3.24), for the three materials considered in this study, and for a fixed void volume fraction value, $f = 0.01.$ As observed in the 3D representations of Subsection 4.1.1, it is confirmed that the yield surfaces shrink in the deviatoric plane as the mean stress, Σ_m tends to it ultimate value, $\hat{p}_Y^+$ – the tensile hydrostatic yield stress (see Equation (3.26)). This behaviour is similar for all materials. Such as in the study of the influence of the porosity in the π-plane for a fixed value of the mean stress (see Figure 4.5), the yield surfaces of Figure 4.8 decrease in size but retain their original shape. This enforces that the shape of the yield locus on the deviatoric plane is solely governed by the tension–compression asymmetry, through the sign and magnitude of the material parameter *k*.

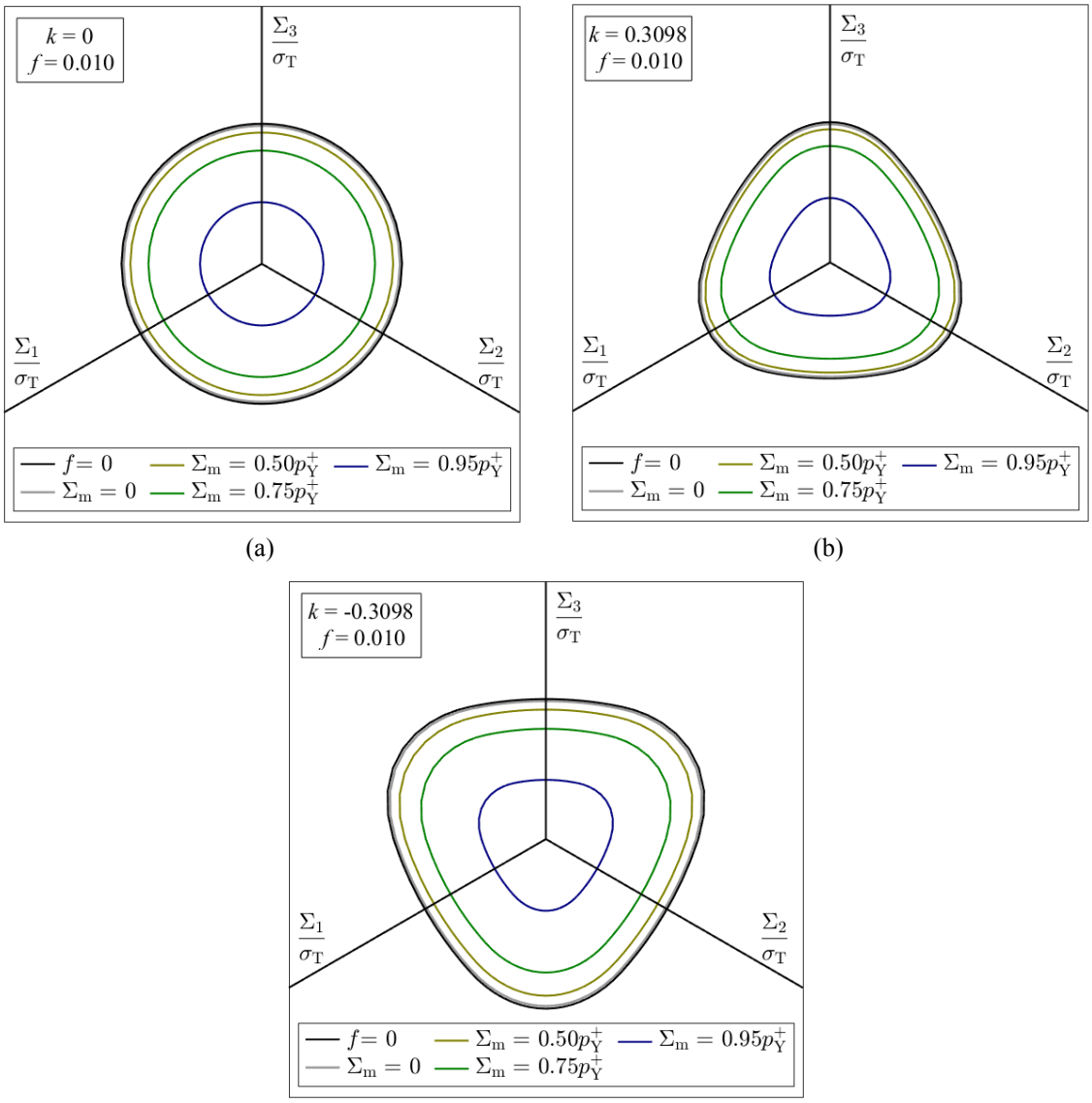

Figure 4.8. Deviatoric plane representation of the CPB06 porous model varying the mean stress: (a) no tension-compression asymmetry ($k = 0$); (b) yield strength in tension greater than in compression ($k = 0.3098$); (c) yield strength in tension lower than in compression ($k = -0.3098$).

According to Figure 4.8, the yield surfaces present their maximum radii along the deviatoric plane for $\Sigma_m = 0$. As the mean stress increases towards its tensile hydrostatic limit, $\Sigma_m \to p_Y^+$, the radial coordinate decreases but, in this case, not linearly. In fact, the yield surface sensitivity to the mean stress *increases continuously* with its absolute value. This remark can be verified by analysing any quadrant of the axisymmetric plane projections plots represented in Figure 4.7. One can observe that, regardless of the porosity value, the slope of the yield surfaces varies between zero (in the deviatoric plane at $\Sigma_m = 0$) to infinity when

the mean stress reaches its limit value, $\Sigma_{\mathrm{m}} = p_{\mathrm{Y}}^{+}$ or $\Sigma_{\mathrm{m}} = p_{\mathrm{Y}}^{-}$. A mathematical proof of these remarks can be obtain by evaluating the slope of the yield locus at any quadrant, i.e. the partial derivative $\partial\Sigma_e/\partial\Sigma_{\mathrm{m}}$ of any branch of Equation (3.41) or Equation (3.42). For instance, taking the first quadrant of the yield loci of Figure 4.7, i.e. $(\Sigma_{\mathrm{m}} > 0,\ J_3^{\Sigma} > 0)$ it is possible to prove that:

$$\left.\frac{\partial\Sigma_{\mathrm{e}}}{\partial\Sigma_{\mathrm{m}}}\right|_{\Sigma_{\mathrm{m}}>0,\ J_3^{\Sigma}>0} = -\frac{3}{2}\frac{q_1 q_2 f \sinh\left(\frac{\sigma_{\mathrm{T}}}{\sigma_{\mathrm{C}}}\right)\left(\left(\frac{\sigma_{\mathrm{T}}}{\sigma_{\mathrm{C}}}\right)\frac{3q_2\Sigma_{\mathrm{m}}}{2\sigma_{\mathrm{T}}}\right)}{\sqrt{1-2q_1 f\cosh\left(\left(\frac{\sigma_{\mathrm{T}}}{\sigma_{\mathrm{C}}}\right)\frac{3q_2\Sigma_{\mathrm{m}}}{2\sigma_{\mathrm{T}}}\right)+q_3 f^2}} \tag{4.4}$$

which is a monotonically increasing function where:

$$\lim_{\Sigma_{\mathrm{m}}\to 0}\left(\frac{\partial\Sigma_{\mathrm{e}}}{\partial\Sigma_{\mathrm{m}}}\right) = 0 \quad \text{and} \quad \lim_{\Sigma_{\mathrm{m}}\to p_{\mathrm{Y}}^{+}}\left(\frac{\partial\Sigma_{\mathrm{e}}}{\partial\Sigma_{\mathrm{m}}}\right) = \infty \tag{4.5}$$

The conclusion holds true for the other quadrants. The plots of Figure 4.8 only show curves for a single void volume fraction ($f = 0.01$); however the porosity value also affects the yield loci sensitivity to the mean stress, i.e. the rate at which the projected area in the π-plane decreases whit increasing hydrostatic stress (tensile or compressive). By analysing Figure 4.7 and/or Equation (4.4) it is possible to verify that the sensitivity to the mean stress increases with the increase of the porosity. In other words, there is a sooner and shaper reduction of the dimension along the deviatoric plane with respect to the mean stress normalized by its ultimate value, $\hat{p}_{\mathrm{Y}}^{+}$ or $\hat{p}_{\mathrm{Y}}^{-}$.

4.2.2. Effect of the stress triaxiality

It is well-known that the stress triaxiality, T_{Σ} is defined by the ratio between the mean stress and the equivalent von Mises stress (see Equation (2.6)). However, the visualization of this parameter in the three-dimensional space or even in the two-dimensional space may not be evident. This subsection intends to address this subject.

By itself, the stress triaxiality is incapable of fully defining a stress state. In the fracture mechanics framework, the pair $(T_{\Sigma}, \overline{\theta}_{\Sigma})$ is often used to define the direction of the principal stress vector, $(\Sigma_1, \Sigma_2, \Sigma_3)$ and, complementary, the mean stress or the equivalent stress is used to set its magnitude. Indeed, three independent parameters are required to fully characterize a stress state. With that said, the stress triaxiality alone defines an infinite

surface that contains all the points that verify a specific ratio Σ_m/Σ_e. In the three-dimensional space, this corresponds to the definition of a circular cone, whose vertex coincides with the origin of the coordinate system (both Cartesian and cylindrical), collinear with the hydrostatic axis with an opening angle quantified by the stress triaxiality value. Figure 4.9 shows the intersection of several stress triaxiality cones with the yield loci of the isotropic CPB06 porous model, for three materials displaying different tension-compression asymmetry. The yield surfaces were sectioned to facilitate the visualization of the stress triaxiality cones and the curves resulting from the intersections.

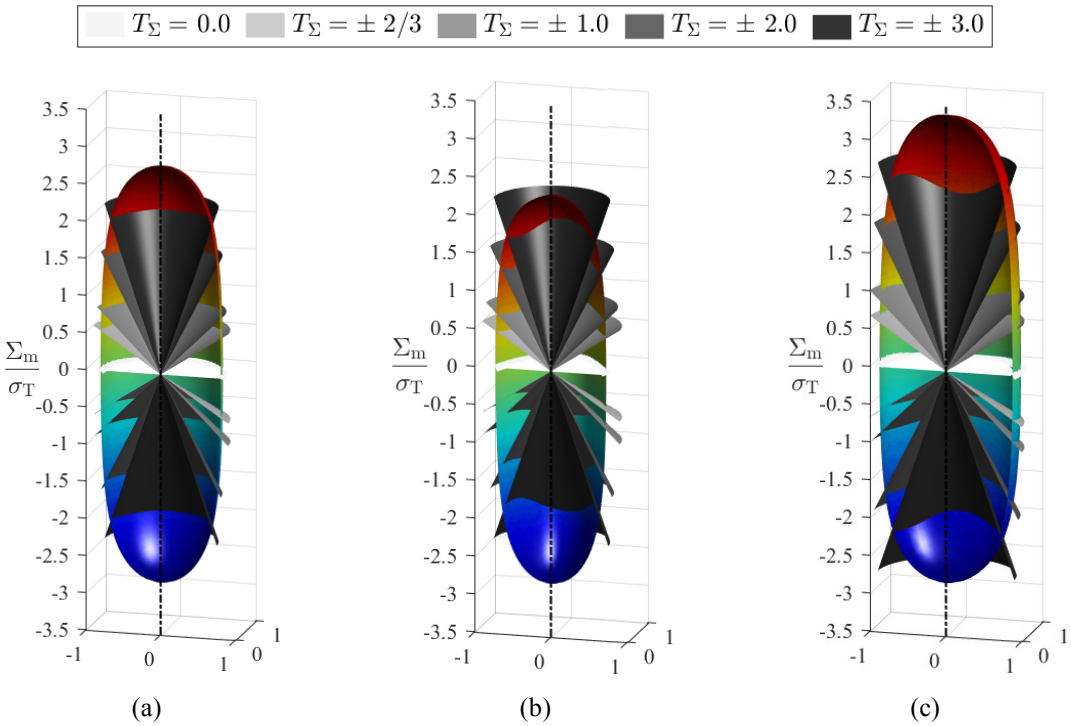

Figure 4.9. 3D section view of the intersection between the CPB06 porous model and several stress triaxialities for a material with $f = 0.010$ and: (a) no tension-compression asymmetry ($k = 0$); (b) yield strength in tension greater than in compression ($k = 0.3098$); (c) yield strength in tension lower than in compression ($k = -0.3098$).

As shown in Figure 4.9 (a) – material with no tension-compression asymmetry – the intersection resultant from any stress triaxiality cone with the yield surface occurs at a fixed mean stress, i.e. results in circles at a constant height with respect to the middle plane, $\Sigma_m = 0$. However, the same does not occurs for the materials exhibiting SD effects, either for $k > 0$ or $k < 0$. In this case, the intersection results in closed curves in which both the radius and the height vary with the angular coordinate. This is due to the fact that the yield loci does not have a circular shape in the π-plane (as in Figure 4.9 (a)). The SD effects,

introduced by the sensitivity to J_3^{Σ}, originate the triangular shape of the yield surfaces. Thus, the von Mises equivalent stress – proportional to the radial coordinate – varies with the angular coordinate and, consequently, the mean stress will also have to vary in order to maintain a constant Σ_m/Σ_e ratio, i.e. a constant stress triaxiality.

The influence of the tension-compression asymmetry on the definition of the intersection point between the yield surface and a specified stress triaxiality value can also be analysed in two-dimensional representations. Figure 4.10 illustrates the axisymmetric plane projections of the CPB06 porous yield criterion, for the three materials considered in this study, and the same stress triaxiality values as in Figure 4.9. Note that in the two-dimensional axisymmetric space $-(\Sigma_m, \Sigma_{11} - \Sigma_{33})$, the cone-shaped geometric surfaces of the previous analysis give rise to simple straight lines through the origin, with a slope quantified by the stress triaxiality value. As stated in Subsection 3.3, under axisymmetric stress states two cases can be distinguished:

i. $\Sigma_{33} > \Sigma_{11}$, which corresponds to $J_3^{\Sigma} > 0$ and $\overline{\theta}_{\Sigma} = 1$;

ii. $\Sigma_{33} < \Sigma_{11}$, which corresponds to $J_3^{\Sigma} < 0$ and $\overline{\theta}_{\Sigma} = 1$.

According to Figure 4.10 it is verified that, if SD effects are displayed, the intersection of the constant triaxiality lines with the yield locus does not occur at the same abscissa, Σ_m for $J_3^{\Sigma} > 0$ and $J_3^{\Sigma} < 0$.

Moreover, note that, with the exception of the second quadrant $(\Sigma_m < 0 \wedge J_3^{\Sigma} > 0)$, for which SD effects do not manifest in the yield surface shape – see Equation (3.42)), the contours characterized by $k > 0$ are contained within the von Mises yield locus and the contours with $k < 0$ are the outermost. For the other quadrants, this means that, regardless of the imposed stress triaxiality, in axisymmetric loadings the plastic flow will occur first in the material with yield strength in tension greater than in compression $(k > 0)$. Although it may seem a counter-intuitive result for loadings with $\Sigma_m > 0$, this behaviour is supported by numerical simulations on unit cells/RVEs (Cazacu & Stewart, 2009; Lebensohn & Cazacu, 2012; Stewart & Cazacu, 2011). In the next chapter, elementary numerical simulations will be performed in order to study of the response of the porous model to axisymmetric loadings and Figure 4.10 will be revised to understand and justify the results obtained.

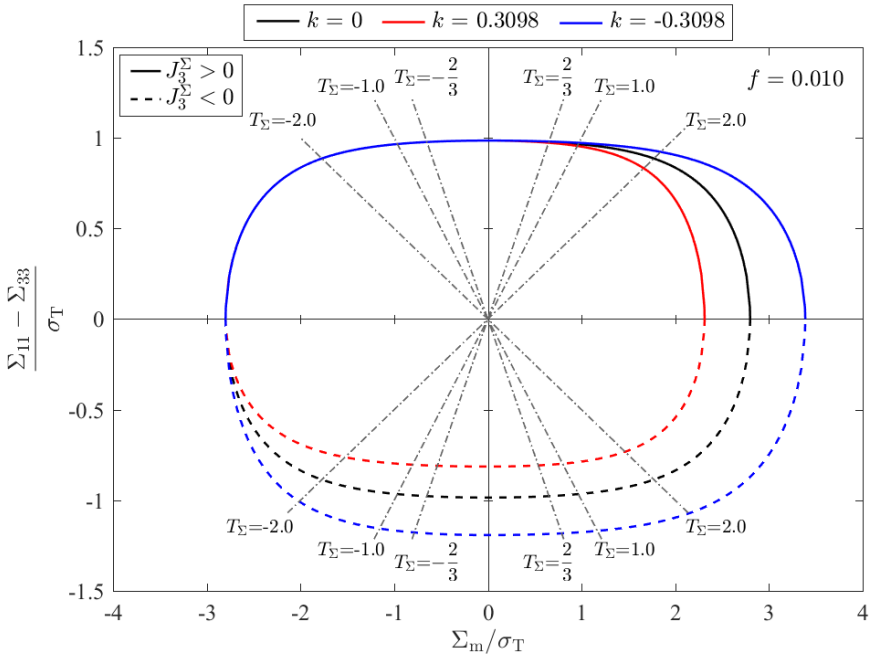

Figure 4.10. Axisymmetric plane projections of the CPB06 porous model for a material with $f = 0.010$ and: (a) no tension-compression asymmetry ($k = 0$); (b) yield strength in tension greater than in compression ($k = 0.3098$); (c) yield strength in tension lower than in compression ($k = –0.3098$).

5. Assessment of the Damage Model Response through Elementary Numerical Tests

Although several micromechanical FEA on three-dimensional unit cells[2] have been conducted showing the importance of SD effects on the dilatational response of porous solids, to the author's knowledge, an assessment of the capability of the CPB06 porous model to replicate the mechanical behaviour predicted in the unit cell simulations is still lacking.

In order to fill this gap, in this chapter a numeric analysis is conducted in order to evaluate the ability of the damage model to effectively describe the plastic flow of the matrix and the accumulated damage in porous solids exhibiting tension–compression asymmetry. For this purpose, single-element tests are carried out for macroscopic axisymmetric stress states, corresponding to a fixed stress triaxiality value and the two corresponding possible values of the Lode parameter (or sign of J_3^{Σ}); as well as for hydrostatic loadings, both tensile and compressive. A brief sensitivity analysis will also be carried out regarding the matrix isotropic hardening law parameters.

5.1. Numerical model

The computations were conducted on a single initially cubic 8-node hexahedral finite element (FE) with a side length C_0. Let $(\mathbf{e}_1, \mathbf{e}_2, \mathbf{e}_3)$ be the reference frame representing the lateral and axial directions, respectively; **u** the incremental displacement between the current and the reference configuration and **t** the prescribed Cauchy stress vector (defined on the current configuration). The boundary conditions are imposed to the element as in Alves et al., (2014), i.e. symmetry at $\mathbf{e}_1 = 0$, $\mathbf{e}_2 = 0$ and $\mathbf{e}_3 = 0$:

$$\begin{aligned} &u_1(0,e_2,e_3)=0, \quad t_2(0,e_2,e_3)=0, \quad t_3(0,e_2,e_3)=0; \\ &u_2(e_1,0,e_3)=0, \quad t_1(e_1,0,e_3)=0, \quad t_3(e_1,0,e_3)=0; \\ &u_3(e_1,e_2,0)=0, \quad t_1(e_1,e_2,0)=0, \quad t_2(e_1,e_2,0)=0, \end{aligned} \tag{5.1}$$

and to the opposite FE surfaces as:

[2] Assuming that the porous solid contains a regular array of initially spherical voids, the *unit cell* is modelled as a cubic cell containing a single initially spherical cavity and the matrix obeys to the classic CPB06 yield criterion.

$$\begin{aligned} &u_1(C_0,e_2,e_3)=u_1^*(t), \quad t_2(C_0,e_2,e_3)=0, \quad t_3(C_0,e_2,e_3)=0;\\ &u_2(e_1,C_0,e_3)=u_2^*(t), \quad t_1(e_1,C_0,e_3)=0, \quad t_3(e_1,C_0,e_3)=0;\\ &u_3(e_1,e_2,C_0)=u_3^*(t), \quad t_1(e_1,e_2,C_0)=0, \quad t_2(e_1,e_2,C_0)=0. \end{aligned} \tag{5.2}$$

By forcing the Cauchy stress components coplanar to each plane to be zero, initially parallel faces will remain parallel after deformation and are shear-free. Figure 5.1 (a) depicts the modelled FE and the imposed boundary conditions. In the previous equation $u_1^*(t)$, $u_2^*(t)$ and $u_3^*(t)$ are the time histories of the incremental displacements, determined such that the macroscopic true stresses $(\Sigma_{11},\Sigma_{22},\Sigma_{33})$ follow a proportional loading history given, for axisymmetric stress states $(\Sigma_{11}=\Sigma_{22})$, by the constant ρ defined in Section 3.3 as:

$$\rho=\frac{\Sigma_{33}}{\Sigma_{11}}, \tag{3.33}$$

The current FE side dimensions, C_i with $i=1,2,3$ are computed by:

$$C_i=C_0+u_i^*(t). \tag{5.3}$$

Hence, the macroscopic true stresses Σ_{11}, Σ_{22} and Σ_{33} are defined as (see Figure 5.1 (b)):

$$\begin{aligned} &\Sigma_{11}=\frac{1}{C_2C_3}\int_0^{C_2}\int_0^{C_3} t_1\ de_3de_2, \quad \Sigma_{22}=\frac{1}{C_1C_3}\int_0^{C_1}\int_0^{C_3} t_1\ de_3de_1,\\ &\Sigma_{33}=\frac{1}{C_1C_2}\int_0^{C_2}\int_0^{C_1} t_3\ de_1de_2. \end{aligned} \tag{5.4}$$

For each time increment, the three imposed macroscopic true stresses on each planar surface of the FE model are continuously updated in order to ensure that the condition of constant proportionality (given in Equation (3.33)) on the final equilibrated configuration is verified. In other words, it is ensured that the macroscopic stress triaxiality, T_Σ remains constant throughout the entire deformation history. Knowing the current FE dimensions, C_i with $i=1,2,3$ the macroscopic principal strains (E_1,E_2,E_3) are calculated as follows:

$$E_1=\ln\left(\frac{C_1}{C_0}\right), \quad E_2=\ln\left(\frac{C_2}{C_0}\right), \quad E_3=\ln\left(\frac{C_3}{C_0}\right), \tag{5.5}$$

hence the second-invariant of the macroscopic principal strain tensor J_2^{E} is given by:

$$J_2^{\mathrm{E}}=\sqrt{\frac{1}{2}\left({E_1}^2+{E_2}^2+{E_3}^2\right)}, \tag{5.6}$$

and the macroscopic von Mises equivalent strain, E_{e} as:

$$E_{\mathrm{e}}=\frac{2\sqrt{3}}{3}J_2^{\mathrm{E}}. \tag{5.7}$$

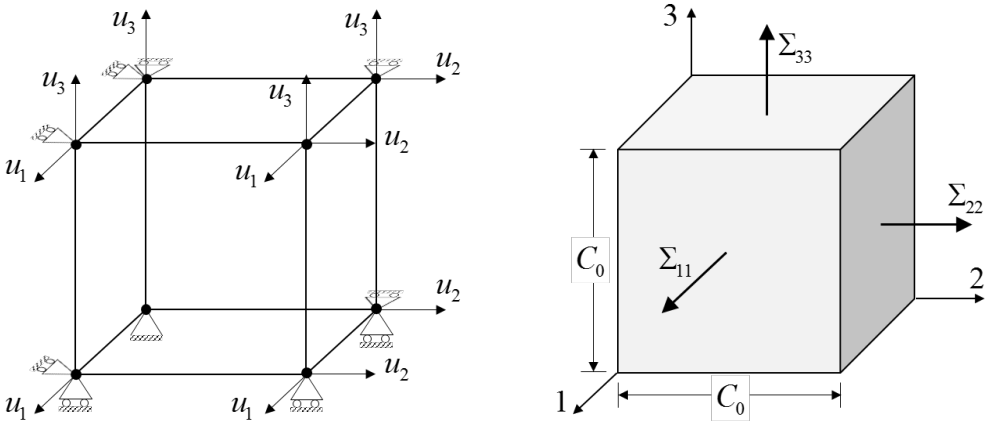

Figure 5.1. Modelled finite-element: (a) imposed boundary conditions; (b) imposed macroscopic loading and initial dimensions.

All the FE numerical simulations were carried out with the in-house quasi-static elastoplastic implicit finite element solver DD3IMP (Menezes & Teodosiu, 2000; Oliveira, Alves, & Menezes, 2008). A single tri-linear solid element was considered associated with a selective reduced integration (SRI) technique. For more details regarding the implementation of the present boundary value problem the reader is referred to the work of Alves et al. (2014).

The response of three porous materials displaying different tension–compression asymmetries is analysed for the SD ratios $(\sigma_{\mathrm{T}}/\sigma_{\mathrm{C}})$ reported by Hosford & Allen (1973), as in Chapter 4. The materials are considered to be isotropic elastic-plastic obeying to the CPB06 porous yield criterion, $\varphi(\boldsymbol{\Sigma}', k, \sigma_{\mathrm{T}}, f) = 0,$ given in Equation (3.24). The elastic behaviour is described by Hooke's law and the matrix tensile hardening behaviour is considered to follow Swift's isotropic hardening power-law, given by:

$$\sigma_{\mathrm{T}} = K\left(\varepsilon_0 + \bar{\varepsilon}_{\mathrm{M}}^{\mathrm{p}}\right)^n, \quad \text{with} \quad \varepsilon_0 = \left(\frac{\sigma_0^{\mathrm{T}}}{K}\right)^{1/n}, \tag{5.8}$$

where σ_{T} is the matrix flow stress, σ_0^{T} is the initial yield strength in tension, $\bar{\varepsilon}_{\mathrm{M}}^{\mathrm{p}}$ is the local equivalent plastic strain of the matrix and *K*, *n* and ε_0 are material parameters. The values for the matrix elastic and hardening parameters were taken to be the same as those considered by Alves & Cazacu (2015) and are resumed in Table 5.1. Additionally, the damage model parameters, namely the void interaction parameters, q_i, the initial void volume fraction, f_0, and the onset of void coalescence, f_{c} are indicated in Table 5.2. The void interaction

parameters are fixed to the numeric values suggested by Tvergaard (1982); the initial void volume fraction is chosen in agreement with unit cell studies such as in Cazacu & Stewart (2009) and Alves & Cazacu (2015a); and the onset of void coalescence is taken such that $f_c/f_0 = 10,$ so that the critical porosity corresponds to a plausible value for metallic materials. In order to facilitate the analysis, the plastic strain controlled nucleation mechanism is neglected, so that the void volume fraction rate of change, $\dot{f}$ is exclusively due to the growth of pre-existing voids. Moreover, as mentioned in Chapter 2, the load-bearing capacity of the material is abruptly reduced when the onset of coalescence is reach. Therefore, by establishing a critical value for the void volume fraction (in the form of f_c), it will be possible to distinguish the onsets of failure for the three materials, allowing to quantify the ductility of the porous solids for a given stress state. Note that, since the parameter k is the only parameter that varies between the three solids, any difference resulting from the simulations for a given stress triaxiality will be due solely to SD effects. The computations are stopped when either one of the two conditions occur: (i) the void volume fraction reaches its arbitrated critical value $(f \geq f_c);$ (ii) the macroscopic effective strain reaches unity $(E_e \geq 1).$

Table 5.1. Elastic properties and hardening law parameters for the three studied materials.

Property	Symbol	Value
Young's modulus	E [GPa]	200
Poisson's coefficient	v	0.33
Hardening coefficient	K/σ_0^T	2.2
Hardening exponent	n	0.1

Table 5.2. Damage model parameters for the ductile failure prediction of the three studied materials.

Property	Symbol	Value
Void interaction parameters	q_1	1.5
	q_2	1.0
	q_3	2.25
Initial void volume fraction	f_0	0.01
Onset of void coalescence	f_c	0.1

5.2. Numerical results

5.2.1. Axisymmetric tensile loadings

Using the FE model, the mechanical response of the porous materials given by the CPB06 damage model will be analysed and discussed for axisymmetric tensile loadings. The study will be performed for the following values of the stress triaxiality: $T_\Sigma = 2/3,\ T_\Sigma = 1$ and $T_\Sigma = 2.$ Recall that for each stress triaxiality two possible axisymmetric stress states can be distinguished by the magnitude of the constant $\rho = \Sigma_{33}/\Sigma_{11},$ responsible for adjusting the ratio between the macroscopic axial and lateral stresses:

i. $\Sigma_{33} > \Sigma_{11},$ which corresponds to $J_3^\Sigma > 0$ and $\overline{\theta}_\Sigma = 1;$

ii. $\Sigma_{33} < \Sigma_{11},$ which corresponds to $J_3^\Sigma < 0$ and $\overline{\theta}_\Sigma = 1.$

The two ρ values that originate the same specified stress triaxiality, T_Σ were determined by Equation (3.34) and are represented in Table 5.3.

Figure 5.2 shows a comparison between the normalized macroscopic von Mises effective stress, Σ_e *versus* the macroscopic effective strain, E_e for the three porous solids corresponding to the FE computations at $T_\Sigma = 2/3,$ for both $J_3^\Sigma > 0$ and $J_3^\Sigma < 0.$ The corresponding void volume fraction evolution, f is shown in Figure 5.3. The void volume fraction rate of grow, $\dot{f}$, is evaluated in function of the macroscopic equivalent strain, $\partial f/\partial E_e,$ and is depicted in Figure 5.4. In each figure and for each material, the onset of failure, (i.e. when the void volume fraction reaches its critical value, $f = f_c$) is marked by a cross symbol, if predicted. Similarly, Figure 5.5 to Figure 5.7 present the same plots and comparisons between the behaviour of the three porous solids for a stress triaxiality of $T_\Sigma = 1$ and Figure 5.8 to Figure 5.10 for a stress triaxiality of $T_\Sigma = 2.$

Table 5.3. Prescribed ratio between the macroscopic axial and lateral stresses for the studied axisymmetric stress triaxiality values.

	$\rho = \Sigma_{33}/\Sigma_{11}$	
Stress Triaxiality	$J_3^\Sigma > 0$	$J_3^\Sigma < 0$
$T_\Sigma = 2/3$	4.0	0
$T_\Sigma = 1$	2.5	0.25
$T_\Sigma = 2$	1.6	4/7

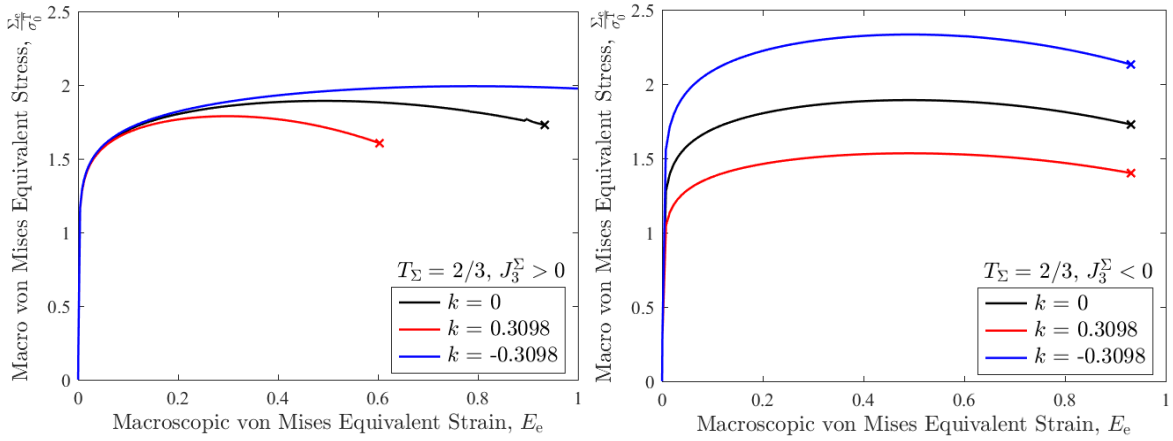

(a) (b)

Figure 5.2. Macroscopic stress–strain response for porous materials displaying distinct SD effects under axisymmetric tensile loadings corresponding to a stress triaxiality $T_\Sigma = 2/3$ and: (a) $J_3^\Sigma > 0$; (b) $J_3^\Sigma < 0$.

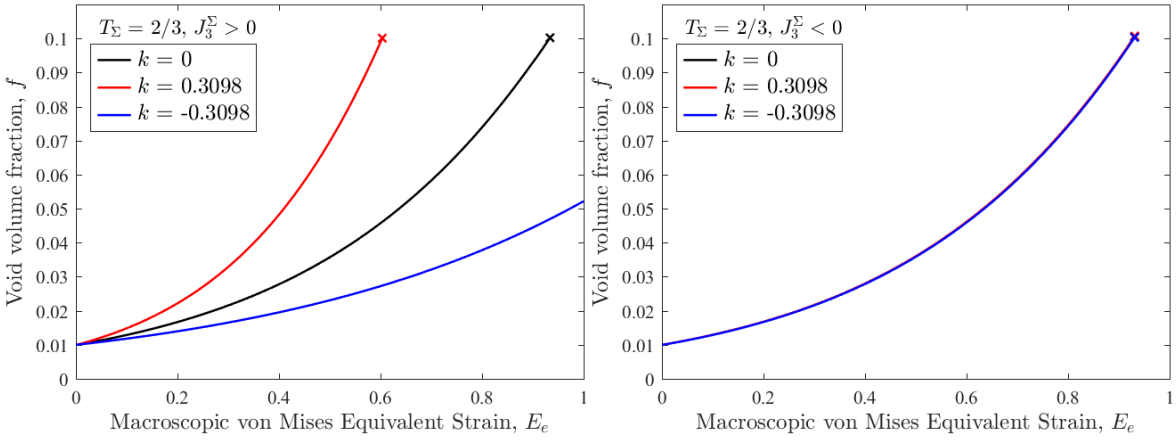

(a) (b)

Figure 5.3. Void volume fraction evolution for porous materials displaying distinct SD effects under axisymmetric tensile loadings corresponding to a stress triaxiality $T_\Sigma = 2/3$ and: (a) $J_3^\Sigma > 0$; (b) $J_3^\Sigma < 0$.

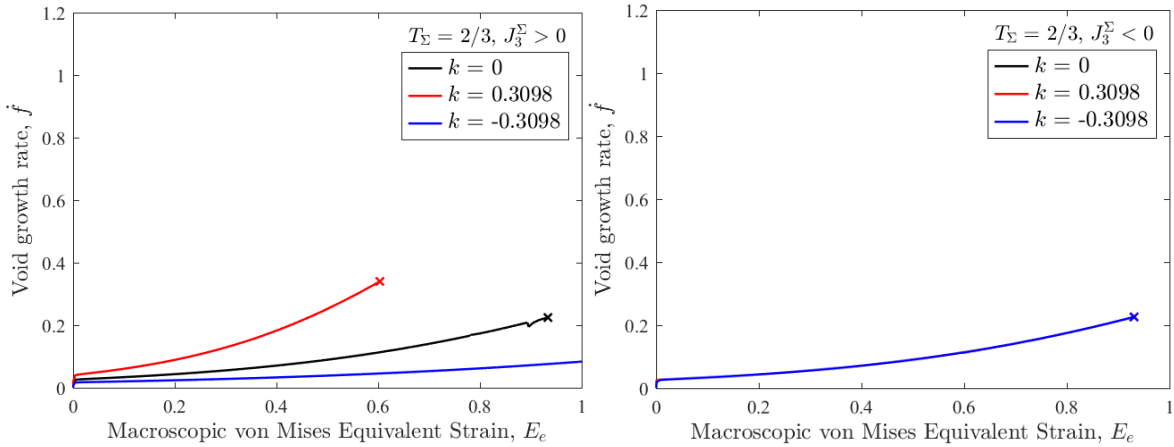

(a) (b)

Figure 5.4. Void growth rate evolution for porous materials displaying distinct SD effects under axisymmetric tensile loadings corresponding to a stress triaxiality $T_\Sigma = 2/3$ and: (a) $J_3^\Sigma > 0$; (b) $J_3^\Sigma < 0$.

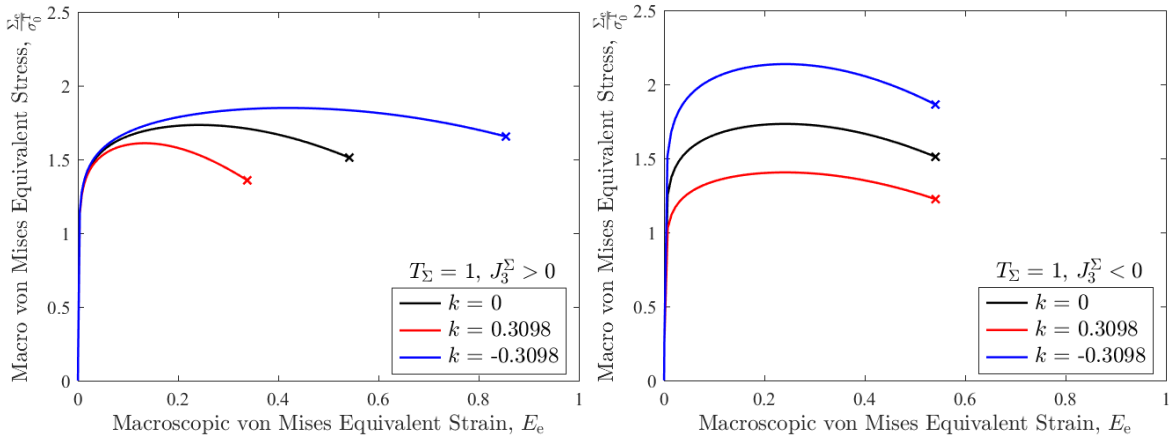

(a) (b)

Figure 5.5. Macroscopic stress–strain response for porous materials displaying distinct SD effects under axisymmetric tensile loadings corresponding to a stress triaxiality $T_\Sigma = 1$ and: (a) $J_3^\Sigma > 0$; (b) $J_3^\Sigma < 0$.

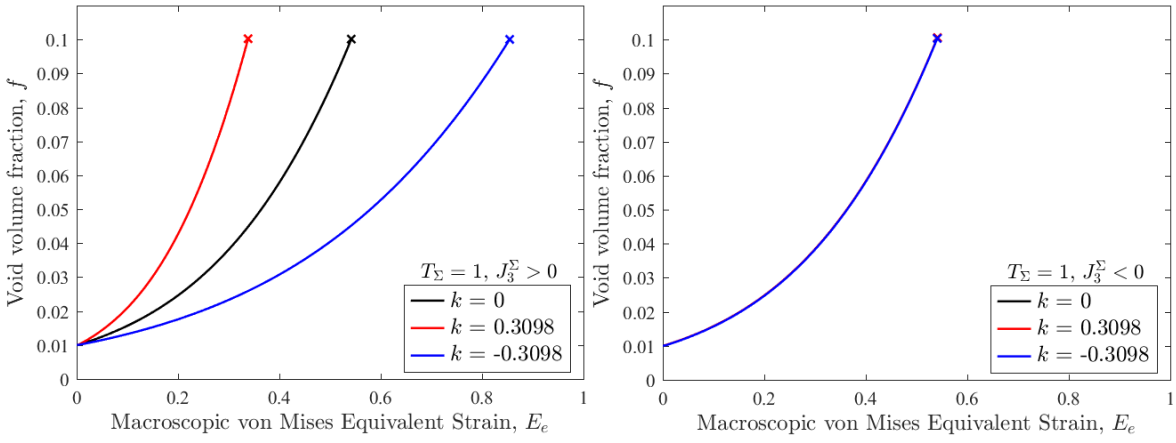

(a) (b)

Figure 5.6. Void volume fraction evolution for porous materials displaying distinct SD effects under axisymmetric tensile loadings corresponding to a stress triaxiality $T_\Sigma = 1$ and: (a) $J_3^\Sigma > 0$; (b) $J_3^\Sigma < 0$.

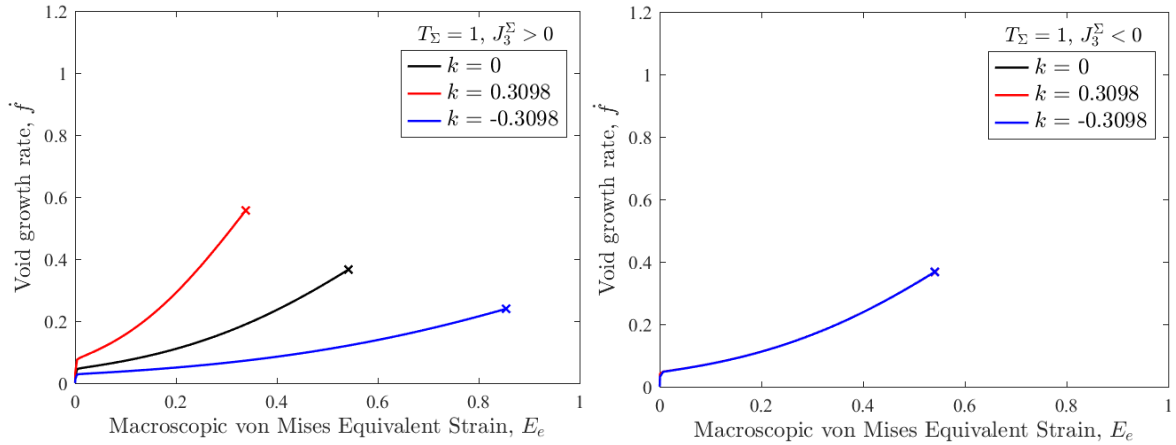

(a) (b)

Figure 5.7. Void growth rate evolution for porous materials displaying distinct SD effects under axisymmetric tensile loadings corresponding to a stress triaxiality $T_\Sigma = 1$ and: (a) $J_3^\Sigma > 0$; (b) $J_3^\Sigma < 0$.

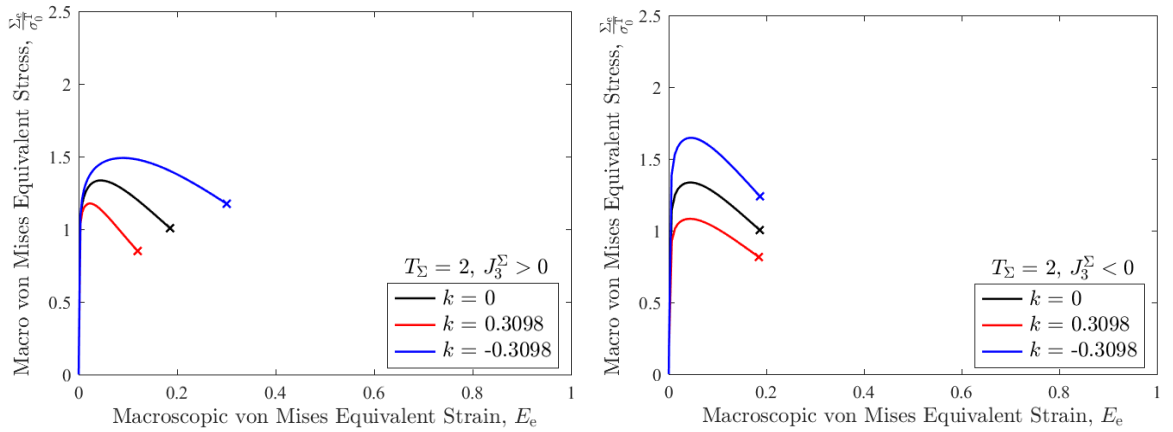

(a) (b)

Figure 5.8. Macroscopic stress–strain response for porous materials displaying distinct SD effects under axisymmetric tensile loadings corresponding to a stress triaxiality $T_\Sigma = 2$ and: (a) $J_3^\Sigma > 0$; (b) $J_3^\Sigma < 0$.

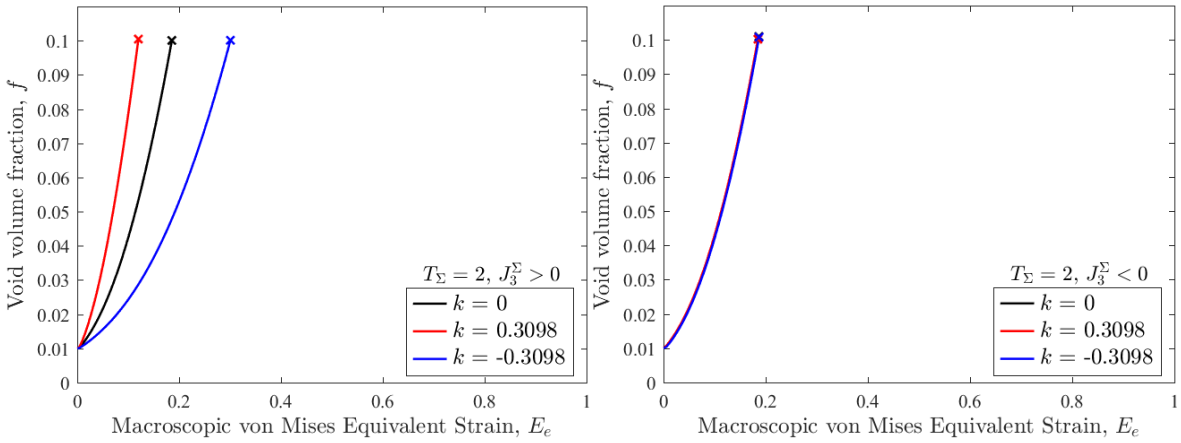

(a) (b)

Figure 5.9. Void volume fraction evolution for porous materials displaying distinct SD effects under axisymmetric tensile loadings corresponding to a stress triaxiality $T_\Sigma = 2$ and: (a) $J_3^\Sigma > 0$; (b) $J_3^\Sigma < 0$.

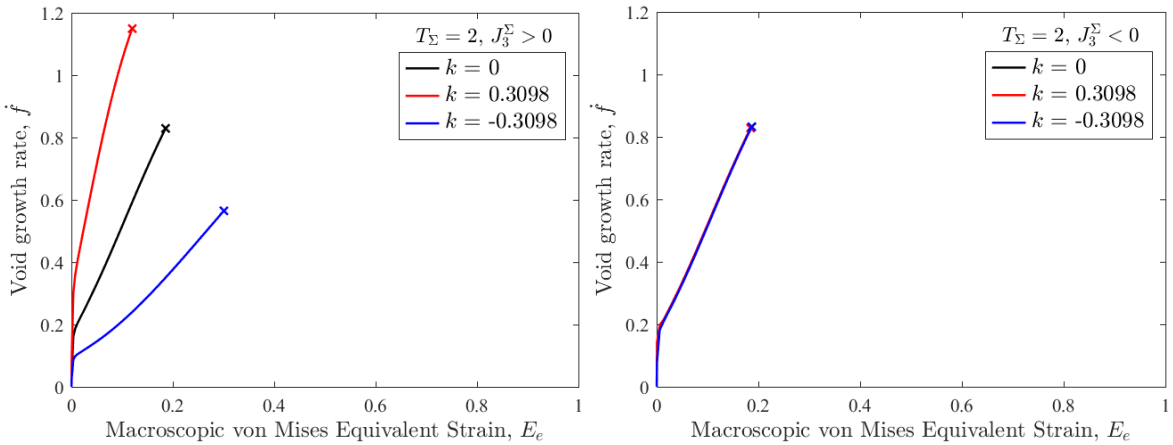

(a) (b)

Figure 5.10. Void growth rate evolution for porous materials displaying distinct SD effects under axisymmetric tensile loadings corresponding to a stress triaxiality $T_\Sigma = 2$ and: (a) $J_3^\Sigma > 0$; (b) $J_3^\Sigma < 0$.

5.2.2. Tensile and compressive hydrostatic loadings

The response of the CPB06 porous model for purely tensile and compressive hydrostatic loadings is also assessed. In this case, the prescribed constant $\rho = \Sigma_{33}/\Sigma_{11}$ becomes unitary and the hydrostatic stress states are solely distinguished by the sign of the imposed macroscopic stresses $(\Sigma_{11} = \Sigma_{22} = \Sigma_{33})$. Note that for hydrostatic loadings the stress triaxiality tends to infinity: $T_\Sigma \to \infty$ for the tensile loadings and $T_\Sigma \to -\infty$ for the compressive loadings. Moreover, for theses loadings the third invariant of the stress deviator tensor is null, $J_3^\Sigma = 0$, hence the Lode angle, θ_Σ, (and Lode parameter, $\overline{\theta}_\Sigma$) are undefined.

Figure 5.11 shows the comparison between the normalized macroscopic von Mises effective stress, Σ_e *versus* the macroscopic effective strain, E_e for the three porous solids, corresponding to the FE computations for the tensile and compressive hydrostatic loadings. For both cases, the void volume fraction evolution, f is illustrated in Figure 5.12 – void growth with hydrostatic tension and void collapse in the hydrostatic compression case. It should be noted that, given the characteristics of the hydrostatic loading responses, the above plots are represented only up to a macroscopic strain of $E_e = 0.05$, i.e. 5% of the limit value considered in the axisymmetric tensile loadings.

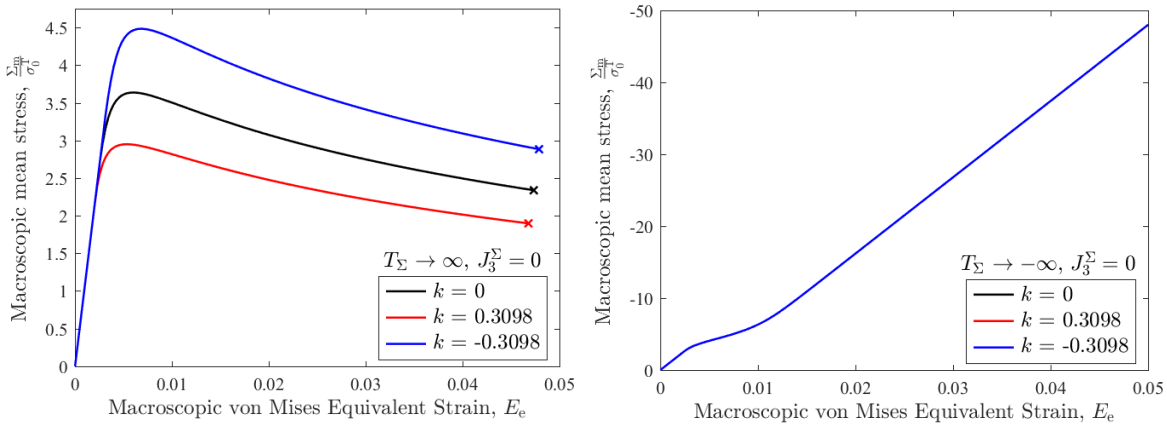

(a) (b)

Figure 5.11. Macroscopic stress–strain response for porous materials displaying distinct SD effects under: (a) tensile hydrostatic loading, $T_\Sigma \to \infty$; (b) compressive hydrostatic loading, $T_\Sigma \to -\infty$.

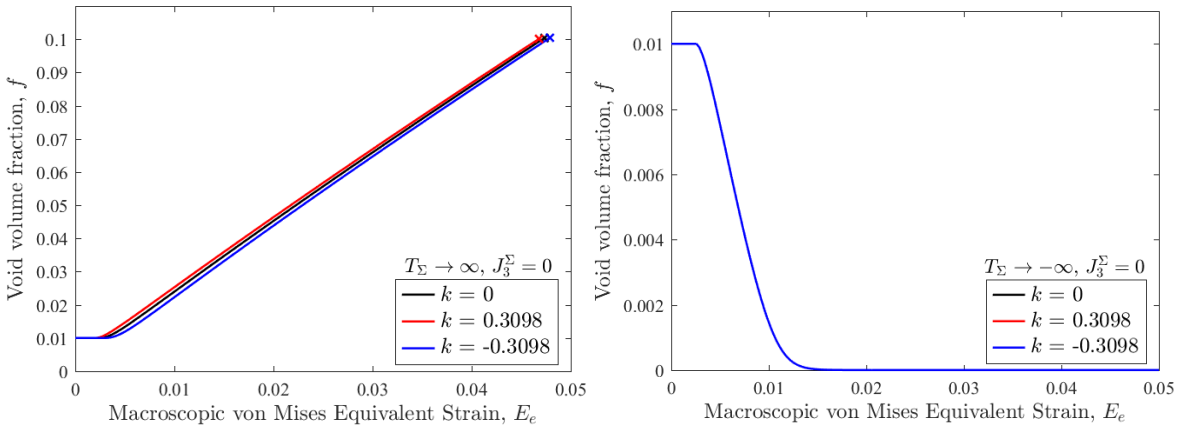

(a) (b)

Figure 5.12. Void volume fraction evolution for porous materials displaying distinct SD effects under: (a) tensile hydrostatic loading, $T_\Sigma \to \infty$; (b) compressive hydrostatic loading, $T_\Sigma \to -\infty$.

5.3. Discussion of the results

The numerical results obtained in the previous section are now discussed. A detailed analysis for the particular case of a stress triaxiality of $T_\Sigma = 2/3$ will be carried out. This stress triaxiality results from the well-known equibiaxial tension (EBT) stress state, which is of great practical importance in sheet metal forming, and is characterized by $\Sigma_{11} = \Sigma_{22}$ with $\Sigma_{33} = 0$ for which $J_3^\Sigma < 0$. As for the remaining axisymmetric loadings, the conclusions drawn from this case are equally applicable and therefore a brief discussion will be made solely on the effect of increasing the stress triaxiality, specifically on the damage accumulation, material ductility and on the impact of the SD effects of the matrix in the mechanical response of the porous solid.

Analysing Figure 5.2 it is clear that the SD effects (described by the parameter k), affect the mechanical response of the porous solids, namely the maximum von Mises effective stress, Σ_e and the softening behaviour of the porous solids. In the case $J_3^\Sigma > 0$, the different porosity evolutions clearly differentiate the onset of failure and, consequently, the maximum macroscopic strain, E_e that is reached – a good indicator of the materials ductility (or its formability). In addition to having the highest macroscopic effective stress throughout the entire deformation history, the material characterized by k = –0.3098 also exhibits the highest ductility for the evolution characterized by $J_3^\Sigma > 0$. In fact, although there is some softening effect on this material, the simulation ended without reaching the onset of the

coalescence. The same conclusion could be drawn from Figure 5.3. Indeed, the damage model predicts that, for axisymmetric loadings with $J_3^{\Sigma} > 0,$ the higher the SD ratio, (i.e. the higher the parameter *k*), the earlier the failure onset occurs. In other words, due to the slower void growth rate, $\dot{f}$ for $J_3^{\Sigma} > 0$ (see Figure 5.4) there is an *enhanced ductility* for porous solids with yield strength in tension lower than in compression, $k < 0.$ However, the damage model does not predict the same behaviour for the loading characterized by $J_3^{\Sigma} < 0.$ In this case, the void growth rate, represented in Figure 5.4 (b) is *insensitive to SD effects of the matrix* and, consequently, all three materials present the same evolution of the void volume fraction, equal to the one of the matrix, characterized by $k = 0$ (von Mises material). This means that, for evolutions with $J_3^{\Sigma} < 0,$ the onset of failure will always occur for the same macroscopic von Mises equivalent strain, E_{e} and, therefore, the tension-compression asymmetry will not affect the ductility of the porous material. Moreover, by presenting the same porosity evolution, the materials exhibit very similar softening behaviours (see Figure 5.2 (b)), contrasting with the numerical results obtained for the axisymmetric stress state with $J_3^{\Sigma} > 0$ (Figure 5.2 (a)).

Although for loadings with $J_3^{\Sigma} < 0$ the porosity evolution is insensitive to the tension-compression asymmetry of the matrix, the CPB06 damage model is able to account of the SD effects in the yielding of the porous solids. Indeed, the numerical results of the macroscopic von Mises equivalent stress evolution are in agreement with the specificities of the yield surface for axisymmetric states, represented in Figure 4.10. This figure shows that, for a given stress triaxiality, a distinct behaviour on yielding occurs for $J_3^{\Sigma} > 0$ and for $J_3^{\Sigma} < 0,$ as the SD effects are manifested very differently. In the particular case of $T_{\Sigma} = 2/3$ and for $J_3^{\Sigma} > 0,$ the curves denoting the yielding of each material for a particular void volume fraction value, f are practically coincident, whereas for $J_3^{\Sigma} < 0$ a clear differentiation in the yield locus of the materials is shown. Note also that, as the stress triaxiality increases, i.e. as the lines approach the hydrostatic axis, the differences in the yielding loci for $J_3^{\Sigma} > 0$ and $J_3^{\Sigma} < 0$ are reduced. This behaviour is well captured in the numerical simulations for $J_3^{\Sigma} > 0,$ in which a departure of the macroscopic equivalent stress curves from the one obtained with

the von Mises material ($k = 0$) is observed with the increase of the stress triaxiality value (see Figure 5.2 (a), Figure 5.5 (a) and Figure 5.8 (a)).

The behaviour predicted by the CPB06 porous model for axisymmetric loadings characterized by $J_3^{\Sigma} > 0$ seems to be in overall good agreement with FEA results obtained in detailed three-dimensional micromechanical studies through unit cells (e.g. the work of Alves & Cazacu (2015a); Alves et al. (2017)). However, the same studies reveal completely different findings for axisymmetric stress states characterized by $J_3^{\Sigma} < 0,$ when compared with the numerical results obtained in the present analysis. In the micromechanical unit cell simulations was concluded that, in the same way as in the $J_3^{\Sigma} > 0$ case, the damage accumulation (i.e. the void growth) for $J_3^{\Sigma} < 0$ is *strongly influenced by the SD effects of the matrix*. In this case, the material with the lowest SD ratio (i.e., lowest parameter *k*) will continue to present the highest macroscopic von Mises equivalent stress, Σ_e. However, and opposing to the $J_3^{\Sigma} > 0$ stress state, there will be an *enhanced ductility* for the porous solids with yield strength in tension greater than in compression, $k > 0.$

According to the cited micromechanical studies, the differences in the porosity evolution (and ultimately on the ductility of the porous materials) with the sign of J_3^{Σ} can be explained by the distribution and heterogeneity of the local plastic strains and local stresses that arise around the micro-voids then SD effects are displayed, which are markedly different than in a von Mises material. In these studies is also shown that, even if at the macroscopic level, i.e. $(\Sigma_{11}, \Sigma_{22}, \Sigma_{33}),$ there is a very small difference in the macroscopic stress–strain response of the materials, the differences in the local state fields, $(\sigma_{11}, \sigma_{22}, \sigma_{33}),$ are very strong. It should be also noted that in the present study it is considered that the onset of failure occurs in all materials for the same critical porosity value, i.e. it is independent of the SD effects displayed by the matrix. However, this assumption may not be accurate. In fact, unit cell computations show (through the inter-void spacing or the cell's cross section monitoring) that the onset of coalescence occurs for slightly different void volume fraction values in the porous solids exhibiting different SD effects (Alves & Cazacu, 2015b).

Being incapable of accounting for SD effects on the porosity evolution for loadings with $J_3^{\Sigma} < 0,$ the CPB06 damage model will also be unable to reproduce distinct softening behaviours, and ultimately fail to reliably predict the ductile fracture of the porous solids

displaying tension-compression asymmetry. Thus, the question arises as to why the damage model is insensitive to the SD effects in the void growth rate, $\dot{f}$ for, and only for, $J_3^{\Sigma} < 0$. Note that this particular stress state corresponds to the fourth quadrant of the axisymmetric projection in the space $(\Sigma_m, \Sigma_{11} - \Sigma_{33})$, represented in Figure 4.10. Analysing this quadrant it seems that the yielding curves are obtained through a *homothetic transformation*. Since the homothetic centre coincides with the origin of the coordinate system, the homothety is said to be a *uniform scaling*. Let *O* denote the origin of the $(\Sigma_m, \Sigma_{11} - \Sigma_{33})$ stress space and *P* an arbitrary point on the von Mises curve. The yield surfaces displaying SD effects can be obtained based on the von Mises curve $(k = 0)$, by the linear transformation:

$$\overrightarrow{OP} \mapsto t\ \overrightarrow{OP}, \tag{5.9}$$

where *t* is a *scale factor*, equal in all directions which, as will be shown below, is given by the ratio σ_C/σ_T. Being similar curves (in the geometric sense), the tangent to the points resulting from the intersection between the yield loci and the stress triaxiality lines are equal in all three materials. A more reasoned mathematical analysis is now presented in order to support these observations. In mathematics, a real valued function, $s : \mathbb{R} \to \mathbb{R}$ is said to be homogeneous of degree α if:

$$s(tx) = t^{\alpha} s(x), \quad \forall t > 0. \tag{5.10}$$

These functions are characterized by their multiplicative scaling behaviour – the *level sets* of a homogenous function are radial expansions and contractions of each other. Moreover, the tangent lines to the level sets of a homogeneous function, $s(x)$ along each ray extending from the origin have *constant slopes*. One can prove that the axisymmetric yield loci for $\Sigma_m > 0 \wedge J_3^{\Sigma} > 0$ is a homogenous function. Rearranging Equation (3.41), defined for $\Sigma_m > 0$, results:

$$\overline{\Sigma}_e = f\left(\overline{\Sigma}_m\right) \Leftrightarrow \overline{\Sigma}_e = -\left(\frac{\sigma_C}{\sigma_T}\right)\sqrt{1 + q_3 f^2 - 2q_1 f \cosh\left(\frac{3}{2} q_2 \left(\frac{\sigma_T}{\sigma_C}\right)\overline{\Sigma}_m\right)}, \tag{5.11}$$

where $\overline{\Sigma}_e = (\Sigma_{11} - \Sigma_{33})/\sigma_T$ is the normalized macroscopic von Mises equivalent stress and $\overline{\Sigma}_m = \Sigma_m/\sigma_T$ is the normalized macroscopic mean stress. For a von Mises material $(k = 0)$, i.e. for a unitary SD ratio, the previous expression resumes to the reference yield locus:

$$\overline{\Sigma}_e\big|_{k=0} = -\sqrt{1 + q_3 f^2 - 2q_1 f \cosh\left(\frac{3}{2} q_2 \overline{\Sigma}_m\right)}. \tag{5.12}$$

By multiplying the argument of $\overline{\Sigma}_{\mathrm{e}}$ in Equation (5.11) by the factor $(\sigma_{\mathrm{C}}/\sigma_{\mathrm{T}})$ results:

$$\overline{\Sigma}_{\mathrm{e}} = f\left(\left(\frac{\sigma_C}{\sigma_T}\right)\overline{\Sigma}_{\mathrm{m}}\right) \Leftrightarrow \overline{\Sigma}_{\mathrm{e}} = \left(\frac{\sigma_C}{\sigma_T}\right)\overline{\Sigma}_{\mathrm{e}}\Big|_{k=0}. \tag{5.13}$$

It follows that the yield loci in the fourth quadrant of Figure 4.10 is a homogenous function with a degree of homogeneity $\alpha = 1$, i.e. both the hydrostatic axis and the deviatoric axis are scaled linearly by the factor $\sigma_{\mathrm{C}}/\sigma_{\mathrm{T}}$. It is thus confirmed that for a given stress triaxiality, T_{Σ} the normal to the surfaces at the point of intersection is independent of the material parameter *k*. As a consequence, according to the normality principle, *the direction of the plastic strain increment is insensitive to SD effects*.

In order to comprehend the insensitivity of the void growth rate, $\dot{f}$ to the SD effects for tensile stress states with $J_3^{\Sigma} < 0,$ the damage evolution law for the opposite stress state, i.e. $J_3^{\Sigma} > 0,$ is firstly analysed. Recovering Equation (3.18), obtained from the mass conservation principle, and combining this expression with Equations (3.25), (3.32) and (3.39) results:

$$\dot{f}_{\mathrm{growth}}\Big|_{J_3^{\Sigma}>0,\ \Sigma_{\mathrm{m}}>0} = (1-f)D_{kk}^{\mathrm{p}} = (1-f)\dot{\lambda}\left(\frac{\sigma_{\mathrm{T}}}{\sigma_{\mathrm{C}}}\frac{3q_1q_2f}{\sigma_{\mathrm{T}}}\right)\sinh\left(\frac{3}{2}q_2\frac{\sigma_{\mathrm{T}}}{\sigma_{\mathrm{C}}}\frac{\tilde{\Sigma}_{\mathrm{e}}}{\sigma_{\mathrm{T}}}T_{\Sigma}\right), \tag{5.14}$$

where $\tilde{\Sigma}_{\mathrm{e}}$ is the macroscopic equivalent stress according to the CPB06 isotropic yield criterion. Figure 5.13 (a) represents with dash-dot lines the evolution of the local equivalent plastic strain of the matrix material, $\overline{\varepsilon}_{\mathrm{M}}^{\mathrm{p}}$ for a tensile axisymmetric loading with $J_3^{\Sigma} > 0$. In this case, it is shown that the magnitude of the plastic strain increment, quantified by the plastic multiplier, λ in Equation (5.14), is independent of SD effects. Furthermore, note the presence of the $\sigma_{\mathrm{T}}/\sigma_C$ ratio both on the argument of the hyperbolic sine and on its multiplying factors. This corroborates the distinct porosity evolutions obtained in the numerical tests (e.g. Figure 5.3 (a)), according to the *k* value. The evolution of the normalized CPB06 equivalent stress, $\tilde{\Sigma}_{\mathrm{e}}/\sigma_{\mathrm{T}},$ a parameter also present in the hyperbolic sine argument of Equation (5.14), is presented in Figure 5.13 (b). It is shown that, although for low values of the macroscopic strain, E_{e} the $\tilde{\Sigma}_{\mathrm{e}}/\sigma_{\mathrm{T}}$ curves are coincident, they diverge from the reference von Mises curve $(k = 0),$ due to the distinct damage evolutions (see Figure 5.3 (a)) and resultant softening behaviours.

Once recognized the source of the void growth rate sensitivity to the SD effects for tensile loadings with $J_3^{\Sigma} > 0$, the damage evolution law for $J_3^{\Sigma} < 0$ is now analysed. Rearranging Equation (3.18) and, as in the previous case, combining it with Equations (3.25), (3.32) and (3.39), yields:

$$\dot{f}_{\text{growth}}\Big|_{J_3^{\Sigma}<0,\ \Sigma_{\text{m}}>0} = (1-f)\,D_{kk}^{\text{p}} = (1-f)\,\dot{\lambda}\left(\frac{\sigma_{\text{T}}}{\sigma_{\text{C}}}\frac{3q_1q_2f}{\sigma_{\text{T}}}\right)\sinh\left(\frac{3}{2}q_2\frac{\tilde{\Sigma}_{\text{e}}}{\sigma_{\text{T}}}T_{\Sigma}\right), \qquad (5.15)$$

Note that, due to the axisymmetric stress state relationships (see Equation (3.39)), the $\sigma_{\text{T}}/\sigma_{\text{C}}$ ratio is no longer present in the argument of the hyperbolic sine. Furthermore, recall that due to the yield function homogeneity, the plastic strain increment has the same direction, as oppose to the $J_3^{\Sigma} > 0$ case. Nonetheless it is possible to show that the magnitude of this increment, quantified by the plastic multiplier, λ depends on the SD effects. This remark can be confirmed by the dash-dot lines represented in Figure 5.14 (a), showing the evolution of the local equivalent plastic strain, $\bar{\varepsilon}_{\text{M}}^{\text{p}}$ for a tensile axisymmetric loading with $J_3^{\Sigma} < 0$. It is confirmed that the evolutions corresponding to the solids exhibiting SD effects do not match with the von Mises curve, $(k = 0)$. Indeed, it can be shown that the former curves can be obtained based the von Mises reference curve by multiplying each point by the scaling factor $\sigma_{\text{C}}/\sigma_{\text{T}}$. As a result, it is concluded that the plastic multiplier, λ is responsible for implicitly eliminating the single scaling effect of the $\sigma_{\text{T}}/\sigma_{C}$ ratio present in the previous expression. This ultimately makes the void growth rate insensitive to the SD effects.

Figure 5.14 (a) shows the CPB06 equivalent stress evolutions for the studied porous materials. Note that, even displaying the same porosity evolution (see Figure 5.3 (b)), the distinct local equivalent plastic strain distribution that arise in the materials displaying SD effects for tensile loadings with $J_3^{\Sigma} < 0$ imply that the flow stress, σ_{T} and, as a result, the CPB06 equivalent stress, $\tilde{\Sigma}_{\text{e}}$ present different evolutions for the three solids. Even so, it should be noted that, if normalized by its current flow stress in tension, i.e. the ratio $\tilde{\Sigma}_{\text{e}}/\sigma_{\text{T}}$ (see Equation (5.15)), the normalized CPB06 equivalent stress presents the same evolution, regardless of the SD effects (see Figure 5.14 (b)).

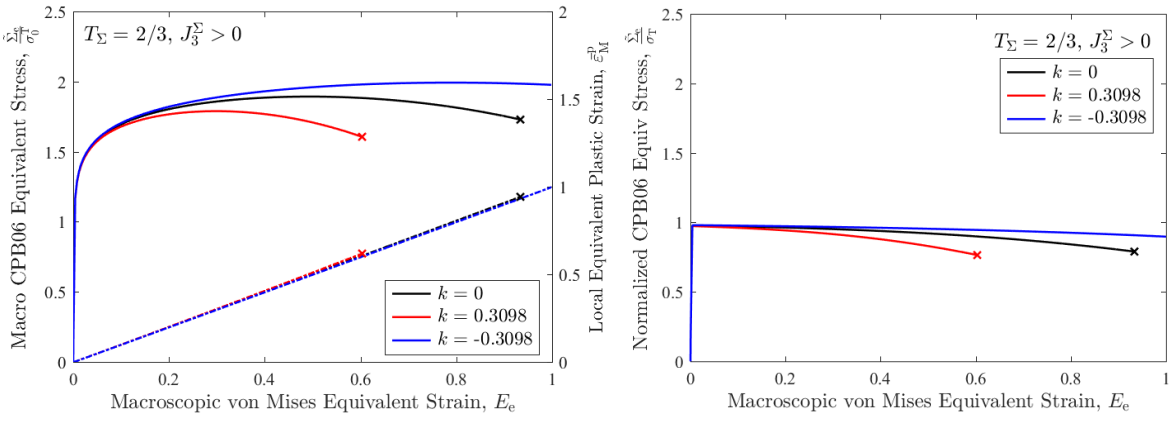

Figure 5.13. Macroscopic stress–strain responses for porous materials displaying distinct SD effects under axisymmetric tensile loadings corresponding to a stress triaxiality $T_\Sigma = 2/3$ and $J_3^\Sigma > 0$: (a) CPB06 equivalent stress and local equivalent plastic strain; (b) Normalized CPB06 equivalent stress.

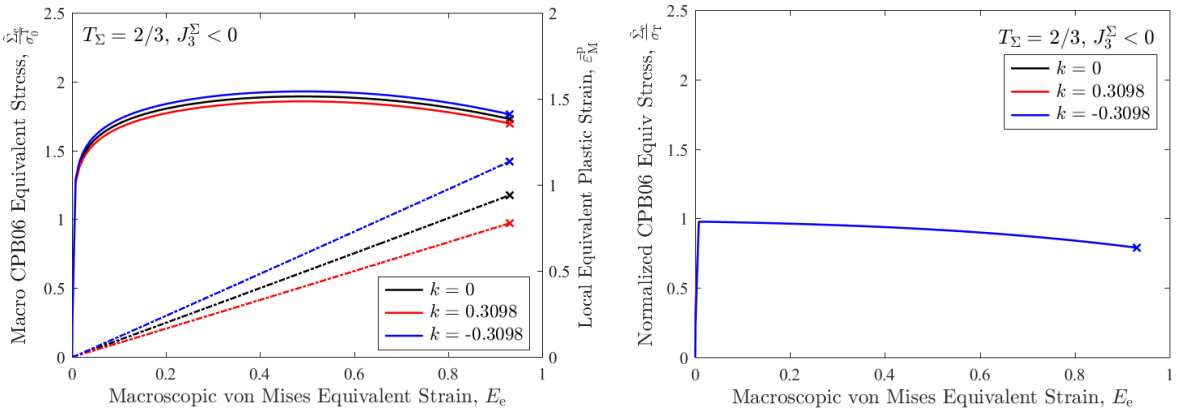

Figure 5.14. Macroscopic stress–strain responses for porous materials displaying distinct SD effects under axisymmetric tensile loadings corresponding to a stress triaxiality $T_\Sigma = 2/3$ and $J_3^\Sigma < 0$: (a) CPB06 equivalent stress and local equivalent plastic strain; (b) Normalized CPB06 equivalent stress.

So far, a detailed analysis of the tensile axisymmetric loading response at $T_\Sigma = 2/3$ was presented, which showed the strong coupling between the sign of the parameter k and the loading path, namely by the sign of J_3^Σ (or the Lode parameter value, $\bar{\theta}_\Sigma = \pm 1$) on the void growth rate, and ultimately on the porous solid ductility. The same conclusions hold true for the remaining stress triaxialities studied, viz. $T_\Sigma = 1$ and $T_\Sigma = 2$. In these cases, analysing Figure 5.5 and Figure 5.8, one can verify that with the increase of the stress triaxiality there is a decrease in the ductility of the porous solids. This behaviour is closely related to the higher void growth rate (see Figure 5.4, Figure 5.7 and Figure 5.10). This would be expected since the stress triaxiality value arises in the argument of the hyperbolic sine, as shown in Equation (5.14) (recall that the hyperbolic sine is a monotonic increasing

function). Furthermore, the increase of the stress triaxiality also causes an earlier triggering of the materials softening and, consequently, the macroscopic von Mises equivalent stresses reach their maximum values for smaller macroscopic equivalent strains. Note that the plastic deformation process of a porous solid involves two concurrent behaviours: the matrix hardening with the local equivalent plastic strain; and the porosity evolution with the macroscopic/volumetric dilatation of the aggregate. Regardless of the SD effects, since high levels of porosity are achieved faster at high stress triaxialities, the softening of the solid due to the increased porosity rapidly overcomes the hardening of the matrix, thereby reducing its ductility, i.e. the ability to undergo plastic deformation before final failure.

Concerning the influence of the SD effects on the response of the material, Figure 5.3 (a), Figure 5.6 (a) and Figure 5.9 (a) show that, with the increase of the stress triaxiality, the absolute difference between the evolutions of the void volume fraction for the studied values of the material parameter k decreases, i.e. the evolutions approximate the one of the von Mises material ($k = 0$). In fact, as a limit case, the SD effects do not manifest on the porosity evolution at $T_\Sigma \to \infty$ (tensile hydrostatic loading), represented in Figure 5.12 (a). In this case, the small differences in the porosity evolution are simply due to the distinct instants for which the materials enter the plastic regime (see Figure 4.10). This means that, as in numerical simulations for tensile axisymmetric loadings with $J_3^\Sigma < 0,$ the damage model predicts that the ductility of the three materials exhibiting different SD effects will be identical. Numerical observations through unit cell simulations need to be conducted in order to validate the predicted trends. Regarding the macroscopic stress-strain response of the tensile hydrostatic loading simulation (see Figure 5.11 (a)) once again it is noted the atypical result that the plastic flow occurs first in the material with yield strength in tension greater than in compression. Such behaviour contrasts with the response obtained for the compressive hydrostatic loading simulations, shown in Figure 5.11 (b). In this case, as expected (e.g. see Figure 4.10), the plastic flow is independent of the SD effects – yielding for compressive hydrostatic loading depends uniquely on the yield strength in tension, which is assumed to be equal in all three materials. Note also that the macroscopic stress-strain evolution for the compressive hydrostatic loading, $T_\Sigma \to -\infty,$ exhibits a completely different behaviour than the other curves analysed so far. Indeed, since the porous materials are subjected to a negative stress triaxiality loading the voids tend to collapse. This way, as shown in Figure 5.12 (b), as the porosity tends to zero, $f \to 0,$ the damage model loses its

sensitivity to the first invariant of the macroscopic stress tensor, I_1^{Σ}. In other words, the porous solids becomes incompressible and their yield surfaces become infinite along the hydrostatic axis. As a result, once the porosity vanishes, the plastic deformation halts and the stress-strain response becomes linear, respecting Hooke's law for continuous media.

5.4. Sensitivity analysis of the hardening law parameters

In this section a brief sensitivity analysis on the damage evolution and on the mechanical properties degradation of porous solids exhibiting SD effects is performed, taking into account the variation of the isotropic hardening law parameters, namely the Swift's law normalized hardening coefficient, K/σ_0^{T} and the hardening exponent, n (see Equation (5.8)).

The sensitivity analysis performed is mono-parametric, meaning that the variation of one parameter is achieved by fixing the other hardening parameter. Figure 5.15 shows the stress-strain curves obtained through Equation (5.8) for the porous solid matrix, representing the effect of the variation of each of the hardening parameters in the normalized matrix tensile flow stress, $\sigma_{\mathrm{T}}/\sigma_0^{\mathrm{T}}$.

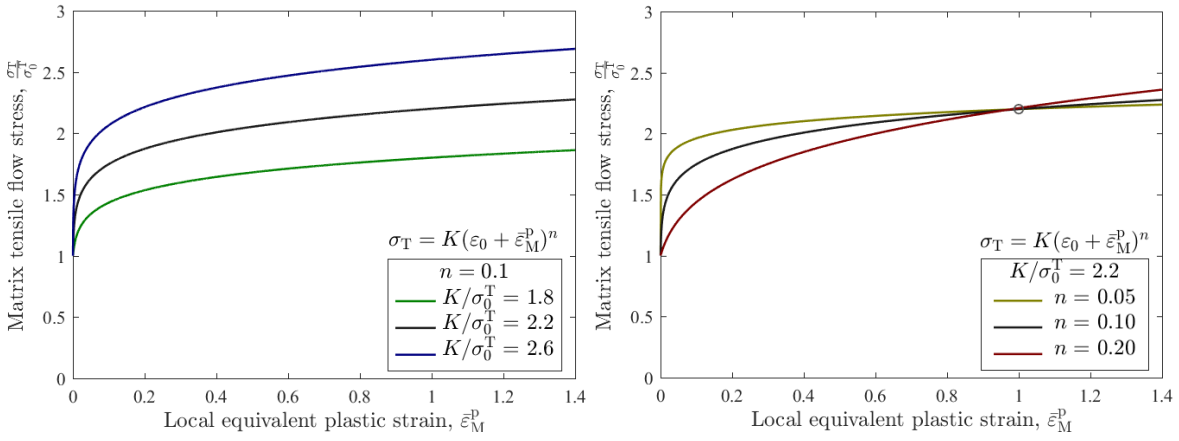

(a) (b)

Figure 5.15. Flow stress *versus* local equivalent plastic strain curves for the matrix material varying: (a) the hardening coefficient, K/σ_0^{T}; (b) the hardening exponent, n.

It can be verified that the nature of the evolution of the tensile flow stress, that is, the rate of hardening, is governed by the parameter n and the hardening coefficient, K/σ_0^{T}, which also acts as a scale factor. Note that for a fixed value of the hardening coefficient, (see

Figure 5.15 (b)), the material with the highest hardening exponent, *n*, presents the lowest matrix flow stress for a local equivalent plastic strain smaller than unity. Once this value is exceeded, this trend is inverted and the material with the highest hardening exponent takes the highest flow stress value. The opposite holds true for the material with the lowest hardening exponent. This behaviour indicates that the lower the hardening exponent, the earlier the hardening starts to occur, but, correspondingly, the earlier the hardening saturation will take place.

Figure 5.16 show a comparison of the normalized macroscopic von Mises effective stress, Σ_e/σ_0^T and the corresponding void volume fraction evolution, f evolutions for the three porous solids under an axisymmetric loading with $T_\Sigma = 1$ and $J_3^\Sigma > 0,$ when varying the hardening coefficient, K/σ_0^T. Figure 5.17 shows the same type of results obtained when varying the hardening exponent, *n*. In order to simplify the graphical analysis only two hardening parameter values are represented. The analysis is performed only for $J_3^\Sigma > 0$ since, as previously observed, there is a insensitivity to parameter *k* for $J_3^\Sigma < 0.$

The macroscopic stress-strain response of the materials when varying the parameter K/σ_0^T is very similar to the result observed in Figure 5.15 (a). It is shown that the variation of this parameter does not influences the ductility of the materials nor its softening behaviour. In summary, the hardening parameter K/σ_0^T acts simply as a scale factor, that is, the strength of the materials is changed but not its deformation history. Moreover, one can verify that neither the hardening coefficient, K/σ_0^T nor the hardening exponent, *n* influence the void volume fraction evolution, which are exactly coincident (see Figure 5.16 (b) and Figure 5.17 (b)). Note that the hardening law only dictates the way the yield locus expands, that is, the parameters defining the hardening law impact the size of the yield surface but not its shape. As seen in the previous chapter, for isotropic porous solids the shape of the yield surface is governed exclusively by the tension-compression asymmetry of the matrix. This implies that for a given stress state (T_Σ , $\overline{\theta}_\Sigma$) the normal to the yield locus and, consequently, the differences in the void grow rate are independent of the isotropic hardening law specificities.

Although no changes in ductility are observed, contrasting to the hardening coefficient, K/σ_0^T, the hardening exponent, *n*, of the Swift's law strongly effects the softening behaviour

of the materials. In this case, as shown in Figure 5.17 (a), a clear competition between the matrix hardening behaviour and the softening effects due to the increase of the porosity is observed. The combination of both phenomena describe the final response of the porous materials. For the materials with the lower hardening exponent, (n = 0.05), hardening starts to occur earlier. Thus, the corresponding stress-strain evolutions clearly present higher yield stress values than the curves referring to the higher hardening exponent, (n = 0.2), for low macroscopic equivalent strain values. However, hardening saturation will also occur firstly on the materials with the lowest hardening exponent n. Therefore, the softening caused by the increase of the porosity will cancel (and exceed) the hardening effects at lower values of the macroscopic equivalent strain. This means that the hardening exponent, n affects not only the maximum macroscopic von Mises yield stress in the stress-strain plots (quantifying the material's strength), but also the position, i.e. the value of the macroscopic equivalent strain, for which the maximum yield stress occurs. In short, for a fixed hardening coefficient, K/σ_0^{T}, the higher the hardening exponent, n, the later the maximum macroscopic yield stress will occur. Note that, it is expected that materials with a lower hardening exponent present the maximum equivalent yield stress. However, the ultimate yield strength – corresponding to the onset of failure (moment at which the critical void volume fraction is reached), of the materials with higher hardening exponents may surpass the ultimate yield strength of the ones with a lower hardening exponent. For instance, a similar ultimate yield strength can be observed in Figure 5.17 (a) for the materials with yield strength in tension lower than in compression (k = –0.3098).

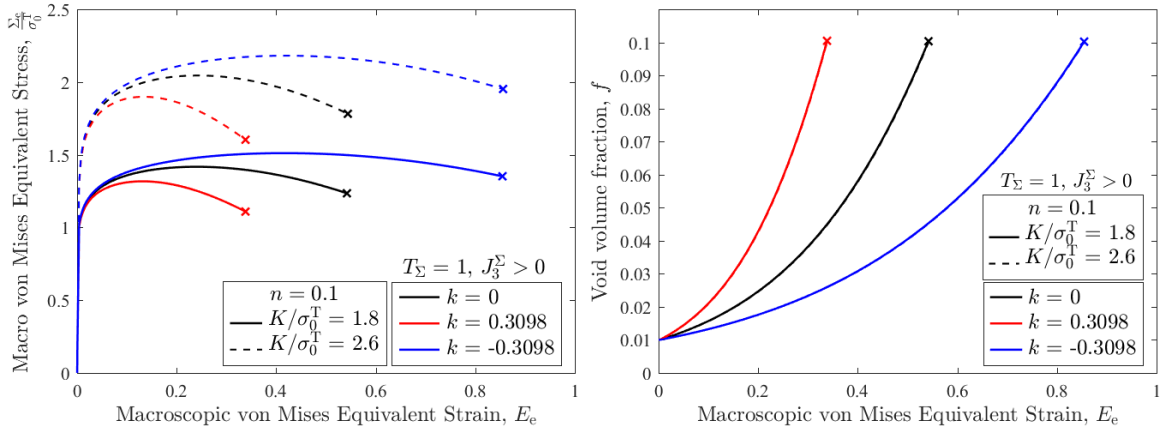

(a) (b)

Figure 5.16. Influence of the hardening coefficient, K/σ_0^{T} and the SD effects of the matrix, k on: (a) the macroscopic von Mises stress-strain evolutions; (b) the void volume fraction evolution, f.

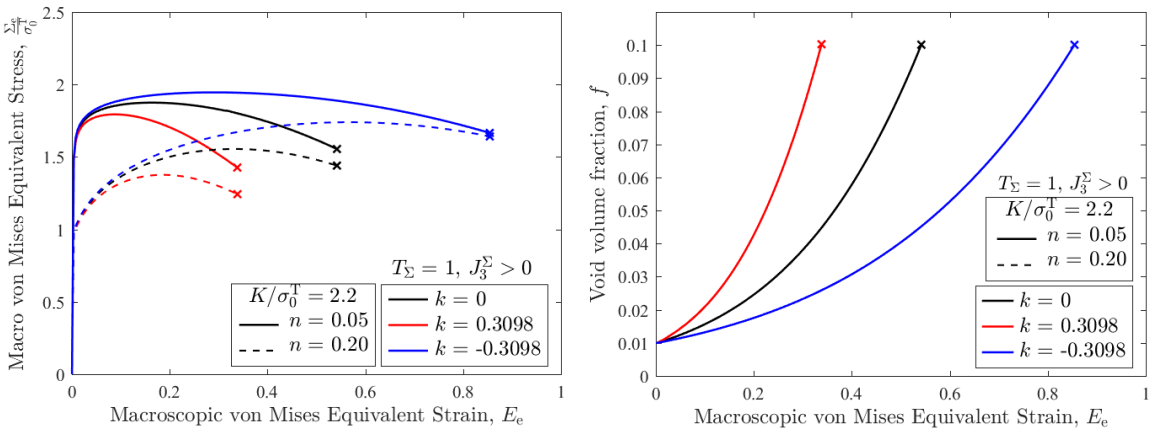

(a) (b)

Figure 5.17. Influence of the hardening exponent, n and the SD effects of the matrix, k on: (a) the macroscopic von Mises stress-strain evolutions; (b) the void volume fraction evolution, f.

6. Conclusions

In this work, the capability of the so-called isotropic CPB06 porous model – a coupled micromechanical-based damage model – to reliably describe the damage evolution and predict the ductile fracture of porous solids exhibiting tension-compression asymmetry was investigated. For this purpose, in an introductory way, a detailed sensitivity analysis of the damage model parameters was carried out, based on the yield loci change of shape and size with material, damage and stress state related parameters. An attempt was made to emphasise the importance of the role played by all stress invariants commonly used in the fracture mechanics framework, namely the J_3^{Σ} invariant for describing the SD effects and the I_1^{Σ} invariant to describe the effect of the mean stress. Next, a numerical analysis was conducted based on single-element tests, under macroscopic tensile axisymmetric loadings. The goal was to evaluate the predictive ability of the isotropic damage model by comparing the results with the behaviours predicted by documented and well-accepted micromechanical finite element computations on three-dimensional unit cells. The main conclusions of the investigations conducted within the context of this thesis are described below.

The sensitivity analysis to the yield surfaces of the CPB06 porous model performed in Chapter 4 led to the following key observations:

i. If SD effects are displayed, the yield locus is no longer symmetric with respect to the middle plane, $\Sigma_m = 0$. Moreover, it is shown that the SD effects only manifest in the definition of the upper vertex of the yield locus, i.e. the *tensile* hydrostatic yield strength and that, remarkably, the higher the yield strength in *compression*, the higher is this hydrostatic limit;

ii. The shape of the yield locus in the deviatoric plane of an isotropic porous solid is solely governed by the tension–compression asymmetry displayed by the matrix material, through the sign and magnitude of the material parameter *k*, since both the void volume fraction and the mean stress only influence the size of the yield contours in the π-plane projections;

iii. In the deviatoric projections at $\Sigma_m = 0$, the radial coordinate of the yield locus decreases linearly with increasing porosity, i.e. the yield locus sensitivity to the

porosity is *constant*. Contrasting, the sensitivity of the yield surface size along the hydrostatic axis is *inversely proportional* to the porosity value;

iv. The yield surfaces present their maximum radii along the deviatoric plane at $\Sigma_m = 0$ and the sensitivity of the yield loci to the mean stress *increases monotonically* towards either the tensile or compressive hydrostatic limits. Furthermore, the sensitivity to the mean stress increases with the increase of the porosity, i.e. the rate at which the projected area in the π-plane decreases with the absolute value of the mean stress;

Regarding the contents of Chapter 5, the single-element numerical tests under tensile axisymmetric loadings shown that:

i. For $J_3^{\Sigma} > 0$ the model clearly distinguish the influence of the tension-compression asymmetry on the porosity evolution and an *enhanced ductility* for porous solids with yield strength in tension lower than in compression, $k < 0,$ is observed;

ii. For $J_3^{\Sigma} < 0$ the model is unable to distinguish the influence of the tension-compression asymmetry on the porosity evolution, and thus, the predicted ductility of the porous solid is independent of the SD effects.

The predicted behaviour for loadings characterized by $J_3^{\Sigma} > 0$ is in overall good agreement with FEA three-dimensional micromechanical studies through unit cells, documented in the literature. However, the same studies reveal that, as for the $J_3^{\Sigma} > 0$ case, for loadings with $J_3^{\Sigma} < 0$ the porosity evolution should equally be influenced by the SD effects displayed by the matrix. Moreover, it would be expected that the porous solids with yield strength in tension greater than in compression, $k > 0,$ would display an enhanced ductility. Being incapable of accounting for SD effects on the porosity evolution for tensile loadings with $J_3^{\Sigma} < 0,$ the damage model is consequently unable to reproduce distinct softening behaviours and, ultimately, fails to reliably predict the ductile fracture onset of the porous solids displaying tension-compression asymmetry.

In order to understand the reason for the insensitivity of the damage model to SD effects for loadings with positive stress triaxialities and $J_3^{\Sigma} < 0,$ the yield loci projections on the axisymmetric plane were analysed. It was shown that in the quadrant of the stress space $(\Sigma_m, \Sigma_{11} - \Sigma_{33})$ correspondent to this loading type, the curves referring to several materials

exhibiting different SD effects are homothetic transformations of each other. Hence, the normal vector to the yield locus at the point resulting from the intersection with a given stress triaxiality is independent of the SD effects displayed by the matrix. Following the normality principle, it was proven that the direction of the plastic strain increment in this quadrant would be insensitive to SD effects. However, its magnitude is responsible for implicitly eliminating the single scaling effect of the σ_T/σ_C ratio present in the void growth rate function. Note that the damage evolution insensitivity to the SD effects occurs only for axisymmetric loadings with $J_3^{\Sigma} < 0$ *and* $\Sigma_m > 0$; indeed, although no compressive axisymmetric stress states have been studied, for negative triaxiality with $J_3^{\Sigma} < 0$ the damage model recovers its sensitivity to SD effects in the porosity evolution.

Concerning the effect of the stress triaxiality in the response of the porous aggregates, it was confirmed that, regardless of the SD effects, with the increase of the stress triaxiality the damage model predicts a decrease in the ductility of the solids – consequence of the higher void growth rate. Furthermore, it was shown that as the stress triaxiality tends to infinity the influence of the SD effects on the damage evolution (noticeable for $J_3^{\Sigma} > 0$) decreases, i.e. the porosity evolutions approximate to the curve referring to the von Mises material, $(k = 0)$.

Finally, the sensitivity analysis regarding the Swift's hardening law parameters on the damage evolution and plastic flow of the porous solids exhibiting SD effects shown that, as expected, neither the hardening coefficient, *K*, nor the hardening exponent, *n* influence the void volume fraction evolution, and, in the end, the ductility of the materials. This is related to the fact that the hardening of the matrix impacts the size of the yield surface but not its shape and, consequently, the plastic flow direction. Furthermore, only the hardening exponent, *n* appears to impact the softening behaviour of the materials, as both the maximum macroscopic equivalent stress and the macroscopic equivalent strain at which it occurs are shifted. In fact, it was concluded that for a fixed hardening coefficient, *K*, the higher the hardening exponent, *n*, the later the maximum macroscopic yield stress occurs.

The preliminary study on the shape and size of the yield loci relative to the void volume fraction and the stress state revelled to be essential to understand the results obtained in the elementary tests analysis. This study highlighted the importance of the yield loci shape, through the role played by all stress invariants, on the direction of the plastic strain

increments, and consequently on the void growth rate, i.e. damage evolution. It was concluded that the application of the CPB06 porous model for tensile loadings with $J_3^{\Sigma} < 0$ should be used with caution, since, in its current form, this coupled damage criterion is incapable of accurately describe the softening effects and, therefore, the fracture initiation of ductile materials displaying SD effects.

Note that, as in Gurson-like criteria, the present model is not suitable for the fracture prediction under shear-dominated loadings, as the J_3^{Σ}- dependency of the model was introduced to model the SD effects of the matrix and not to model the void distortion and void sheet coalescence mechanisms, active at low stress triaxiality. In future research, it would be interesting to extend the CPB06 damage model to incorporate the void shearing damage effects. This could be performed in a similar manner to how Gurson's (1977) criteria has been extended, meaning that the same approach can be used to include also strain-rate dependency and temperature sensitivity. Another interesting topic for future work would be to perform a sensitivity analysis including the matrix anisotropic behaviour. The numerical tools developed within this work are equally prepared to study this sounder case. Such analysis involves a higher number of interdepend coefficients, hence the knowledge acquired for the isotropic case, i.e. the developed *know-how*, will prove to be an excellent basis for the study of this more complex case.

Bibliography

Alves, J. L., & Cazacu, O. (2015a). Correlation between strength differential effects in the plastic flow of the matrix and the rate of damage growth in porous polycrystals. *Comptes Rendus - Mecanique*, *343*(2), 107–120. https://doi.org/10.1016/j.crme.2014.12.002

Alves, J. L., & Cazacu, O. (2015b). Micromechanical study of the dilatational response of porous solids with pressure-insensitive matrix displaying tension-compression asymmetry. *European Journal of Mechanics, A/Solids*, *51*, 44–54. https://doi.org/10.1016/j.euromechsol.2014.11.010

Alves, J. L., Oliveira, M. C., Menezes, L. F., & Cazacu, O. (2017). The role of tension-compression asymmetry of the plastic flow on ductility and damage accumulation of porous polycrystals. *Ciencia e Tecnologia Dos Materiais*, *29*(1), e234–e238. https://doi.org/10.1016/j.ctmat.2016.06.006

Alves, J. L., Revil-Baudard, B., & Cazacu, O. (2014). Importance of the coupling between the sign of the mean stress and the third invariant on the rate of void growth and collapse in porous solids with a von Mises matrix. *Modelling and Simulation in Materials Science and Engineering*, *22*(2). https://doi.org/10.1088/0965-0393/22/2/025005

Argon, A. S., Im, J., & Safoglu, R. (1975). Cavity formation from inclusions in ductile fracture. *Metallurgical Transactions A*, *6*(4), 825. https://doi.org/10.1007/BF02672306

Ayada, M. (1987). Central bursting in extrusion of inhomogeneous materials. In *Proceedings of 2nd International Conference on Technology for Plasticity, Stuttgart, 1987* (Vol. 1, pp. 553–558).

Babout, L., Maire, E., Buffière, J.-Y., & Fougeres, R. (2001). Characterization by X-ray computed tomography of decohesion, porosity growth and coalescence in model metal matrix composites. *Acta Materialia*, *49*(11), 2055–2063.

Badreddine, H., Labergère, C., & Saanouni, K. (2016). *Ductile damage prediction in sheet and bulk metal forming*. *Comptes Rendus - Mecanique*.

https://doi.org/10.1016/j.crme.2015.11.006

Bao, Y. (2003). *Prediction of ductile crack formation in uncracked bodies*. *PhD Thesis*. PhD Thesis, Department of Ocean Engineering, Massachusetts Institute of Technology. Retrieved from http://18.7.29.232/handle/1721.1/17634

Barlat, F., Aretz, H., Yoon, J. W., Karabin, M. E., Brem, J. C., & Dick, R. E. (2005). Linear transfomation-based anisotropic yield functions. *International Journal of Plasticity*, *21*(5), 1009–1039. https://doi.org/10.1016/j.ijplas.2004.06.004

Barros, P. D., Alves, J. L., Oliveira, M. C., & Menezes, L. F. (2016). Modeling of tension-compression asymmetry and orthotropy on metallic materials: Numerical implementation and validation. *International Journal of Mechanical Sciences*, *114*, 217–232. https://doi.org/10.1016/j.ijmecsci.2016.05.020

Benseddiq, N., & Imad, A. (2008). A ductile fracture analysis using a local damage model. *International Journal of Pressure Vessels and Piping*, *85*(4), 219–227. https://doi.org/10.1016/j.ijpvp.2007.09.003

Benzerga, A. A., & Besson, J. (2001). Plastic potentials for anisotropic porous solids. *European Journal of Mechanics, A/Solids*, *20*(3), 397–434. https://doi.org/10.1016/S0997-7538(01)01147-0

Benzerga, A. A., Besson, J., & Pineau, A. (2004a). Anisotropic ductile fracture, part II. theory. *Acta Materialia*, *52*, 4639–4650. https://doi.org/10.1016/j.actamat.2004.06.019

Benzerga, A. A., Besson, J., & Pineau, A. (2004b). Anisotropic ductile fracture: Part I: experiments. *Acta Materialia*, *52*(15), 4623–4638. https://doi.org/https://doi.org/10.1016/j.actamat.2004.06.020

Besson, J. (2010). *Continuum models of ductile fracture: A review*. *International Journal of Damage Mechanics* (Vol. 19). https://doi.org/10.1177/1056789509103482

Besson, J., & Guillemer-Neel, C. (2003). *An extension of the Green and Gurson models to kinematic hardening*. *Mechanics of Materials* (Vol. 35). https://doi.org/10.1016/S0167-6636(02)00169-2

Cazacu, O., Plunkett, B., & Barlat, F. (2006). Orthotropic yield criterion for hexagonal closed packed metals. *International Journal of Plasticity*, *22*(7), 1171–1194. https://doi.org/10.1016/j.ijplas.2005.06.001

Cazacu, O., Revil-Baudard, B., Lebensohn, R. A., & Gărăjeu, M. (2013). On the Combined

Effect of Pressure and Third Invariant on Yielding of Porous Solids With von Mises Matrix. *Journal of Applied Mechanics*, *80*(6), 64501–64505. Retrieved from http://dx.doi.org/10.1115/1.4024074

Cazacu, O., & Stewart, J. B. (2009). Analytic plastic potential for porous aggregates with matrix exhibiting tension-compression asymmetry. *Journal of the Mechanics and Physics of Solids*, *57*(2), 325–341. https://doi.org/10.1016/j.jmps.2008.10.010

Chaboche, J. L., Boudifa, M., & Saanouni, K. (2006). A CDM approach of ductile damage with plastic compressibility. *International Journal of Fracture*, *137*(1–4), 51–75. https://doi.org/10.1007/s10704-005-3061-5

Chu, C. C., & Needleman, A. (1980). Void Nucleation Effects in Biaxially Stretched Sheets. *Journal of Engineering Materials and Technology*, *102*(3), 249–256. Retrieved from http://dx.doi.org/10.1115/1.3224807

Cockcroft, M. G., & Latham, D. J. (1968). Ductility and the workability of metals. *J Inst Metals*, *96*(1), 33–39.

Dunand, M. (2013). *Ductile fracture at intermediate stress triaxialities: Experimental investigations and micro-mechanical modeling*. *Massachusetts Institute of Technology*. PhD Theis, Department of Mechanical Engineering, Massachusetts Institute of Technology.

Dunand, M., & Mohr, D. (2011). On the predictive capabilities of the shear modified Gurson and the modified Mohr-Coulomb fracture models over a wide range of stress triaxialities and Lode angles. *Journal of the Mechanics and Physics of Solids*, *59*(7), 1374–1394. https://doi.org/10.1016/j.jmps.2011.04.006

Faleskog, J., Gao, X., & Shih, C. F. (1998). Cell model for nonlinear fracture analysis–I. Micromechanics calibration. *International Journal of Fracture*, *89*(4), 355–373.

Gologanu, M., Leblond, J.-B., & Devaux, J. (1993). Approximate models for ductile metals containing non-spherical voids—Case of axisymmetric prolate ellipsoidal cavities. *Journal of the Mechanics and Physics of Solids*, *41*(11), 1723–1754. https://doi.org/https://doi.org/10.1016/0022-5096(93)90029-F

Gurson, A. L. (1975). *Plastic Flow and Fracture Behavior of Ductile Materials Incorporating Void Nucleation, Growth, and Interaction*. Retrieved from https://books.google.pt/books?id=xtrnHgAACAAJ

Gurson, A. L. (1977). Continuum Theory of Ductile Rupture by Void Nucleation and

Growth: Part I—Yield Criteria and Flow Rules for Porous Ductile Media. *Journal of Engineering Materials and Technology*, *99*(1), 2–15. Retrieved from http://dx.doi.org/10.1115/1.3443401

Hammi, Y., & Horstemeyer, M. F. (2007). A physically motivated anisotropic tensorial representation of damage with separate functions for void nucleation, growth, and coalescence. *International Journal of Plasticity*, *23*(10–11), 1641–1678. https://doi.org/10.1016/j.ijplas.2007.03.010

Hill, R. (1967). The essential structure of constitutive laws for metal composites and polycrystals. *Journal of the Mechanics and Physics of Solids*, *15*(2), 79–95. https://doi.org/https://doi.org/10.1016/0022-5096(67)90018-X

Hosford, W. ~F., & Allen, T. ~J. (1973). Twinning and directional slip as a cause for a strength differential effect. *Metallurgical Transactions*, *4*, 1424–1425. https://doi.org/10.1007BF02644545

Keeler, S., Kimchi, M., KUZIAK, R., KAWALLA, R., WAENGLER, S., & Yuqing Weng, Han Dong, Y. G. (2014). Advanced high strength steels for automotive industry. *Archives of Civil and Mechanical Engineering*, *8*(2), 511. https://doi.org/10.1016/S1644-9665(12)60197-6

Kiran, R., & Khandelwal, K. (2014). Gurson model parameters for ductile fracture simulation in ASTM A992 steels. *Fatigue and Fracture of Engineering Materials and Structures*, *37*(2), 171–183. https://doi.org/10.1111/ffe.12097

Lebensohn, R. A., & Cazacu, O. (2012). Effect of single-crystal plastic deformation mechanisms on the dilatational plastic response of porous polycrystals. *International Journal of Solids and Structures*, *49*(26), 3838–3852. https://doi.org/10.1016/j.ijsolstr.2012.08.019

Lemaitre, J. (1984). How to use damage mechanics. *Nuclear Engineering and Design*, *80*(2), 233–245.

Li, H., Fu, M. W., Lu, J., & Yang, H. (2011). Ductile fracture: Experiments and computations. *International Journal of Plasticity*, *27*(2), 147–180. https://doi.org/10.1016/j.ijplas.2010.04.001

Li, Y., & Karr, D. G. (2009). Prediction of ductile fracture in tension by bifurcation, localization, and imperfection analyses. *International Journal of Plasticity*, *25*(6), 1128–1153.

Liao, K. C., Pan, J., & Tang, S. C. (1997). Approximate yield criteria for anisotropic porous ductile sheet metals. *Mechanics of Materials*, *26*(4), 213–226. https://doi.org/10.1016/S0167-6636(97)00033-1

Malcher, L. (2012). *Continuum Modelling and Numerical Simulation of Damage for Ductile Materials*. PhD Thesis, Department of Mechanical Engineering, Faculty of Engineering, University of Porto.

Mandel, J., & Sciences., I. C. for M. (1972). *Plasticite classique et viscoplasticite*. Wien: Springer.

Marcadet, S. (2015). *Signature redacted Signature redacted Signature redacted Signature redacted*. PhD Thesis, Department of Mechanical Engineering, Massachusetts Institute of Technology.

McClintock, F. ~A. (1968). A Criterion for Ductile Fracture by the Growth of Holes. *Journal of Applied Mechanics*, *35*, 363. https://doi.org/10.1115/1.3601204

Menezes, L. F., & Teodosiu, C. (2000). Three-dimensional numerical simulation of the deep-drawing process using solid finite elements. *Journal of Materials Processing Technology*, *97*(1), 100–106. https://doi.org/https://doi.org/10.1016/S0924-0136(99)00345-3

Nahshon, K., & Hutchinson, J. W. (2008). Modification of the Gurson Model for shear failure. *European Journal of Mechanics, A/Solids*, *27*(1), 1–17. https://doi.org/10.1016/j.euromechsol.2007.08.002

Oliveira, M. C., Alves, J. L., & Menezes, L. F. (2008). Algorithms and Strategies for Treatment of Large Deformation Frictional Contact in the Numerical Simulation of Deep Drawing Process. *Archives of Computational Methods in Engineering*, *15*(2), 113–162. https://doi.org/10.1007/s11831-008-9018-x

Pack, K. (2017). *Signature redacted Signature redacted Thesis supervisor Signature redacted*. PhD Thesis, Department of Mechanical Engineering, Massachusetts Institute of Technology.

Perrin, G., & Leblond, J. B. (1990). Analytical study of a hollow sphere made of plastic porous material and subjected to hydrostatic tension-application to some problems in ductile fracture of metals. *International Journal of Plasticity*, *6*(6), 677–699.

Revil-Baudard, B., Cazacu, O., Flater, P., Chandola, N., & Alves, J. L. (2016). Unusual plastic deformation and damage features in titanium: Experimental tests and

constitutive modeling. *Journal of the Mechanics and Physics of Solids*, *88*, 100–122. https://doi.org/10.1016/j.jmps.2016.01.003

Rice, J. R., & Tracey, D. M. (1969). On the ductile enlargement of voids in triaxial stress fields∗. *Journal of the Mechanics and Physics of Solids*, *17*(3), 201–217.

Roll, K. (2008). Simulation of sheet metal forming - Necessary developments in the future. *Numisheet 2008*, (September), 59–68.

Rousselier, G. (1987). Ductile fracture models and their potential in local approach of fracture. *Nuclear Engineering and Design*, *105*(1), 97–111. https://doi.org/https://doi.org/10.1016/0029-5493(87)90234-2

Sá, R. A. and P. T. and E. A. and A. D. S. and J. C. de. (2016). A study on the performance of ductile failure models under different range of stress triaxiality states with experimental validation. *Journal of Physics: Conference Series*, *734*(3), 32122. Retrieved from http://stacks.iop.org/1742-6596/734/i=3/a=032122

Stewart, J. B. (2009). *Development of Yield Criteria for Describing the Behavior of*. PhD Thesis, University of Florida.

Stewart, J. B., & Cazacu, O. (2011). Analytical yield criterion for an anisotropic material containing spherical voids and exhibiting tension-compression asymmetry. *International Journal of Solids and Structures*, *48*(2), 357–373. https://doi.org/10.1016/j.ijsolstr.2010.10.009

Tvergaard, V. (1981). Influence of voids on shear band instabilities under plane strain conditions. *International Journal of Fracture*, *17*(4), 389–407.

Tvergaard, V. (1982). On localization in ductile materials containing spherical voids. *International Journal of Fracture*, *18*(4), 237–252.

Tvergaard, V., & Needleman, A. (1984). Analysis of the cup-cone fracture in a round tensile bar. *Acta Metallurgica*, *32*(1), 157–169.

Weck, A., Wilkinson, D. S., Toda, H., & Maire, E. (2006). 2D and 3D visualization of ductile fracture. *Advanced Engineering Materials*, *8*(6), 469–472.

Wierzbicki, T., Bao, Y., Lee, Y.-W., & Bai, Y. (2005). Calibration and evaluation of seven fracture models. *International Journal of Mechanical Sciences*, *47*(4–5), 719–743.

Xue, L. (2007). *Ductile Fracture Modeling - Theory , Experimental Investigation and Numerical Verification*. *Computer*. PhD. Thesis, Massachusetts Institute of Technology.

Xue, L. (2008). Constitutive modeling of void shearing effect in ductile fracture of porous materials. *Engineering Fracture Mechanics*, *75*(11), 3343–3366. https://doi.org/10.1016/j.engfracmech.2007.07.022

Xue, Z., Pontin, M. G., Zok, F. W., & Hutchinson, J. W. (2010). Calibration procedures for a computational model of ductile fracture. *Engineering Fracture Mechanics*, *77*(3), 492–509. https://doi.org/10.1016/j.engfracmech.2009.10.007

Yang, D. Y., Ahn, D. G., Lee, C. H., Park, C. H., & Kim, T. J. (2002). Integration of CAD/CAM/CAE/RP for the development of metal forming process. *Journal of Materials Processing Technology*, *125–126*, 26–34. https://doi.org/10.1016/S0924-0136(02)00414-4

Yoon, J. H., Stewart, J. B., & Cazacu, O. (2011). Coupled elastic-plastic damage model for a porous aggregate with an incompressible matrix displaying tension-compression asymmetry. *Engineering Fracture Mechanics*, *78*(7), 1407–1423. https://doi.org/10.1016/j.engfracmech.2011.03.003

Annex A – Determination of the Principal Values of the Transformed Stress Tensor

Let $\hat{\boldsymbol{\Sigma}}$ be the transformed stress tensor such that:

$$\hat{\boldsymbol{\Sigma}} = \begin{bmatrix} \hat{\Sigma}_{11} & \hat{\Sigma}_{12} & \hat{\Sigma}_{13} \\ \hat{\Sigma}_{12} & \hat{\Sigma}_{22} & \hat{\Sigma}_{23} \\ \hat{\Sigma}_{13} & \hat{\Sigma}_{23} & \hat{\Sigma}_{33} \end{bmatrix}, \tag{A.1}$$

with $(\mathbf{e}_1, \mathbf{e}_2, \mathbf{e}_3)$ denoting an orthogonal frame attached to the material (i.e. sheet rolling, transverse and normal directions, respectively). The principal values of the transformed stress tensor, $\hat{\Sigma}$ are the roots of the characteristic equation:

$$\det\left(\hat{\boldsymbol{\Sigma}} - \hat{\Sigma}\mathbf{I}\right) = 0, \tag{A.2}$$

whit **I** being the second-order identity tensor, which yields:

$$\hat{\Sigma}^3 - H_1\hat{\Sigma}^2 - 3H_2\hat{\Sigma} - 2H_3 = 0, \tag{A.3}$$

where H_1, H_2 and H_3 are the first, second and third invariants of $\hat{\boldsymbol{\Sigma}}$, which are given as:

$$H_1 = \frac{1}{3}\hat{I}_1 = \frac{1}{3}\left(\hat{\Sigma}_{11} + \hat{\Sigma}_{22} + \hat{\Sigma}_{33}\right), \tag{A.4}$$

$$H_2 = \frac{1}{3}\hat{I}_2 = \frac{1}{3}\left(\hat{\Sigma}_{23}{}^2 + \hat{\Sigma}_{13}{}^2 + \hat{\Sigma}_{12}{}^2 - \hat{\Sigma}_{22}\hat{\Sigma}_{33} - \hat{\Sigma}_{33}\hat{\Sigma}_{11} - \hat{\Sigma}_{11}\hat{\Sigma}_{22}\right), \tag{A.5}$$

$$H_3 = \frac{1}{2}\hat{I}_3 = \frac{1}{2}\left(2\hat{\Sigma}_{23}\hat{\Sigma}_{13}\hat{\Sigma}_{12} + \hat{\Sigma}_{11}\hat{\Sigma}_{22}\hat{\Sigma}_{33} - \hat{\Sigma}_{11}\hat{\Sigma}_{23}{}^2 - \hat{\Sigma}_{22}\hat{\Sigma}_{13}{}^2 - \hat{\Sigma}_{33}\hat{\Sigma}_{12}{}^2\right). \tag{A.6}$$

Following the change of variables proposed by Barlat et al. (2005):

$$\hat{\Sigma} = \overline{\Sigma} + H_1. \tag{A.7}$$

The characteristic equation becomes:

$$\overline{\Sigma}^3 - 3H_\mathrm{p}\overline{\Sigma} - 2H_\mathrm{q} = 0, \tag{A.8}$$

where

$$H_\mathrm{p} = \left(H_1^2 + H_2\right) \geq 0, \tag{A.9}$$

$$H_\mathrm{q} = \frac{1}{2}\left(2H_1^3 + 3H_1H_2 + 2H_3\right). \tag{A.10}$$

Cardan's solution to the modified characteristic Equation (A.8) is:

$$\overline{\Sigma}_1 = z^{1/3} + \overline{z}^{1/3}, \tag{A.11}$$

$$\overline{\Sigma}_2 = \omega z^{1/3} + \overline{\omega}\overline{z}^{1/3}, \tag{A.12}$$

$$\overline{\Sigma}_3 = \overline{\omega} z^{1/3} + \omega \overline{z}^{1/3}, \tag{A.13}$$

where z in a complex number (a+ib), ω is a complex constant ($e^{-2i\pi/3}$), and $\overline{z}$ and $\overline{\omega}$ are their conjugate quantities, with:

$$z = H_{\mathrm{q}} + \mathrm{i}\sqrt{H_{\mathrm{p}}{}^3 - H_{\mathrm{q}}{}^2}. \tag{A.14}$$

Hence, the principal values of $\hat{\boldsymbol{\Sigma}}$ are:

$$\hat{\Sigma}_1 = H_1 + 2\sqrt{H_1{}^2 + H_2}\cos(\theta/3), \tag{A.15}$$

$$\hat{\Sigma}_2 = H_1 + 2\sqrt{H_1{}^2 + H_2}\cos\left(\frac{\theta + 4\pi}{3}\right), \tag{A.16}$$

$$\hat{\Sigma}_3 = H_1 + 2\sqrt{H_1{}^2 + H_2}\cos\left(\frac{\theta + 2\pi}{3}\right), \tag{A.17}$$

with

$$\theta = \arccos\left(\frac{H_{\mathrm{q}}}{H_{\mathrm{p}}{}^{3/2}}\right). \tag{A.18}$$

According to Barlat et al. (2005) these values are ordered as:

$$\hat{\Sigma}_1 \geq \hat{\Sigma}_2 \geq \hat{\Sigma}_3, \quad \hat{\Sigma}_1 > \hat{\Sigma}_3. \tag{A.19}$$

Annex B - Components of the Fourth-Order Anisotropic Tensor B

Tensor **B** denotes the inverse of the linear transformed anisotropy fourth-order tensor $\mathbf{L}=(\mathbf{C}:\mathbf{T})$ where **T** is the fourth-order deviatoric unit tensor given by

$$\mathbf{T}=\begin{bmatrix} 2/3 & -1/3 & -1/3 & 0 & 0 & 0 \\ -1/3 & 2/3 & -1/3 & 0 & 0 & 0 \\ -1/3 & -1/3 & 2/3 & 0 & 0 & 0 \\ 0 & 0 & 0 & 1 & 0 & 0 \\ 0 & 0 & 0 & 0 & 1 & 0 \\ 0 & 0 & 0 & 0 & 0 & 1 \end{bmatrix}, \tag{B.1}$$

and **C** is the original CPB06's fourth-order symmetric tensor describing the anisotropy of the matrix (see Equation (3.4)). In order to determine the hydrostatic anisotropy factor, *h* the components of the tensor **B**, must be known (as shown in Equations (3.15)-(3.16)). According to Revil-Baudard et al. (2016), the components of B_{ij}, with $i,j=1,...,6$, are given in Voigt notation in terms of L_{ij}, with $i,j=1,...,6$, by:

$$B_{12}=\frac{1}{3}\frac{2(L_{32}-L_{12})+(L_{31}-L_{11})}{(L_{21}-L_{11})(L_{32}-L_{12})-(L_{22}-L_{12})(L_{31}-L_{11})}, \tag{B.2}$$

$$B_{13}=\frac{1}{3}\frac{(L_{11}-L_{21})+2(L_{12}-L_{22})}{(L_{21}-L_{11})(L_{32}-L_{12})-(L_{22}-L_{12})(L_{31}-L_{11})}, \tag{B.3}$$

$$B_{11}=-(B_{12}+B_{13}), \tag{B.4}$$

$$B_{21}=B_{12}, \tag{B.5}$$

$$B_{23}=\frac{1}{3}\frac{2(L_{11}-L_{21})+(L_{12}-L_{22})}{(L_{11}-L_{21})(L_{32}-L_{22})-(L_{12}-L_{22})(L_{31}-L_{21})}, \tag{B.6}$$

$$B_{22}=-(B_{21}+B_{23}), \tag{B.7}$$

$$B_{31}=B_{13}, \tag{B.8}$$

$$B_{32}=B_{23}, \tag{B.9}$$

$$B_{33}=-(B_{31}+B_{23}), \tag{B.10}$$

$$B_{44}=\frac{1}{L_{44}};\ \ B_{55}=\frac{1}{L_{55}};\ \ B_{66}=\frac{1}{L_{66}}. \tag{B.11}$$

Appendix A - Axisymmetric Stress State Particularities and Relationships

Assuming an axisymmetric loading, the macroscopic stress tensor, $\boldsymbol{\Sigma}$ is given by:

$$\boldsymbol{\Sigma} = \begin{bmatrix} \Sigma_{11} & 0 & 0 \\ 0 & \Sigma_{11} & 0 \\ 0 & 0 & \Sigma_{33} \end{bmatrix} = \Sigma_{11} \begin{bmatrix} 1 & 0 & 0 \\ 0 & 1 & 0 \\ 0 & 0 & \rho \end{bmatrix}, \tag{A.1}$$

where the constant ρ is the ratio between the lateral and the axial macroscopic imposed stresses, i.e.:

$$\rho = \frac{\Sigma_{33}}{\Sigma_{11}}, \tag{A.2}$$

prescribed in order to originate a specified stress triaxiality value. Hence, the macroscopic mean stress, Σ_m becomes:

$$\Sigma_m = \frac{2\Sigma_{11} + \Sigma_{33}}{3} = \Sigma_{11}\left(\frac{2+\rho}{3}\right), \tag{A.3}$$

which results in a macroscopic deviatoric stress tensor, $\boldsymbol{\Sigma}'$ given by:

$$\boldsymbol{\Sigma}' = \boldsymbol{\Sigma} - \Sigma_m \mathbf{I} = \Sigma_{11} \begin{bmatrix} \frac{1-\rho}{3} & 0 & 0 \\ 0 & \frac{1-\rho}{3} & 0 \\ 0 & 0 & \frac{2(\rho-1)}{3} \end{bmatrix}. \tag{A.4}$$

Therefore, the second and third deviatoric stress invariants, respectively J_2^{Σ} and J_3^{Σ} can be written as:

$$J_2^{\Sigma} = \frac{1}{2}\left(\Sigma_1'^2 + \Sigma_2'^2 + \Sigma_3'^2\right) = \frac{1}{3}\Sigma_{11}^2\left(\rho-1\right)^2, \tag{A.5}$$

$$J_3^{\Sigma} = \Sigma_1'\Sigma_2'\Sigma_3' = \frac{2}{27}\Sigma_{11}^3\left(\rho-1\right)^3. \tag{A.6}$$

The von Mises equivalent stress, Σ_e is determined by the second deviatoric stress invariant, J_2^{Σ} as:

$$\Sigma_e = \sqrt{3J_2^{\Sigma}} = \left|\Sigma_{11}\left(\rho-1\right)\right|. \tag{A.7}$$

Thus, the stress triaxiality, T_{Σ} results:

$$T_{\Sigma}=\frac{\Sigma_{\mathrm{m}}}{\Sigma_{\mathrm{e}}}=\frac{\Sigma_{11}\left(2+\rho\right)}{3\left|\Sigma_{11}\left(\rho-1\right)\right|}=\begin{cases}\dfrac{2+\rho}{3\left(\rho-1\right)} & \text{if } \rho>1,\\ \dfrac{2+\rho}{3\left(1-\rho\right)} & \text{if } \rho<1,\end{cases} \quad \text{for } \Sigma_{11}>0. \tag{A.8}$$

Rearranging the previous expression results:

$$\rho=\begin{cases}\dfrac{3T_{\Sigma}+2}{3T_{\Sigma}-1} & \text{if } J_3^{\Sigma}>0;\\ \dfrac{3T_{\Sigma}-2}{3T_{\Sigma}+1} & \text{if } J_3^{\Sigma}<0,\end{cases} \tag{A.9}$$

which represent both ρ values that yield a certain stress triaxiality.

The normalized third-invariant of the deviatoric stress tensor, ξ_{Σ} (see Equation (2.7)) resumes to:

$$\xi_{\Sigma}=\frac{3\sqrt{3}}{2}\frac{J_3^{\Sigma}}{\left(J_2^{\Sigma}\right)^{3/2}}=\frac{\left(\rho-1\right)^3}{\left|\rho-1\right|^3}=\operatorname{sgn}\left(\rho-1\right)=\begin{cases}+1 & \text{if } \rho>1;\\ -1 & \text{if } \rho<1,\end{cases} \tag{A.10}$$

which corresponds to a Lode angle parameter, $\bar{\theta}_{\Sigma}$ given by:

$$\bar{\theta}_{\Sigma}=1-\frac{2}{\pi}\arccos\left(\xi_{\Sigma}\right)=\begin{cases}+1 & \text{if } \rho>1;\\ -1 & \text{if } \rho<1.\end{cases} \tag{A.11}$$

Thus, it is concluded that, regardless of the value $\rho=\Sigma_{33}/\Sigma_{11}$ (i.e. the stress triaxiality), under axisymmetric loadings, the Lode angle parameter takes only two possible values: $\bar{\theta}_{\Sigma}=\pm 1$.